DISSERTATION

submitted to the Combined Faculties for

the Natural Sciences and for Mathematics of the

Ruperto-Carola University Heidelberg, Germany

for the degree of

Doctor of Natural Sciences

presented by

Master of Science Katharina Anna Quadt

born in Berlin, Germany

Oral examination: 19.03.2018

Force and retrograde flow in *Plasmodium berghei* sporozoites

Referees:

Prof. Dr. Ulrich Schwarz

Prof. Dr. Friedrich Frischknecht

Table of contents

Table of contents

Table of contents

Summary

Plasmodium sporozoites, the motile forms that are transmitted from the mosquito to the mammalian host, use a unique type of locomotion called gliding motility. This motility is powered by an actin-myosin motor underneath the plasma membrane: Myosin pulls on actin-filaments that are connected to adhesins of the thrombospondin-related anonymous protein (TRAP) family including TLP (TRAP-like protein). These membrane-spanning proteins interact with host cell receptors thereby transmitting the generated force to the substrate resulting in a forward movement of the cell. As a consequence, the filamentous actin-adhesin complexes are driven back to the rear of the cell, which is known as retrograde flow. The role of TLP and actin filaments in force production and retrograde flow of *Plasmodium berghei* sporozoites was investigated using reverse genetics, live cell imaging and optical tweezers. This instrument allows manipulation of microscopic objects by exerting forces in the piconewton range via a highly focused laser beam. In our experiments, we positioned polystyrene particles onto the gliding sporozoites, which actively translocated these beads towards the posterior end of the cell. We found that transport speeds were significantly higher than the sporozoite forward movement (1-2 μm/s) independent of particle size or functionalization. This bead transport most likely indirectly reflects retrograde flow in sporozoites. Wild type sporozoites and transgenic sporozoites lacking the surface protein TLP with and without different concentrations of actin-modulating drugs (cytochalasin D and jasplakinolide) were challenged to pull beads from the optical traps at different forces. These experiments revealed a role of TLP in controlling the retrograde flow by converting it into optimal force transmission for gliding motility. Further, force experiments on mutant sporozoites with altered TLP C-termini refined our hypothesis and suggested a function for the extracellular domain in recruiting surrounding surface proteins and possibly stabilizing them laterally for force transmission.

In a second project, I assessed parasite-induced surface protrusions called knobs on *P. falciparum*-infected erythrocytes using Atomic Force Microscopy (AFM). This analysis revealed that the knobs on infected erythrocytes carrying heterozygous sickle cell- traits were larger but fewer.

Zusammenfassung

Plasmodium Sporozoiten, die bewegliche Form des Parasiten, welche vom Moskito auf den Säugetierwirt übertragen wird, bewegen sich auf einzigartige Weise fort, durch die sogenannte Gleitbewegung. Erzeugt wird diese Bewegung durch einen Aktin-Myosin-Motor, der sich unter der Plasmamembran befindet: Myosin zieht an Aktinfilamenten, die mit Oberflächenproteinen aus der Familie der TRAP-Proteine, inklusive TLP (TRAP-like protein), verbunden sind. Diese membrandurchspannenden Proteine interagieren mit Rezeptoren der Wirtszelle und übertragen so die erzeugte Kraft auf das Substrat, was zu einer Vorwärtsbewegung der Zelle führt. Dadurch werden die Komplexe aus Aktinfilamenten und Adhäsinen zum Ende der Zelle nach hinten bewegt, was als retrograder Fluss bekannt ist. Die Rolle die TLP und Aktinfilamente während der Kraftentwicklung und des retrograden Flusses in *Plasmodium berghei* Sporozoiten spielen, wurde mit Hilfe reverser Genetik, Lebendmikroskopie und optischer Pinzetten untersucht. Dieses Instrument ermöglicht die Manipulation mikroskopisch kleiner Objekte durch die Ausübung von Kräften im Piconewtonbereich mittels eines hoch fokussierten Laserstrahls. In unseren Experimenten positionierten wir Mikropartikel aus Polystyrol auf sich fortbewegende Sporozoiten, die diese Partikel aktiv zum hinteren Ende der Zelle transportierten. Wir fanden heraus, dass die Transportgeschwindigkeiten, unabhängig von Größe und Funktionalisierung des Partikels, signifikant höher waren als die Vorwärtsbewegung des Sporozoiten (1-2 µm/s). Der Partikeltransport spiegelt höchstwahrscheinlich indirekt den retrograden Fluss in Sporozoiten wieder. Wildtyp- und genetisch veränderte Sporozoiten, denen das Oberflächenprotein TLP fehlt, wurden bei verschieden Laserstärken in An- und Abwesenheit unterschiedlicher Konzentrationen von Aktinfilamente beeinflussenden Substanzen (Cytochalasin D und Jasplakinolide) auf ihr Vermögen getestet, Partikel aus der optischen Falle herauszuziehen. Die Experimente zeigten, dass TLP bei der Steuerung des retrograden Flusses eine Rolle übernimmt, indem es diesen in eine für die Vorwärtsbewegung optimale Kraftübertragung umwandelt. Darüber hinaus verfeinerten Kraftexperimente an mutierten Sporozoiten mit veränderten TLP C-Termini unsere Hypothese, und legten eine Funktion der extrazellulären Domäne nahe, umliegende Oberflächenproteine zu rekrutieren und diese möglicherweise für die Kraftübertragung lateral zu stabilisieren.

Zusammenfassung

In einem zweiten Projekt vermaß ich auf der Oberfläche von mit *P. falciparum*-infizierten Erythrozyten befindliche, vom Parasiten induzierte Vorwölbungen, sogenannte Knobs, mit Hilfe der Rasterkraftmikroskopie. Diese Analyse ergab, dass die Knobs auf Erythrozyten mit Hämoglobin von heterozygoten Trägern der Sichelzellanämie größer sind, dafür aber in geringerer Dichte auftreten.

Acknowledgments

First, I would like to thank Freddy for supporting me during the Tweezer project, giving me the freedom to go to Australia (and letting me come back) and be puzzled about data together. I learned to trust my skills and to discuss my experiments with confidence. Also, thank you for proof-reading my thesis.

Thanks to Prof. Ulrich Schwarz for being in my TAC-meeting and in my defense committee and for advice on the physics behind my experiments. Also, thank you to Dr. Silvia Portugal and Dr. Annika Guse for attending my defense. Thanks to Prof. Joachim Spatz for making it possible for me to use the optical tweezers and the AFM.

I also want to thank my parents and my grandparents for unconditional support and for believing in me throughout my academic endeavors.

I would like to thank Catherine for working together at the tweezers and showing me the "art" of cloning. You are very patient teacher, great at breaking down complex problems and you make everything more fun. I admire your wits and I appreciate your honesty. I feel very fortunate to share my life with you.

Thanks to the whole lab for a pleasant working atmosphere. Martin for developing the experiments at the tweezers, for your expertise on physics and for proof-reading my thesis. Miriam and Christian for taking excellent care of the mosquito breeding. Mirko and Dennis for never being annoyed by my questions. Jessica and Julia for knowing what to do and if not finding out. Ross for always being helpful and kind. Johanna for being the most independent and successful student. Markus for sharing his knowledge. Tina for countless coffees and laughs. Ben for making the practical more fun. Verena for enjoying coffee breaks and unwinding at the gym. Thanks to the Deponte lab for sharing lab equipment and entertaining social gatherings. Mendi, Noa and Konrad for your friendship and enjoying life outside the lab. Birthe for always being there and moral support. Carla and Yvonne for putting everything in perspective and for creating much-needed diversions. Johannes for helping me with emergency IT-problems and making me take myself not too seriously.

Abbreviations

AFM	Atomic force microscopy
ADF1/2	Actin-depolymerizing factor 1 and 2
AOD	Acousto-optic deflector
BSA	Bovine serum albumin
CAP	Cyclase-associated protein
CP	Capping protein
CD36	Cluster of differentiation 36
CelTOS	Cell traversal of ookinetes and sporozoites
CSA	Chondroitin sulphate A
CSP	Circumsporozoite protein
CTD	Cytoplasmic tail domain
CytoD	Cytochalasin D
DIC	Differential interference contrast
DNA	Deoxyribonucleic acid
DV	Digestive vacuole
ECM	Extracellular matrix
ELC	Essential light chains
EPCR	Endothelial protein C receptor
EphA2	Ephrin receptor
FACS	Fluorescence-activated cell sorting
F-actin	Filamentous actin
FA	Focal adhesion
fps	Frames per second
FRAP	Fluorescence recovery after photobleaching
G-actin	Globular actin
GAP 40/45/50	Glideosome-associated proteins
GEST	Gamete egress and sporozoite traversal
HOT	Holographic optical tweezers
HSPG	Heparan sulfate proteoglycan

Abbreviations

ICAM-1	Intercellular adhesion molecule-1
IMC	Inner membrane complex
iRBCs	Infected red blood cells
IP	intraperitoneal(ly)
IV	intravenous(ly)
Jas	Jasplakinolide
KAHRP	Knob-associated histidine-rich protein
MTIP	Myosin A tail domain interacting protein
NA	Numerical aperture
OT	Optical tweezers
PCR	Polymerase chain reaction
*Pf*EMP1	*Plasmodium falciparum* erythrocyte membrane protein 1
PM	Plasma membrane
PPLP1	Perforin-like protein 1
PVM	Parasitophorous vacuole membrane
PV	Parasitophorous vacuole
QPD	Quadrant photodiode
RG	Red green line
RS-actin	Rabbit skeletal actin
RNA	Ribonucleic acid
S6	Sporozoite gene 6
SEM	Scanning electron microscope
SPECT-1/2	Sporozoite microneme protein essential for cell traversal
TEM	Transmission electron microscope
TRAP	Thrombospondin-related anonymous protein
TREP	TRAP-related protein
TLP	TRAP-like protein
UOS3	Upregulated in oocyst derived sporozoites 3
*var*2CSA	Variant surface antigen 2 chondroitin sulphate A
VCAM 1	Vascular cell adhesion molecule 1
Wt	Wild type

1 Introduction

1.1 Components of cell migration

Cell motility is a highly dynamic process and important during embryonic development, immune responses and wound healing, and can lead to inflammation and cancer metastasis in pathological processes (Friedl, 2004). The cytoskeleton is the essential component in coordinating cell motility. It is composed of three distinct types of polymers: actin, microtubules and intermediate filaments. Actin is the most abundant protein of the cytoskeleton and exists either in a monomeric, globular form or as polymeric, filamentous actin (F-actin) (Lodish, 2000). The actin filament can be considered to consist of two parallel protofilaments that twist around each other in a right-handed helix (Melak et al., 2017). For actin elongation ATP-bound - G - actin monomers are incorporated into a filament and the bound ATP is hydrolyzed to ADP. As a result of this hydrolysis, most of the filament consists of ADP -F-actin, but ATP - F-actin is found at the growing end. The (+) end - also referred to as the barbed end - elongates faster than the (−) end or pointed end, which reflects the polarity of the actin filament.

The length of the filament can remain constant, with the newly added subunits travelling through the filament, until they reach the (−) end, where they dissociate. This process is known as "treadmilling" (Figure 1), which can occur in the lamellipodia of cells. Subunits released from one end of the filament are rapidly recruited to assemble at the leading edge of the cell (Pollard et al., 2000).

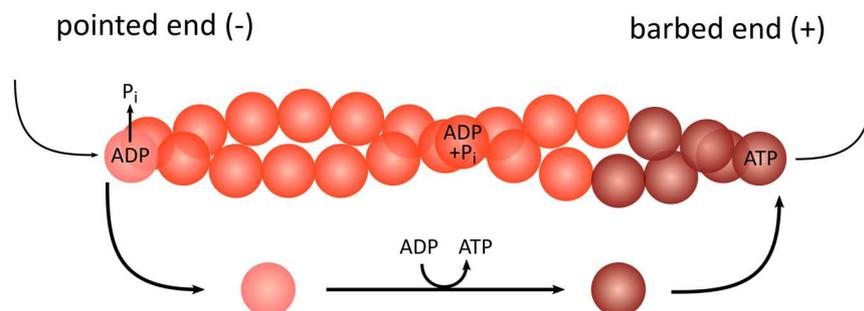Figure 1: Actin filament undergoing treadmilling. The filament length remains constant, while actin monomers are added to the barbed end (+) (ATP-actin) and dissociate from the pointed end (-) (ADP-actin). After exchange of ADP for ATP, ATP-actin is added to the barbed-end (+). The filament growth at the barbed end is higher indicated by the bold arrow and dissociation is lower and *vice versa* at the pointed end (-).

In vitro, actin polymerization depends on salt and monomer concentration. However, growth and disassembly of actin filaments in cells are tightly controlled by several actin-binding proteins that either promote or inhibit actin polymerization (Blanchoin et al., 2014). Actin filaments in the cell cortex determine the shape, stiffness and movement of the cell surface in response to external stimuli. The physical linkage between cytoskeletal actin and the extracellular matrix (ECM) is mediated by integrins, which provides traction for migration. Integrins consist of two non-covalently associated glycoprotein subunits α and ß. In type I integral membrane proteins, the short intracellular tail binds to a complex of proteins linking to the cytoskeleton and the N-terminal extracellular domain interacts with ligands of the extracellular matrix like laminin, collagen or fibronectin. Integrins can switch between an active and an inactive conformation enabling the motile cell to quickly form and break attachments (Hynes, 2002). Integrin activation can be initiated by the binding of cytoplasmic proteins ("inside-out activation") or by the binding of integrins to extracellular ligands ("outside-in signaling ") (Takagi et al., 2002). Activation induces conformational changes and leads to assembly of actin filaments at the intracellular end of the integrin and force can be applied to the point of attachment. Focal adhesions (FAs) are comprised of clusters of integrin receptors associated with large complexes of signaling and structural proteins linked to the actin cytoskeleton to form strong adhesions (Alberts et al., 2002). Interestingly, amoeboid migration of, for instance leukocytes in 3D environments can be adhesion-independent and does not require high traction forces, but is characterized by constant shape changes and is 100 times faster than mesenchymal migration of highly adhesive cells, such as fibroblasts (Renkawitz and Sixt, 2010).

1.1.2 Molecular Mechanics: Force and actin flow

Directed migration follows a cycle of well-defined steps starting with lamellipodial and or filopodial protrusion driven by actin polymerization at the leading edge (Figure 2 A), where new adhesion sites are formed (Figure 2 B). This is followed by the disruption of older adhesion sites at the cell rear and cytoskeleton contraction which results in forward movement of the cell (Figure 2 C). The actin polymerization pushing against the plasma membrane and myosin II contraction at the cell center also generate a rearward directed retrograde flow (Figure 2 D) (Fournier et al., 2010; Gardel et al., 2008; Ponti et al., 2004).

The retrograde flow was first observed by particles being transported rearward over the cell surface of fibroblasts and initially proposed to be caused by moving plasma membrane (Abercrombie et al., 1970; Harris and Dunn, 1972). However, it was later demonstrated by fluorescence recovery after photobleaching (FRAP) experiments of fluorescently labeled actin, that actin monomers were incorporated into filaments at the leading edge and underwent a rearward movement away from the cell edge (Wang, 1985). Forscher *et al*. showed that retrograde flow in neural growth cones depends on both actin polymerization and myosin II contractility (Forscher et al., 1992; Lin et al., 1996).

The regulation of retrograde flow-driven movement which depends on transmembrane force-coupling receptors connecting rearward flowing actin and the ECM has been described as a 'molecular clutch' (Mitchison and Kirschner, 1988). If the clutch is not engaged, slippage will occur between the cytoskeleton and adhesion receptors and actin polymerization without
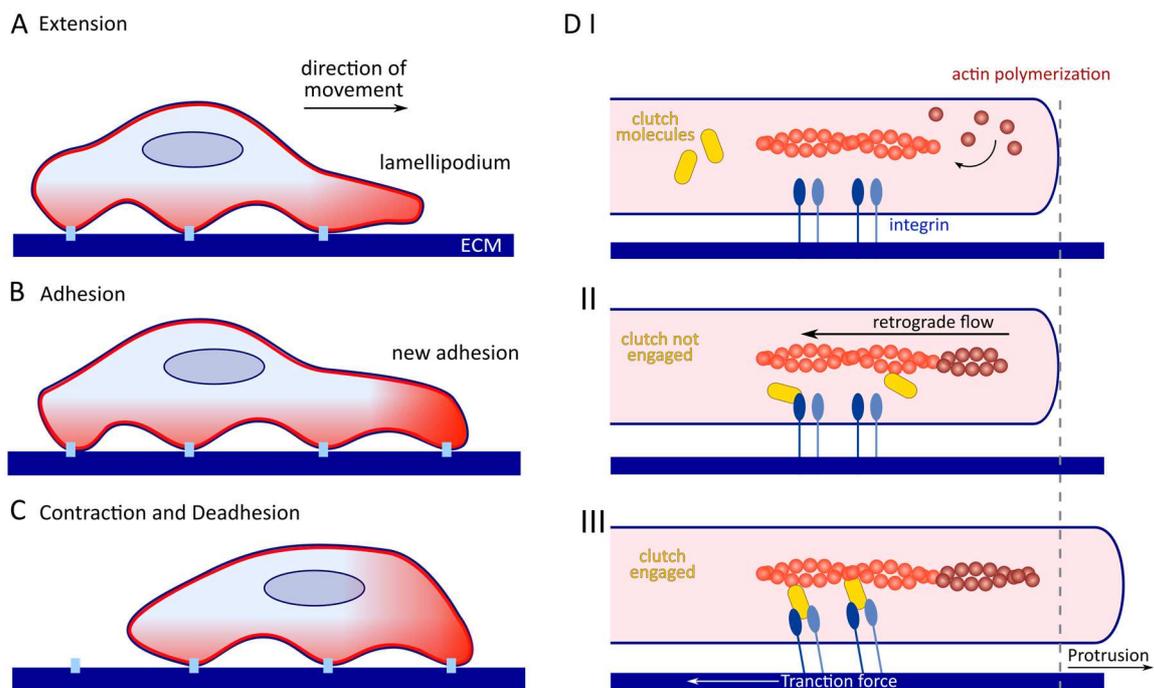
Figure 2: Actin-based cellular forces are transmitted through surface receptors that bind to the extracellular matrix to generate friction that induces traction against the extracellular environment. (A) The migrating cell forms protrusion at the leading edge by actin polymerization. (B) Adhesions of the extending network to the underlying substrate via integrins are formed (C) The cell retracts its trailing edge by combining actomyosin contractility and disassembly of adhesions at the rear. (D) Retrograde flow conversion according to the "molecular clutch" model. Transmembrane proteins (blue) convert the force generated by actin assembly (red) into protrusion. (I+II) The molecular clutch is disengaged; there is no connection between adhesions and the actin cytoskeleton. In this situation, no protrusion occurs because actin treadmilling is mainly converted into retrograde flow. (III): The molecular clutch is engaged. The connection between the polymerizing actin network and the substrate results in membrane protrusion. Moreover, this connection enables the conversion of the acto-myosin tension into traction of the cell body and retraction of the tail. Figure adapted from Case and Waterman, 2015.

connection to the ECM results in fast retrograde flow, while traction force is decreased (Figure 2 D I+II). When the clutch is engaged, forces generated by actin polymerization are transmitted through clustered ECM-bound integrins resulting in slow retrograde flow, rearward traction and membrane protrusion (Figure 2 D III). This means actin retrograde flow speeds decreases at sites of focal adhesions and traction forces are observed to be highest (Alexandrova et al., 2008; Gardel et al., 2008; Hu et al., 2007). Also, actin polymerization in the lamellipodium of fast moving fish keratocytes was demonstrated to be directly coupled to forward movement (Theriot and Mitchison, 1991), conversely retrograde flow was observed to be inversely related to cell speed (Jurado et al., 2005) also reported in neural growth cones (Lin and Forscher, 1995).

1.2 Optical tweezers

The weak non-covalent bonds that hold biomolecules (and entire cells) together exert forces that are typically in the piconewton range. In order to study and measure those forces, optical tweezers, which originally were invented 30 years ago by Arthur Ashkin and co-workers (Ashkin et al., 1986) have been proven to be a useful non-invasive tool for biological systems and for monitoring interactions between cells or proteins.

Applications of optical tweezers on single molecular level range from DNA stretching (Wang et al., 1997) and protein folding (Cecconi et al., 2005) to measurements of step sizes and forces exerted by motor proteins such as kinesin (Svoboda and Block, 1994) and myosin (Finer et al., 1994; Veigel et al., 1998). Manipulation on the single cell level include the quantification of the propulsion force from trypanosomes (Stellamanns et al., 2014), forces during cell-cell interactions (Crick et al., 2014) and characterization of mechanical cell properties (Dao et al., 2003). Recent advances allow optical trapping *in vivo* (Harlepp et al., 2017) and the combination of optical tweezers with fluorescence microscopy offers simultaneous and correlative visualization and manipulation of molecular interactions (Hashemi Shabestari et al., 2017) while the use of optical tweezers also complement Atomic Force Microscopy in force spectroscopy (Pierini et al., 2016).

1.2.1 Principle of Optical Tweezers

The optical tweezers exert forces induced by a strongly focused laser beam on dielectric particles. The optical trapping force can be explained by decomposing it into two components: a scattering force or radiation pressure pushing the bead in the direction of light propagation. The force exerted on the particle results from the interaction between the laser-induced dipole in the dielectric particle and the electric gradient field of the focused laser beam. The gradient force acts on the dipole attracting the particle along the light intensity gradient to the focus, where the electric field intensity is highest. As the focused laser beam exhibits a Gaussian intensity profile, the gradient force is directed to the center of the trap (Figure 3). To obtain a stable three-dimensional trap, the gradient force in the axial direction must be greater than the scattering force. This requires a very steep intensity gradient, which is achieved by focusing the laser beam through an objective of high numerical aperture.
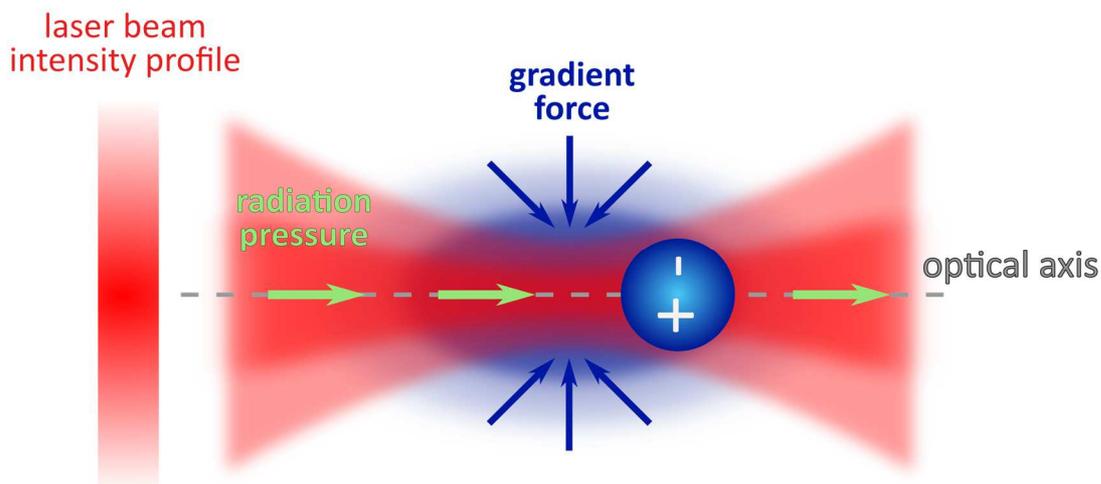
Figure 3: Working principle of Optical Tweezers: Focused laser beam with Gaussian intensity laser profile interacts with dielectric particle. A part of the incident photons is scattered by the particle resulting in the scattering force – radiation pressure – pushing the particle in the direction of propagation of the beam (green arrows). As a consequence, particles are always trapped slightly behind the focus. The gradient force (blue) pulls the particle along the light intensity gradient to the focal point with the highest intensity.

The force experienced by the bead (*F*) points toward the trap center and grows with the distance of the bead from the trap center ($x_{displacement}$). The trap behaves as a Hookean spring for small distances: $F = -k_{trap}\, x_{displacement}$, where k_{trap} is the stiffness (Figure 4 A). Beyond the linear region, a small zone of near-constant force follows at the border of the potential, after which the force rapidly drops to zero (Figure 4 B).
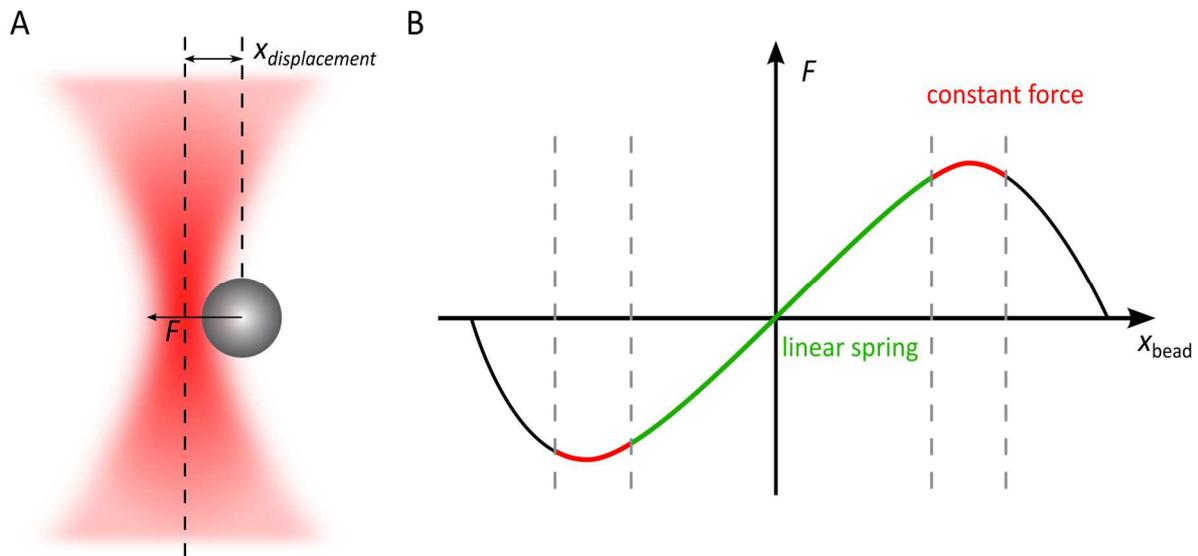
Figure 4: Optical tweezers apply spring-like forces to dielectric particle (A) Dielectric particle trapped near the focus of the laser beam. The Force (*F*) pulls in the opposing direction of the lateral displacement of the bead ($x_{displacement}$). (B) For small displacements, the force exerted by optical tweezers grows linearly with the distance. The linear region (green) is followed by near-constant force region (red) and goes down to zero beyond that.

To measure the trap stiffness for greater displacements, a calibration method based on particle displacement from the trap center in response to viscous drag is used. This approach requires information about the viscosity of the medium and the particle diameter and only applies for spherical objects (see Methods section 2.4.1).

The optical tweezers systems employed in this thesis allow for generation of multiple traps using different techniques. One realization is called holographic optical tweezers (HOT) using a liquid-crystal spatial light modulator (SLM) for trap generation. The SLM is an array of liquid crystal pixels. The orientation of the liquid crystal in each pixel can be adjusted individually in order to vary the effective optical path length. This way the incident plane phase front is reshaped according to the computer-generated hologram leading to the intensity profile encoded in the hologram displayed on the SLM (Grier, 2003). Previous studies including actin bundling experiments (Streichfuss et al., 2011) and direct manipulation of transgenic malaria parasites (Hegge et al., 2012) were performed with this set up. Alternatively, steerable devices like acousto-optic deflectors (AODs) and galvo-mirrors are able to create multiple traps by

time-sharing the laser beam between different trap positions at high frequencies. The latter technology is part of the second optical tweezers set up used in this work.

1.3 Life cycle of *Plasmodium*

In 2016 malaria caused an estimated 216 million cases and 445,000 deaths worldwide. Most of these deaths occurred in African (90%), mainly in young children (WHO (2017)). The causative agent of malaria is the protozoan parasite *Plasmodium*, transmitted by *Anopheles* mosquitoes. Five species of the genus *Plasmodium* are known, that cause infections in humans: *Plasmodium falciparum*, *Plasmodium vivax*, *Plasmodium ovale*, *Plasmodium malariae*, and in parts of southeast Asia, *Plasmodium knowlesi* (Kantele and Jokiranta, 2011). In order to investigate the parasites life cycle *in vivo*, rodent malaria parasites are often used as models of human malaria (Carter, 1977; Craig et al., 2012). Four different species that infect African rodents have been adapted for laboratory use: *Plasmodium berghei*, *P. yoelii*, *P. chabaudi* and *P. vinckei.* The preferred mouse model - also used in this thesis - for analysis of *Plasmodium* gene function is *P. berghei* providing efficient reverse genetics technologies (Janse et al., 2011; Janse et al., 2006; Otto et al., 2014).

1.3.1 Sporozoite stage and exo-erythrocytic forms

When a female infected mosquito takes a blood meal, *Plasmodium* sporozoites are injected into the skin of the mammalian host. Subsequently, the highly motile sporozoites migrate through the dermis to find a blood vessel and enter the bloodstream to be transported to the liver (Amino et al., 2006; Douglas et al., 2015). Sporozoites that remain at the bite site get eliminated by recruited immune cells (Amino et al., 2008). The same happens to parasites that end up in the lymphatic system, where they get degraded in the draining lymph nodes (Amino et al., 2006; Yamauchi et al., 2007). After arriving at the liver, sporozoites leave the bloodstream again by crossing the sinusoidal wall, the boundary between the liver sinusoid and hepatocytes. Sporozoites can either traverse sinusoidal Kupffer cells, the resident macrophages in the liver (Baer et al., 2007; Frevert et al., 2005; Pradel and Frevert, 2001), or migrate through endothelial cells (Tavares et al., 2013). In the liver, sporozoites traverse several hepatocytes before productively invading a terminal hepatocyte where they replicate (Mota et al., 2001). Cell traversal of the sporozoites requires several parasite factors like

phospholipase disrupting cell membranes (Bhanot et al., 2005), SPECT (sporozoite microneme protein essential for cell traversal) (Ishino et al., 2004) and the Perforin-Like Protein 1 (PLP1, also called SPECT2) both essential in wounding the host cell. CelTOS (cell traversal of ookinetes and sporozoites) has a role in cell traversal in both ookinetes and sporozoites (Kariu et al., 2006) and GEST (gamete egress and sporozoite traversal) mediates gamete egress and sporozoite traversal (Talman et al., 2011). The TRAP-like protein (TLP) that is the focus of this thesis, was also proposed to be involved in cell traversal of sporozoites (Moreira et al., 2008).

For subsequent invasion of the sporozoites, proteins including TRAP (thrombospondin related anonymous protein) (Matuschewski et al., 2002), AMA-1 (apical membrane antigen 1) (Silvie et al., 2004), or the 6-cysteine domain proteins P52 and P36 (Ishino et al., 2005; Labaied et al., 2007; van Dijk et al., 2005) have been implicated.

Also, receptors on hepatocytes haven been recently suggested to be important for invasion, like the Ephrin A2 (Kaushansky et al., 2015), the Scavenger Receptor B type 1 (SR-B1) and CD81, which is required for invasion of hepatocytes by *P. yoelii* and *P. falciparum* sporozoites (Vaughan and Kappe, 2017).

During invasion, the sporozoite forms a protective parasitophorous vacuole (PV), in which parasites develop into round, non-motile exo-erythrocytic forms (Prudencio et al., 2006). The parasitophorous vacuole membrane (PVM) is made up of hepatocyte plasma membrane and is modified by the parasite through the insertion of parasite proteins, essential for early liver stage development (Mueller et al., 2005a; Mueller et al., 2005b) and subsequent stage conversion (Silvie et al., 2014). Parasites also remove host-cell proteins from the PVM to avoid autophagy (Agop-Nersesian et al., 2017).

The replication of the parasite through schizogony within the vacuole of the hepatocyte leads to an amplification of parasite numbers, with 10,000 merozoites formed in one infected hepatocyte (Prudencio et al., 2006). Finally, merozoites are released as clusters within vesicles, called merosomes (Sturm et al., 2006). In the bloodstream, merozoites rapidly infect erythrocytes, initiating the asexual blood stage and the clinical symptoms of a malaria infection (Haldar et al., 2007; Miller et al., 2002).

1.3.2 Asexual blood stages and pathogenesis

The virulence of the asexual blood stages of *P. falciparum* is due to several modifications occurring in the infected erythrocyte and the export of parasite proteins to the plasma membrane of the host (Cooke et al., 2004; Deitsch and Wellems, 1996; Marti et al., 2005; Przyborski et al., 2003). These modifications alter the adhesive properties of the infected erythrocyte. After invasion, the merozoite develops inside a newly formed PV within the host red blood cell into a ring stage and progresses to the trophozoite stage and then to the replicating schizont stage. During parasite maturation, the hemoglobin from the red blood cell cytosol is internalized and digested in a compartment termed the digestive food vacuole (DV). The parasite uses only a fraction of the released amino acids for protein biosynthesis and the excess is discarded (Krugliak et al., 2002). The toxic heme released from the digested hemoglobin is detoxified by crystallizing it into hemozoin (Kapishnikov et al., 2017).

After 16 – 20 h post invasion, mature blood-stages of *P. falciparum* start sequestering in the microvascular of inner organs thereby avoiding passage through and, hence elimination by the spleen (Mebius and Kraal, 2005). At high parasite densities, the sequestered mass of infected erythrocytes leads to microvascular obstruction (Dondorp et al., 2008; Dondorp et al., 2004), metabolic disturbances, such as acidosis (Planche and Krishna, 2006), and release of damaging inflammatory mediators (Schofield, 2007; van der Heyde et al., 2006) which can combine to cause severe disease and death of the human host.

Cytoadhesion is mediated by members of the *Plasmodium falciparum* erythrocyte membrane protein 1 (*Pf*EMP1) family (Kraemer and Smith, 2006). *Pf*EMP1 proteins are encoded by approximately 60 *var* genes per parasite genome (Barry et al., 2007; Kyes et al., 2001). However, only one variant of *Pf*EMP1 is expressed per cell at any given time. The parasite is able to switch its *var* gene expression and therefore allows modifying the antigenic and functional properties of infected erythrocytes, evading immunity and altering adhesion capabilities (Ghumra et al., 2012; Guizetti and Scherf, 2013; Rowe et al., 2009).

*Pf*EMP1 variants can interact with numerous host cell receptors, including CD36, which leads to firm adhesion to microvascular endothelium (McCormick et al., 1997), intercellular adhesion molecule 1 (ICAM 1) mediating rolling of infected erythrocytes (Rowe et al., 2009; Smith et al., 2013), endothelial protein C receptor (EPCR) (Turner et al., 2013), P-selectin and vascular cell adhesion molecule 1 (VCAM 1) (Tembo and Montgomery, 2010). A specific

*Pf*EMP1 variant, *var*2CSA is responsible for pregnancy-associated malaria (PAM) by interacting with chondroitin sulphate A (CSA), which is abundant within the placental intervillous space (Clausen et al., 2012; Fried and Duffy, 1996; Salanti et al., 2004). Effective trafficking of parasite-derived proteins to the erythrocyte membrane is organized along actin filaments via parasite-generated unilamellar membrane profiles, termed Maurer's clefts (Cyrklaff et al., 2011). Within the erythrocyte plasma membrane, *Pf*EMP1 molecules are clustered on nanoscale knob-like protrusions (Cooke et al., 2000; Smith et al., 2013). The major structural component of the knobs on the inside of the erythrocyte is the knob-associated histidine-rich protein (KAHRP) (Pologe et al., 1987). KAHRP interacts with both parasite (Oberli et al., 2014) and skeletal host proteins; including spectrin, actin and ankyrin R (Helms et al., 2016; Oh et al., 2000; Weng et al., 2014). Expression of KAHRP has been shown to increase the rigidity of infected erythrocytes (Glenister et al., 2002). This rigidifying effect on the cytoskeleton is common to a number of exported parasite proteins (Maier et al., 2008). In the absence of knobs, infected erythrocytes show diminished presentation of *Pf*EMP1 and reduced cytoadherence to CD36, ICAM-1, and CSA under flow conditions (Crabb et al., 1997; Horrocks et al., 2005). Recent simulations demonstrated that the knob number and distribution influence the cytoadhesion dynamics (Dasanna et al., 2017).

Establishment of *in vivo* murine models is difficult, because rodent malaria parasite do not possess *Pf*EMP1 orthologs (Hall et al., 2005) or display knob structures on infected erythrocytes (Mackenstedt et al., 1989).

1.3.3 Sexual stages and parasite development within the mosquito

Transmission of the parasites from the host to the mosquito is an essential step in the *Plasmodium* life cycle. A population of the blood-stage parasites differentiates into the sexual forms of the parasite, which are known as gametocytes (Guttery et al., 2015). The parasites are already primed for gametocytogenesis at the merozoite stage (Meibalan and Marti, 2016). This sexual commitment is regulated by a highly conserved apicomplexan-specific transcription factor, ApiAP2-G, both in *P. falciparum* (Kafsack et al. 2014) and in *P. berghei* (Sinha et al. 2014). After ingestion by the mosquito, gametocytes mature into gametes triggered by a drop in temperature, a change in pH as well as the presence of xanthurenic acid in the mosquito gut (Billker et al., 1998). Male gametocytes transform into eight motile

microgametes and the female emerges from the erythrocyte as one macrogamete. For egress of the gametes, the parasites' PVM and the host red blood cell membrane need to be dissolved, which involves the secretion of specialized vesicles called osmiophilic bodies (Kehrer et al., 2016a; Kehrer et al., 2016b; Suarez-Cortes et al., 2016). During exflagellation, the haploid male gametes then fuse with female gametes to form a diploid zygote, which develops into an ookinete (Sinden, 1983). Ookinetes traverse the midgut epithelial cell wall and form oocysts underneath the basal lamina (Vlachou et al., 2006). Within the oocysts, mitotic divisions occur and sporozoites are formed in a process called sporogony. For egress from mature oocysts, proteolysis of the oocysts wall (Aly and Matuschewski, 2005; Mastan et al., 2017) and active movement of the sporozoites (Klug and Frischknecht, 2017) is required. Released sporozoites travel passively via the hemolymph through the mosquito body cavity
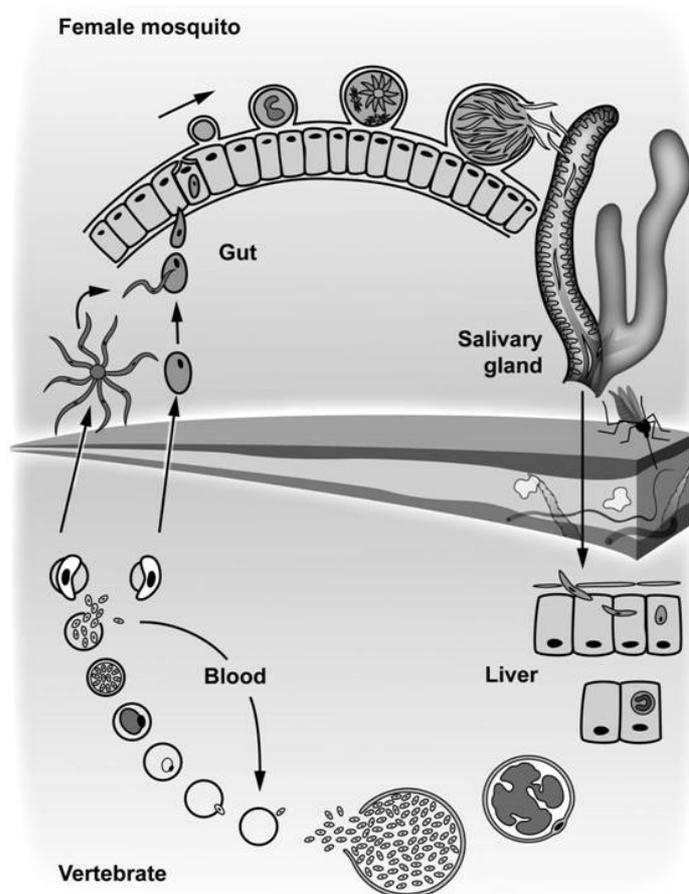
Figure 5: Life cycle of *Plasmodium*. Malaria-infected female mosquitoes inject sporozoites into the skin where they move actively to find and enter a blood vessel. Sporozoites get transported to the liver, where they breach through the endothelial wall at the liver sinusoid. After traversing several cells, sporozoites invade hepatocytes and replicate into thousands of merozoites. After leaving the liver, merozoites invade uninfected erythrocytes either starting the intra-erythrocytic cycle or developing into male or female gametocytes that can be transmitted back to the mosquito. Activated by the mosquito gut environment, male gametes fuse with females to produce a zygote, which develops into a motile ookinete that can traverse the mosquito midgut and forms an oocyst. After sporozoite formation, they egress from the oocyst and are passively transported within the hemolymph before invading the salivary glands.

to the salivary glands (Frischknecht et al., 2006), which they actively invade (Douglas et al., 2015). After penetration of the basal lamina, sporozoite passage through acinar cell into the secretory cavity (Pimenta et al., 1994), where they persist mostly non-motile (Frischknecht et al., 2004), while a small number of sporozoites enter eventually the salivary ducts for transmission to the next host.

1.3.4 Hemoglobinopathies

During the co-evolution of humans and *P. falciparum* parasites, the human genome has developed polymorphisms that confer innate resistance to infections with *Plasmodium*. However, they also cause significant disadvantages for the human – conditions called hemoglobinopathies. Normal hemoglobin (HbAA) is formed as a tetramer consisting of two α- and two β-globin chains and each globin chain is bound to one heme molecule. In hemoglobin S and C, the β-globin chain is altered at position 6 by a substitution of glutamic acid to valine and lysine respectively. Heterozygous HbAS and HbAC carriers have a significant survival advantage in *P. falciparum* infections. However, sickle cell disease (HbSS) is usually fatal, whereas the HbCC homozygotes have a mild, chronic hemolytic anemia and splenomegaly (Taylor et al., 2012).

How this partial protection is conferred is still under investigation (Taylor et al., 2013). It was reported, that these hemoglobin variants cause reduced cytoadherence probably resulting from diminished surface expression of *Pf*EMP1, which are aberrantly displayed on fewer and abnormally large knobs (Cholera et al., 2008; Fairhurst et al., 2005; Fairhurst et al., 2012; Fairhurst et al., 2003). A recent study supports a possible mechanism, that the intracellular trafficking and sorting of parasite-encoded adhesins to the host cell surface is impaired in HbSC and HbCC infected red blood cells (iRBCs) (Cyrklaff et al., 2011) due to disturbed redox regulation in these hemoglobinopathic erythrocytes (Cyrklaff et al., 2016).

1.4 *Plasmodium* sporozoites

1.4.1 Structure and motility

Plasmodium sporozoites are crescent shaped cells, that share common organelles like a nucleus, a mitochondrion, a secretory pathway with ER and Golgi (Schrevel et al., 2008) and an endosome-like vesicle with higher eukaryotes, while the apicoplast originating from the engulfment of an organism of the red algal lineage and functions in as fatty acid and isoprenoid and heme synthesis (McFadden, 2011) is a unique feature of Apicomplexans (Figure 6). Apicomplexan parasites are named after their apical complex containing polar rings, rhoptries, dense granules and micronemes. Rhoptries release their content during PV formation upon contact with a host cell. Molecules from dense granules are involved in modifying the host cell

after invasion. Micronemes are vesicles containing surface proteins important for gliding motility and invasion (Tomley and Soldati, 2001). Micronemal proteins can have transmembrane domains or like the circumsporozoite protein (CSP) possess glycolipid anchors, while some have ectodomains that resemble those of integrins from vertebrates which are essential for adhesion (Blackman and Bannister, 2001).

The apical part of the sporozoite has a polar ring structure, which is tilted toward the substrate. Microtubules originate at the polar ring and stretch along the cell ending close to the nucleus (Kudryashev et al., 2010b). In the cross section, the microtubules are evenly spaced over two-thirds of the ventral side of the cell, while a single one is typically located at the dorsal side (Cyrklaff et al., 2007; Kudryashev et al., 2012). The actin-myosin motor that drives motility is located in the space between the plasma membrane and an underlying flattened double membrane system termed the inner membrane complex (IMC). The IMC is in turn supported on the cytoplasmic face by an organized network of intermediate filament-like proteins termed the subpellicular network (Kudryashev et al., 2010b) and by interactions with the microtubules giving the parasite stability for maintaining its shape (Khater et al., 2004; Kudryashev et al., 2012).
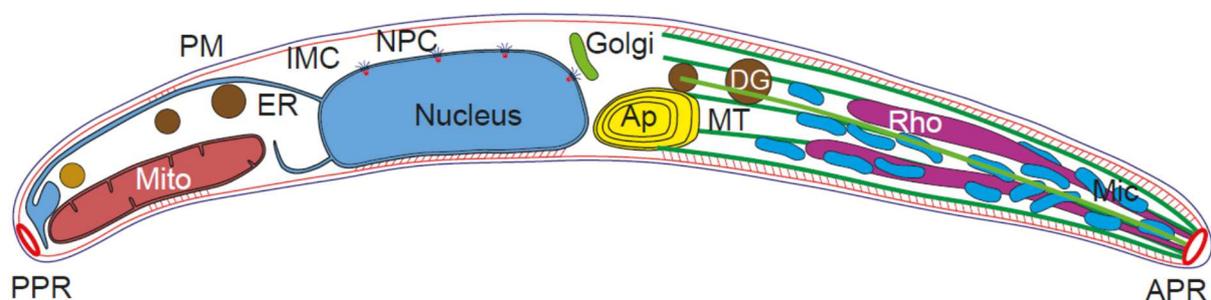
Figure 6: Sporozoite architecture of a *Plasmodium* sporozoite: nucleus (blue), mitochondrion (red), Ap: apicoplast (yellow), secretory organelles: Golgi (green), ER: endoplasmic reticulum (brown), apical complex with APR, apical polar ring (at the front end), Rho: rhoptries (purple), Mic: micronemes (blue), DG: dense granules (brown), MT: microtubules (green), layer surrounding the sporozoite PM: plasma membrane (blue), IMC: inner membrane complex (red), subpellicular network (orange) and PPR, proximal polar ring (at the posterior end) modified from (Kudryashev et al., 2010b).

Sporozoites move in an unusual form of substrate-dependent motility termed gliding without cilia, flagella, or amoeboid deformations of cell shape (Vanderberg, 1974). On flat glass support, the parasites glide in circular fashion, while they move in complex helical or corkscrew-like trajectories within the skin or in artificial 3D environments (Amino et al., 2006; Hellmann et al., 2011). Generally, they are able to adhere onto the substrate at either the

dorsal or the ventral sides, however they prefer to circle in one direction that appears as a counterclockwise (CCW) movement in an inverted microscopic set-up (Vanderberg, 1974). Micropillar arrays simulating extracellular environments have been shown to affect the sporozoites' motility pattern and directionality by varying size and distance between the pillars (Hellmann et al., 2011) and suggest that cell curvature has evolved to enable the movement of the sporozoites through the extracellular environment (Battista et al., 2014) and to find blood vessels with similar curvature and diameter (Hopp et al., 2015; Muthinja et al., 2017).

1.4.2 Molecular motor and motility

Sporozoites can achieve very high speeds of 1 – 3 µm/s upon transmission into the dermis (Amino et al., 2006), which is an order of magnitude faster than the fastest of human cells (Lammermann et al., 2013). Classical actin regulators of higher eukaryotes such as Arp2/3 complex proteins, as well as cross-linking, branching and nucleation promoting factors are absent in Apicomplexa (Gordon and Sibley, 2005; Schuler and Matuschewski, 2006).

Actin

Apicomplexan actin is divergent from that of other eukaryotes (Wesseling et al., 1988). *Plasmodium* encodes two actin isoforms that share approximately 80 % sequence identity with homologues from yeast or vertebrates (Vahokoski et al., 2014). *Plasmodium* actin I, which is expressed throughout the life cycle, forms only short filaments (Sahoo et al., 2006; Schmitz et al., 2010; Schuler et al., 2005b) and features a differently structured filament with a larger pitch than rabbit muscle actin (Schmitz et al., 2005). *Plasmodium* actin II polymerizes into longer filaments (Vahokoski et al., 2014) but is only present in the gametocyte and mosquito stages including sporozoites (Lindner et al., 2013), although the transcript has been shown to be absent in sporozoites (Andreadaki et al., 2014). The rapid turnover of short actin filaments and the intrinsic instability makes visualization challenging. Previous attempts to visualize F-actin within the parasites have largely been unsuccessful, since conventional actin labelling techniques such as Life-Act, Phalloidin and SiR-Act do not allow detection and even cryogenic electron tomography failed to detect F-actin within the parasites (Kudryashev et al., 2010a). But recently, actin filaments have been visualized in intracellular *T. gondii* tachyzoites linking

individual parasites within the vacuole by using actin-chromobodies (Periz et al., 2017) which are currently being tested in *Plasmodium*.

Actin-binding-proteins

The dynamic actin filament turnover in apicomplexan parasites is organized by a limited number of actin-binding proteins (Sattler et al., 2011). Formins have been shown to bind at the barbed end and nucleate actin filaments (Baum et al., 2008). Sequestration of G-actin is facilitated by profilin, which was reported to bind actin monomers through a unique arm domain thereby controlling actin polymerization (Moreau et al., 2017; Skillman et al., 2012). It was demonstrated that the actin depolymerizing factors (ADF 1 and 2) stimulate nucleotide exchange inducing disassembly of F-actin, while ADF1 exclusively binds to G-actin (Schuler et al., 2005a; Singh et al., 2011). Cyclase-associated protein (CAP) was shown to bind ADP-G-actin and catalyze the nucleotide exchange from ADP to ATP thereby recycling actin monomers for new rounds of polymerization (Hliscs et al., 2010; Makkonen et al., 2013). Barbed end capping by capping protein (CP) was found to be essential for fast filament turnover (Ganter et al., 2009) and coronin was suggested to be responsible for organizing actin filaments into parallel bundles (Bane et al., 2016; Olshina et al., 2015).

MyoA

The current model of gliding motility envisions a linear model with an apicomplexa-specific myosin XIV, myosin A (Meissner et al., 2002), which is anchored to the outer IMC membrane by a myosin light chain (MLC), called MTIP in *Plasmodium* (Bergman et al., 2003) or MLC1 in *Toxoplasma* (Herm-Gotz et al., 2002). Two more *T. gondii* MyoA MLCs have been described, named essential light chains (ELC) 1 and 2 and a more recent paper suggested an additional myosin light chain required for motility (Green et al., 2017). A number of glideosome-associated proteins (GAPs) GAP40, GAP45, GAP50 and members of the GAPM family have been described to stabilize the myosin motor (Bullen et al., 2009; Frenal et al., 2010; Johnson et al., 2007). GAP45 was reported to act as a molecular tether between the IMC and the PM, maintaining a critical distance between the two membrane systems (Frenal et al., 2010). The myosin molecules are thought to pull on actin filaments driving connected surface proteins bound to the substrate rearwards resulting in a forward movement of the parasite (Figure 7).

Previously, the glycolytic enzyme aldolase was suggested to act as bridge between the cytoplasmic tails of adhesins and the actin filaments (Jewett and Sibley, 2003; Starnes et al., 2009). The role of aldolase has since been shown to be nonessential (Shen and Sibley, 2014), while a more recent paper proposed a new connector (Jacot et al., 2016). To disengage adhesive interactions between parasite and substrate, adhesions were shown to be cleaved off through the action of a rhomboid protease (Ejigiri et al., 2012) which releases the extracellular domain.
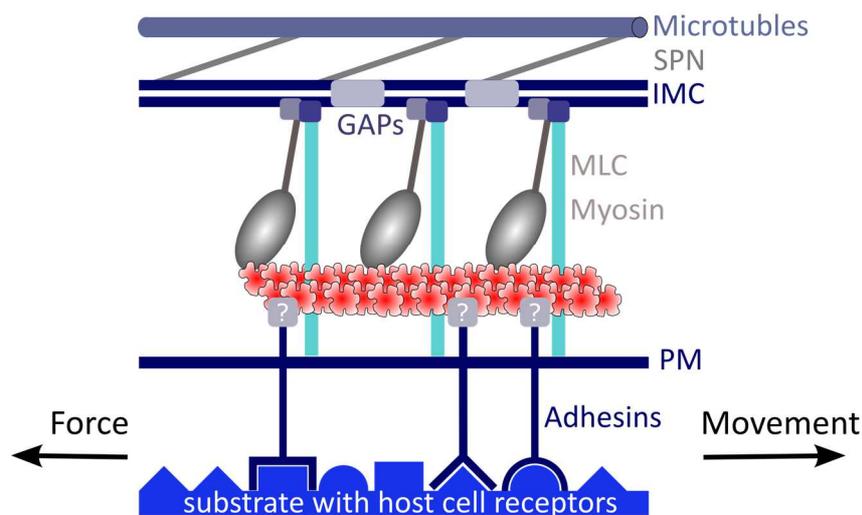
Figure 7: Molecular motor model at the host-pathogen interface: Actin filaments (red) are driven rearward within the parasite by myosin (gray) and linked via surface adhesin molecules (dark blue) that mediate contact with the host cell or substrate (light blue). The parasite motor is located in the space between the parasite plasma membrane and the inner membrane complex (IMC). Microtubules, IMC associated proteins and subpellicular network support the structure from underneath. The power stroke of the single headed myosin generates the force on the actin filament, which is transferred via the transmembrane TRAP-family proteins to a substrate. A myosin light chain (MLC) anchors MyoA with glideosome-associated proteins (GAPs) in the IMC. The Myosin interacts with short actin filaments that in turn are linked to the cell surface via an unknown linker.

The above described linear motor model has been challenged by studies that have knocked out key proteins associated with glideosome function in the related Apicomplexan parasite *T. gondii*, that were previously thought to essential (Andenmatten et al., 2013; Egarter et al., 2014). This underlines the complexity of the system and suggests, that the molecular motor might not be conserved completely in both organisms.

1.4.3 Actin-modulating drugs

Apicomplexan motility can be disrupted with drugs targeting the actin - myosin motor. The membrane-permeable compound jasplakinolide (Jas), which is produced by marine sponges, acts by stabilizing actin filaments (Cramer, 1999). While high concentrations of Jas disrupt cell

invasion and motility (Poupel and Tardieux, 1999) and lead to formation of a prominent apical protrusion (Shaw and Tilney, 1999), treatment with low dosages increased gliding speed in *T. gondii* tachyzoites, but only in an unproductive way with randomly oriented actin filaments (EM-data) (Wetzel et al., 2003). The stabilizing effects of jasplakinolide (Bubb et al., 1994) could result in longer as well as more numerous actin filaments. The addition of Jas lengthened *Tg* actin filaments *in vitro* from 100 nm to 240 nm (Sahoo et al., 2006), however Jas-treatment of live tachyzoites caused problems as it may have led to either the wrong orientation of the filaments or polymerization with no preferential direction (Stadler et al., 2017).

Cytochalasin D, a fungal alkaloid and actin-filament-disrupting drug prevents filament growth by blocking polymerization at the barbed end resulting in short filaments (Cooper, 1987). CytoD inhibits parasite motility and invasion in *Apicomplexan* parasites (Dobrowolski and Sibley, 1996; Wetzel et al., 2005). Inhibition of actin polymerization reduces forces and abrogates polarity in *T. gondii* tachyzoites (Stadler et al., 2017) .

In *Plasmodium*, gliding speeds were highest at low concentrations of Jas, but decreased with increasing concentrations for Jas and CytoD (Munter et al., 2009). At high concentrations of both inhibitors, sporozoites stopped moving. Treatment with CytoD leads to firm attachment, while Jas caused detachment of sporozoites from the substrate (Hegge et al., 2010).

1.4.4 Surface proteins

Initiation of gliding motility has been linked to the interaction of serum albumin (Vanderberg, 1974) or peptides containing motives (arginine-glycine-aspartic acid (RGD)) present in ECM proteins (Perschmann et al. 2011). These interactions trigger a signaling cascade via Ca^{2+} that leads to secretion of micronemal proteins including thrombospondin-related anonymous protein (TRAP) family (Carey et al., 2014).

The TRAP family consists of five proteins TRAP, MTRAP, TLP, CTRP and S6/TREP/UOS3 (Figure 8) that are expressed in different stages of the *Plasmodium* life cycle (Morahan et al., 2009). In the following, I am going to focus on the proteins relevant for sporozoite motility and invasion. TRAP family proteins have common structural features like adhesive domains, *i.e.* the von Willebrand factor A-domain (A-domain) (Whittaker and Hynes, 2002) and the thrombospondin type I repeat (TSR) (Tucker, 2004) including a signal peptide at the N-terminus and a short cytoplasmic tail domain (CTD) (Kappe et al., 1999). A micronemal

targeting signal motif with the sequence: YXXΦ (Y represents tyrosine, X can be any amino acid and Φ represents a hydrophobic amino acid) is located between the transmembrane domain and the CTD which ensures correct protein transport to the micronemes (Bhanot et al., 2003; Di Cristina et al., 2000). A second motif located at the extracellular side of the transmembrane region is important for proteolytic cleavage by rhomboid proteases to disengage adhesive interactions between parasite ligands and host cell receptors at the rear of the cell (Baker et al., 2006; Ejigiri et al., 2012). It has however not been shown whether all TRAP-family proteins are proteolytically processed.
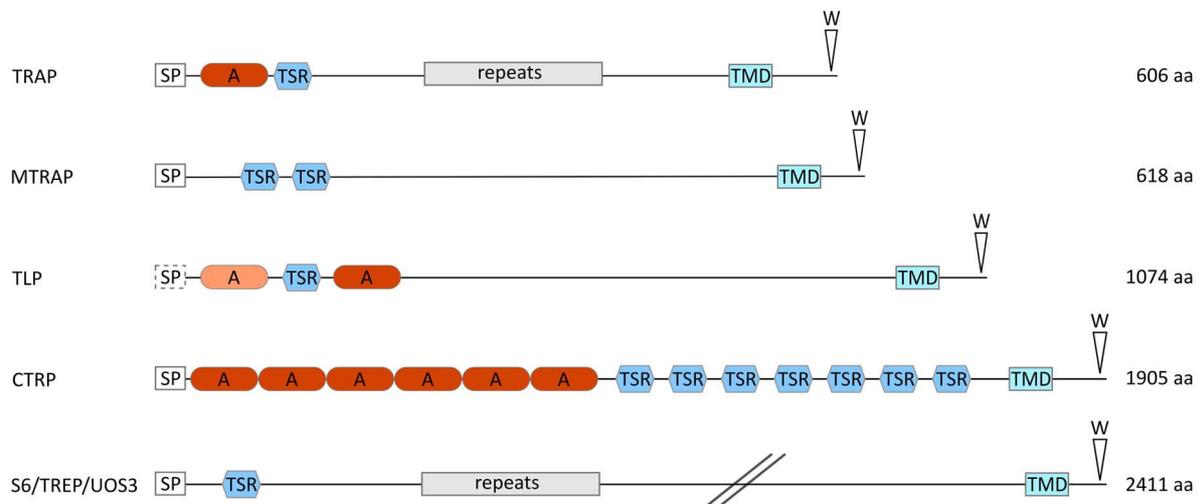
Figure 8: Topology of TRAP-family proteins in *Plasmodium spp*. The Integrin-like A-domains (A) are highlighted in red and thrombospondin type I repeats in blue. Signal peptides (SP) at the N-terminus are drawn in white, transmembrane domain (TMD) at the C-terminus in turquoise. Conserved tryptophan (W) at the C-terminus are indicated by arrow heads. Note: orange A-domain in TLP is less conserved and probably non-functional. The signal peptide of TLP (dashed box) has been predicted as second transmembrane, but has not been supported experimentally. The protein length as number in amino acids (aa) refers to the *Plasmodium berghei* ANKA strain. Protein lengths are not drawn to scale

Sporozoites lacking TRAP no longer invade salivary glands indicating a role in host cell invasion (Sultan et al., 1997). Mutations at the cytoplasmic tail of this protein - at the penultimate tryptophan residue or at the negatively charged region - show aberrant gliding motility suggesting that TRAP links extracellular interactions with the interior to modulate motility (Kappe et al., 1999). Mutations in the extracellular domains of TRAP did not affect gliding motility, but impaired salivary gland entry and sporozoite infectivity. (Matuschewski et al., 2002).

S6 (sporozoite gene 6) / TREP (TRAP-related protein (TREP) / UOS3 (upregulated in oocyst derived sporozoites 3) contains only one TSR domain and is significantly longer than the other TRAP family proteins and is expressed during sporozoite release from oocysts and in

hemolymph sporozoites (Mikolajczak et al., 2008). Deletion of S6/TREP/UOS3 results in a strongly reduced rate of salivary gland infection and a defect in substrate attachment (Combe et al., 2009; Hegge et al., 2010; Steinbuechel and Matuschewski, 2009). S6/TREP/UOS3 might mediate linear cohesion, the capacity to resist forces applied along the sporozoite axis, within the initial adhesion site in hemolymph sporozoites (Hegge et al., 2012).

The TRAP-like protein (TLP) possesses one TSR and at least one A-domain, while a second A-domain might not be functional. The signal peptide of TLP has been recently re-annotated to be a second transmembrane domain (PlasmoDB), however experimental evidence supporting this is lacking. The *tlp* gene has 3325 bp and no introns and is localized on chromosome 11. The predicted protein sequence has 1074 amino acids. According to *Plasmo*GEM, TLP is dispensable in the blood stage. After successful gene disruption, the growth rate (0.95) is not significantly different from wild type (http://plasmogem.sanger.ac.uk/phenotypes) confirming data from gene deletion studies (Heiss et al., 2008; Hellmann et al., 2011; Moreira et al., 2008). After exchanging the cytoplasmic tail domain of TRAP with the tail region of TLP, sporozoites were still able to move, but salivary gland and hepatocyte invasion were not as efficient as wild type sporozoites (Heiss et al., 2008). Sporozoites without the *tlp* gene displayed continuous gliding motility, but showed decreased capacity to traverse cells which led to a reduced infectivity *in vivo* (Heiss et al., 2008; Mishra et al., 2012; Moreira et al., 2008) and delayed prepatency (Hellmann et al., 2011). Also, *tlp(-)* sporozoites have a slight deadhesion phenotype when gliding on glass substrate, which could be compensated by flow (Hegge et al., 2010) and the addition of low concentrations of Jas could partially rescue the absence of TLP on soft substrates (Hellmann et al., 2013). These findings suggest that TLP might contribute to adhesion site formation by interacting with actin filaments thereby linking the parasite motor to the environment during cell traversal or crossing of endothelial barriers.

1.5 Aim of this work

The goal of this research project is to investigate the mechanism of cell motility, force development and retrograde flow in *Plasmodium* sporozoites as a minimally equipped unicellular model organism.

The current model suggests a linear motor, in which a single-headed myosin and short actin filaments enable dynamic turnover for fast gliding motility. The questions of how actin is organized, force is produced and transmitted via transmembrane proteins were addressed in this thesis. Also, the function of a sporozoite surface protein, TLP is the focus of this thesis and was investigated using optical tweezers, reverse genetics, *in vivo* studies as well as live cell microscopy.

Further, I used an Atomic Force Microscope to investigate the knob formation and morphology on *P. falciparum*-infected erythrocytes. This work is part of a collaboration with the group of Prof. Lanzer assessing the knob density on infected erythrocytes and correlating the results with the number of *Pf*EMP1-molecules expressed on the surface via FACS analysis. In addition, I analyzed knobs in number and size on infected erythrocytes with different hemoglobin variants contributing to the understanding of the protective mechanism for heterozygotes carriers.

2 Materials & Methods

2.1 Equipment and Software

AFM

JPK Nano Wizard III	JPK, Berlin, Germany
JPK processing software	JPK, Berlin, Germany
AFM cantilever	Nanosensors, PPP-NCLR-50, Switzerland

Wide-field epifluorescence microscope

Axiovert 200 M with XL-3 incubator	Carl Zeiss, Jena, Germany
Axiovision 4.6. software	Carl Zeiss, Jena, Germany
CoolSnap HQ2 high resolution CCD	Photometrics, Tucson, AZ, USA

Spinning disc confocal microscope

UltraView spinning disk confocal unit	Perkin Elmer, Waltham, USA
Eclipse Ti-E inverted microscope	Nikon, Tokyo, Japan
back-illuminated EMCCD ImagEM X2	Hamamatsu, Hamamatsu, Japan
sCMOS Orca Flash4	Hamamatsu, Hamamatsu, Japan
Volocity 6.1.1.	Perkin Elmer, Waltham, USA

Optical Tweezer Systems

CellManipulator	MMI, Eching, Germany
Eclipse Ti-E inverted Microscope	Nikon, Tokyo, Japan
CFI Plan Fluor DLL 100x, NA 1.3 ph3	Nikon, Tokyo, Japan
8 W Ytterbium fiber laser, 1070 nm	MMI Eching, Germany
CCD camera	Cellcamera MXF285c, MMI, Eching, Germany
Optical table	VH3660W-OPT, Newport, Irvine, CA, USA
Software	mmiCellTools 4.5 software, Eching, Germany

Material and Methods

Holographic Optical Tweezers	self-built system, University of Heidelberg
Bright field and fluorescence microscopy setup	Alpha SNOM platform, Witec, Ulm, Germany
Universal Plan Apochromat 60x, NA 1.2	Olympus, Center Valley, PA, USA
5 W Nd:YVO$_4$ laser, 1064 nm	J20-BL-106C, Spectra Physics, Mountain View, CA, USA
CCD camera	Axiocam, Zeiss, Oberkochen, Germany
Fluorescence camera	Retiga EX, 12 bit (QImaging, Surrey, Canada
Highspeed camera	Phantom V7.2 Vision Research, Wayne, NJ, USA
Optical table	VH3648W-OPT, Newport, Irvine, CA, USA
MATLAB software	The MathWorks Inc., Massachusetts, USA
Software	LabVIEW, National Instruments, Texas, USA

Equipment

Amaxa Nucleofector II	Lonza, Cologne, Germany
Analytic scale TE1245-OCE	Sartorius, Göttingen, Germany
Autoclave	Holzner, Nußloch, Germany
Binocular Nikon SMZ 1500	Nikon, Tokyo, Japan
CCD camera EASY 440 K	Herolab, Wiesloch, Germany
Centrifuge 5417 R (cooled)	Eppendorf, Hamburg, Germany
Centrifuge Heraeus	BioFuge pico DJB Labcare, Buckinghamshire, UK
Centrifuge Heraeus	Laborfuge 400e Thermo Fisher Scientific, Waltham, USA
Centrifuge Heraeus	Multifuge 1 S-R DJB Labcare, Buckinghamshire, UK
E.A.S.Y Win 32	Herolab, Wiesloch, Germany
Freezer -80°C	New Brunswick Scientific, Edison, USA
Freezer -20°C	Liebherr, Ochsenhausen, Germany

Material and Methods

Heating block MBT 250	Kleinfeld Labortechnik, Gehrden, Germany
Heating block	Thermomixer compact Eppendorf, Hamburg, Germany
Ice machine	Scotsman, Pogliano Milanese, Italy
Incubator CO_2	MCO-17AI Sanyo, München, Germany
Incubator	Innova 400 shaker New Brunswick Scientific, Edison, USA
Incubator	Multitron 2 Infors Incubator, Bottmingen, Switzerland
Liquid Nitrogen tank	ARPEGE 170 Air Liquide, Düsseldorf, Germany
Magnetic stirrer	Carl-Roth, Karlsruhe, Germany
Microwave oven (Micromaxx)	Medion, Essen, Germany
Mini-PROTEAN Electrophoresis Cell	Bio-Rad Laboratories GmbH, München, Germany
Restraining tube for mice	In house production, University of Heidelberg, Germany
Neubauer chamber improved	Brand, Wertheim Optical table Newport, Irvine, USA
Pipettes (L20, L200, L1000)	Labmate, St. Albans. UK
Pipette 0,2-2 µl	Gilson, Middleton, USA
Pipettus SWIFTPET	ABIMED, Langenfeld, Germany
PH-meter	Hanna Instruments, Kehl, Germany
Scale EW600-2M	Kern, Balingen, Germany
Sterile Workbench Herasafe	Thermo Fisher Scientific, Waltham, USA
Sterile Workbench BSB 6	Gelaire, Sydney, Australia
Mastercycler ep Gradient	Eppendorf, Hamburg, Germany
Mosquito cages	BioQuipProducts, Rancho Dominguez,USA
Timer	Oregon Scientific, Neu-Isenburg, Germany
UV-table UVT-28 L	Herolab, Wiesloch, Germany

Vacuum pump N86KN.18	KNF Neuberger GmbH, Freiburg, Germany
Vortex-Genie 2	Scientific Industries, Bohemia, USA
Water bath Isotemp 210	Thermo Fisher Scientific, Waltham, USA

2.2 Disposables and chemicals

1 kb DNA ladder	New England Biolabs, Ipswich, USA
5-Fluorocytosine (5-FC)	Sigma-Aldrich, München, Germany
96 well optical bottom plates	nunc, Rochester, USA
α-GFP antibody, ABfinity	ThermoScientifc, Waltham, USA
AccuPrep® Plasmid Mini Extraction Kit	Bioneer, Daejeon, Republic of Korea
Acetic acid CH_3COOH	Carl Roth, Karlsruhe, Germany
Agar	Bacto^{TM} Agar, BD, Heidelberg, Germany
Agarose	UltraPure ^{TM}Agarose, Invitrogen, Thermo Fisher Scientific
Alexa Fluor 594 goat anti-rabbit IgG antibody	Invitrogen, Karlsruhe, Germany
Alsever's solution	Sigma Aldrich, München, Germany
Amaxa TM Human T Cell Nucleofector^{TM} Kit	Lonza, Cologne, Germany
Ampicillin sodium salt	Sigma Aldrich, München, Germany
Bromophenol blue	AppliChem, Darmstadt, Germany
Bovine Serum Albumin, BSA fraction V	Carl Roth, Karlsruhe, Germany
Cannulas	BD Microlance^{TM} 3, 27G Nr. 20 0.4 x 19 mm, Sigma Aldrich, München, Germany
Cell culture flask 250ml	Greiner bio-one, Frickenhausen, Germany
CIP Alkaline Phosphatase	New England Biolabs, Ipswich, USA
Cover slip round	diameter 12 mm, 0.13-0.16 mm thickness (No. 1), Marienfeld.
Cover slip square	24 x 24 mm, 0.13-0.16 mm thickness (No. 1), Marienfeld, Germany
Cover slip rectangular	24 x 60 mm, 0.13-0.16 mm thickness (No. 1), Marienfeld, Germany
Cryovials CRYO.S	Greiner bio-one, Frickenhausen, Germany

Material and Methods

Cytochalasin D	Sigma Aldrich, München, Germany
D (+)- Glucose	Carl Roth, Karlsruhe, Germany
Dimethyl sulfoxide (DMSO)	Sigma Aldrich, München, Germany
DNeasy Blood & Tissue Kit	Quiagen, Hilden, Germany
dNTP Mix 2 mM	MBI Fermentas, Burlington, USA
dmH_2O demineralized water	In house supply, University of Heidelberg
double-sided sticky tape	tesa, Beiersdorf company, Germany
Eppendorf tubes (1.5 ml, 2.0 ml)	Sarstedt, Nürnbrecht, Germany
Erlenmeyer flasks (various sizes)	Schott, Mainz, Germany
Ethylenediaminetetraacetic acid (EDTA)	Thermo Fisher Scientific, Darmstadt, Germany
Ethanol 100 %	Sigma Aldrich, München, Germany
Ethanol 96 %	Zentrallager, Heidelberg, Germany
Falcon tubes (15 ml, 50 ml)	Greiner bio-one Frickenhausen, Germany
FBS US Fetal bovine serum	certified, US origin, Gibco™, Thermo Fisher Scientific, Darmstadt, Germany
FBS Fetal bovine serum	qualified, E.U.-approved, South America origin, Gibco™, Thermo Fisher Scientific, Darmstadt, Germany
Finder grids	Maxtaform Grids, Pennsylvania, USA,
Gentamycin (10 mg/ml)	PAA, Pasching, Austria
Giemsa stain	Giemsa's azur eosin methylene blue solution Merck, Darmstadt, Germany
Glass slide	76 x 26 mm, 1 mm thickness, Marienfeld, Germany
Glycerol 98 %, water free	Sigma-Aldrich, München, Germany
Gloves nitrile	VWR, Darmstadt, Germany
Gloves latex	Hartmann, Heidenheim, Germany
Hoechst 33342	Thermo Fisher Scientific, Waltham, USA
Heparin-Natrium 25000 U	Ratiopharm, Ulm, Germany
High Pure PCR Product Purification Kit	Roche, Mannheim, Germany

Material and Methods

Immersion oil	Carl Zeiss, Jena, Germany
Insulin syringe U-100 1 ml	Bran, Melsung, Germany
IPTG Isopropyl-β-D-thiogalactopyranosid	Carl Roth, Karlsruhe, Germany
Jasplakinolide	CalBiochem, La Jolla, USA
Ketamine hydrochloride solution 10%	Bremer Pharma, Warburg, Germany
Loading dye purple (6x, for agarose gels)	MBI Fermentas, Burlington, USA
Methanol 99,8%	Sigma-Aldrich, München, Germany
Midori green	DNA/RNA dye, Nippon Genetics Europe, Germany
Nail polish	drugstore, dm, Heidelberg, Germany
Nycodenz ®	Axis-shield, Heidelberg, Germany
2-Propanol	Sigma-Aldrich, München, Germany
Paraffin	Carl Roth, Karlsruhe, Germany
Parafilm	Pechiney plastic packaging, Menasha, USA
Paraformaldehyde (PFA)	Riedel-de Haën AG, Seelze, Germany
Pasteur capillary pipettes	WU, Mainz, Germany
PCR tubes, 8-strips	G. Kisker GbR, Steinfurt, Germany
PC-S-1,5 streptavidin-polystyrene microparticles	G. Kisker, Steinfurt, Germany
Penicillin/Streptomycin 100x	PAA, Pasching, Austria
Pestle	Compatible with 1.5 ml tubes, Bel-Art™ SP Scienceware™
Phenylhydrazine 97 %,	Sigma-Aldrich, München, Germany
Petri dish	Greiner bio-one Frickenhausen, Germany
pGEM-T Easy Vector Systems	Promega, Madison, USA
PBS with Ca^{2+} & Mg^{2+}	PAA, Pasching, Austria
Plastic Pipettes (5 ml, 10 ml, 25 ml)	Greiner bio-one Frickenhausen, Germany
5x Phusion GC & HF buffer	Thermo Fisher Scientific, Waltham, USA
Phusion polymerase	Thermo Fisher Scientific, Waltham, USA
Pipette tips	Gilson, Middleton, USA
Potassium chloride, KCl	Merck, Darmstadt, Germany

Primer	Thermo Fisher Scientific, Darmstadt, Germany
ProLong® Gold Antifade Mountant,	Thermo Fisher Scientific, Darmstadt, Germany
Pyrimethamine	Sigma Aldrich, München, Germany
Restriction enzymes	Supplied with recommended buffers, NEB, Ipswich, USA
RPMI 1640	Gibco™, Thermo Fisher Scientific, Darmstadt, Germany
Saponin	Quillaja bark extract, 20-35% sapogenin content, Sigma Aldrich, München, Germany
Sodium chloride, NaCl	Sigma Aldrich, München, Germany
Sodium dihydrogen phosphate, NaH$_2$PO$_4$	J.T. Baker, Phillipsburg, USA
Millipore® Stericup™ filter units, 0.22 µm	Millipore, Merck, USA
Syringe (1 ml, 5 ml)	BD Plastipak™, Heidelberg, Germany
Sytox Orange	Invitrogen, Karlsruhe, Germany
T4 DNA Ligase	Promega, Wisconsin, USA
Taq DNA Polymerase	Thermo Fisher Scientific, Darmstadt, Germany
Tris	Carl Roth, Karlsruhe, Germany
Triton X-100	Merck, Darmstadt, Germany
Tryptone	Bacto™ Tryptone, BD, Heidelberg, Germany
Uncoated flow chamber µ-slide I	ibidi GmbH, Martinsried, Germany
X-Gal	Neolab, Heidelberg, Germany
XL1-Blue competent cells (*E. coli*)	Agilent Technologies, Santa Clara, USA
Xylazine hydrochloride 20 mg/ml	Xylariem, Ecuphar, Greifswald, Germany
Yeast Extract	Bacto™ Yeast extract, BD, Heidelberg, Germany

2.3 Buffers and solutions

5-FC solution	dissolved 1 mg/ml 5-FC in warm tap water.
Blocking solution	2 % BSA in PBS
DNA loading buffer (6x stock solution)	125 mg bromophenol blue
	35 ml dmH$_2$O
	15 ml glycerol
Fixation solution	4 % PFA in PBS
Freezing solution	5 ml Glycerol
	in 45 ml Alsever's solution
Giemsa staining solution	7,5 ml Giemsa stain in 50 ml of tap water
Ketamine / Xylazine	25 mg/ml Ketamine
	2.5 mg/ml Xylazine
	in PBS
Lysogeny broth (LB)	10 g NaCl
	10 g Bacto™ Tryptone
	5 g Bacto™ Yeast extract
	dissolved in 1 l of dmH$_2$O and autoclaved at 121°C for 20 min.
LB agar	15 g of Bacto™ agar was added to the recipe above. After autoclaving, the mixture had to cool to 50°C before the respective antibiotics were added and the plates cast
Nycodenz solution	

Stock solution (100 %):	138 g Nycodenz ®
	394 mg Tris-HCl
	112 mg KCl
	56 mg Na_2EDTA
	This was filled up to 500 ml with Millipore water and stirred for 2-3 h at RT until dissolved completely, adjusted pH to 7,5 using 5 M KOH or HCl. The solution was autoclaved for 20 min at 121°C and stored at 4°C.
Working solution (55 %):	Mix 27,5 ml Nycodenz® solution with 22,5 ml PBS ($+Ca^{2+}$& Mg^{2+})
Permeabilization solution	0.2% Triton X-100 in blocking solution
Phosphate buffered saline (PBS)	8.0 g NaCl
	0.2 g KCl
	1.42 g Na_2HPO_4
	Dissolved in 1 l dmH_2O and adjusted pH to 7.4
Pyrimethamine drinking water	
Stock solution (7mg/ml):	350 mg Pyrimethamine were dissolved in 50 ml of DMSO.
Working solution (0.07 mg/ml):	Stock solution was diluted 1:100 with tap water and adjusted to pH 4.8 with HCl.
RPMI-1640 + Pen/Strep	500 ml RPMI-1640
	5 ml Penicillin/Streptomycin (100x)
Saponin stock solution	2.8% (w/v) Saponin in PBS

Transfection medium (T-medium)   15 ml FCS (US)

60 ml RPMI containing 25 mM HEPES

22.5 µl Gentamicin

Mixed and sterile-filtered and kept at 4°C

TAE buffer

50x stock solution   242 g Tris base in water

57.1 ml glacial acetic acid

100 ml of 500 mM EDTA (pH 8.0)

Filled up to 1 l and diluted 1:50 for a 1xTAE

working solution.

2.4 Optical tweezers

Optical Tweezers (OT) are able to manipulate microscopic objects by the power of light. For stable trapping of transparent microparticles a steep optical gradient is needed. For this, an objective with high numerical aperture (63x water immersion NA 1.2) (Nambiar et al., 2010) focuses the incoming laser beam to the focal plane, creating the required gradient leading to a 'restoring force' on the trapped microparticle as it is displaced from the trap center due to Brownian motion or an external force.

The experiments were performed on custom-built combined optical tweezers and fluorescence microscopy setup (Hegge et al., 2012; Streichfuss et al., 2011; Uhrig et al., 2009). In order to avoid thermal heating by absorption of the incident light, a wavelength of 1064 nm was chosen. In this wavelength regime, water and therefore most biological samples are highly transparent and thus are not heated significantly.

2.4.1 Stokes Calibration for force experiments

Since not all physical parameters of the optical tweezer setup are known exactly, the trapping potential needs to be determined empirically. The calibration was performed in a sealed custom-made microfluidic chamber consisting of two coverslips. The bottom coverslip was coated with polydimethylsiloxane (PDMS) and contained a channel with dimensions of 0.5 × 15 × 0.1 mm W × D × H. Two holes into the top coverslip for the in- and outlet tubing. Before assembly, both coverslips were plasma-treated enabling a stable and tight sealing. Inlet and outlet holes of the PDMS channel were connected to the loading reservoir and a syringe pump. The bead containing solution was loaded into the channel from the reservoir by the syringe pump. The pump pulled at a constant rate and thus generated the desired steady flow speed needed for precise force calibration.

For this experimental set up, we choose the Stokes calibration method which allows escape force determination. For small displacements of the bead from equilibrium position, there is a linear relation between force and displacement (Hooke's law). Since the escape occurs beyond the linear region of the trap, the spring constant calibration is not adequate. The escape force can be measured by applying a steadily increasing force until the particle escapes from the trap. The external force, in this case the Stokes' drag is induced by a constant flow

past the trapped particle. The escape force (F_{stokes}) is determined at the speed of the flow (v) at which the bead is displaced from the trap center using this formula:

$$F_{Stokes} = 6\pi r \eta v$$

r = radius of the microparticle [1 μm]

η = viscosity of water [1 mPa s]

v = flow velocity (μm/s)

In order to achieve reliable results, this procedure was repeated several times. To verify these results, two complementary approaches were used to obtain the escape force at specific velocities (Figure 9). In the first approach, a bead was trapped with high laser power from a medium with a low concentration of beads (Figure 9 A). Subsequently, the laser power and thus the trap stiffness was gradually reduced by lowering the diode current (Figure 9A I+II). As soon as the Stokes force became stronger than the optical force, the bead escaped the laser trap due to the Stokes drag (Figure 9B III).

In the second approach, we used a medium with higher concentrations of beads (Figure 9 B). The optical potential was adjusted until the trapping force equaled the Stokes force of the beads in the moving medium (Figure 9B I+II). This force equilibrium was obtained as beads moving through the trap center were trapped for a short time, but escaped the trap rapidly (after several ms) assisted by Brownian motion (Figure 9B III).

For both approaches, the flow speed (v) of the escaped beads was measured by tracking beads in the same focal plane close to the glass surface at similar distances used in subsequent experiments. This is important as the trapping force depends on the distance the trap to a surface. By knowing the flow speed (v) at a certain laser power, we could determine the corresponding escape force.
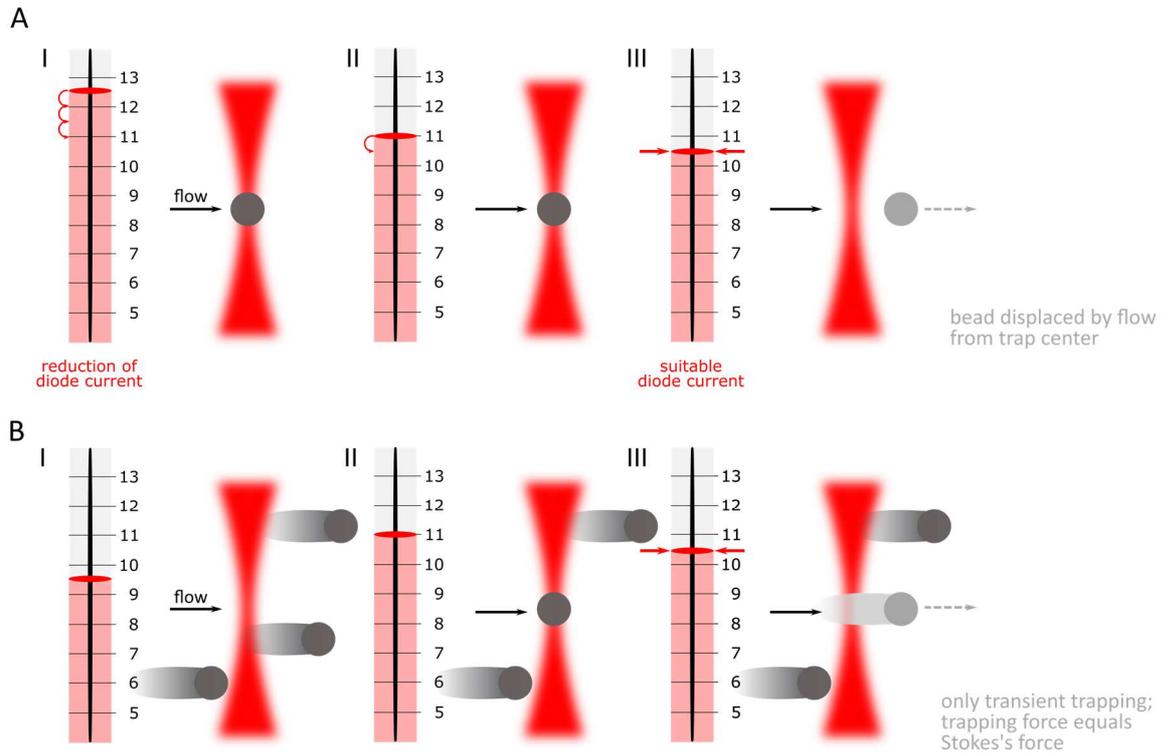
Figure 9: Stokes calibration using two complementary approaches. (A) First approach: Trapping bead with high laser power (I) and gradually reducing laser intensity (II) until bead pulled out by the stokes force displaced out of the trap center by constant flow (III). (B) Second approach: Starting with a higher bead concentration, laser intensity is varied (I+II) until bead is only briefly trapped in the laser focus and immediately displaced again due to Brownian motion (III).

The conducted calibration of the optical tweezers allows for quantification of the escape forces in the subsequent experiments. In force experiments we tested the sporozoites capability to overcome a force of 70, 130 and 190 pN corresponding to laser currents of 10, 11 and 12 A, respectively.

2.4.2 Sample preparation

For optical tweezer experiments, an open flow cell was prepared consisting of two coverslips (60 × 24 mm bottom and 24 × 24 mm top) spaced by two stripes of double-sided sticky tape forming a reservoir of about 30 µl (Figure 10). Salivary glands were dissected into a volume of 40 µl RPMI/ 3 %BSA and kept on ice. After releasing the sporozoites from the salivary glands, the sporozoite suspension was applied to the flow chamber and the sporozoites were allowed to attach for 10 min. As soon as the sporozoites settled and started to move in circles, a bead solution was added to one side of the flow cell and pulled through the flow chamber by applying capillary forces created by tissue paper on the opposite side. To ensure that the entire volume of the chamber was exchanged, we replaced the medium of the chamber with twice the volume. Depending on the experiment, the bead solution consisted of either RPMI/ 3 % BSA alone or additional actin modulating compounds like cytochalasin D, or jasplakinolide at low concentrations (50 nM, 200 nM). Sporozoites were incubated with the compounds for 5- 10 minutes before the experiment was performed.

sporozoite solution
applied to open end of flow cell

flow cell: channel
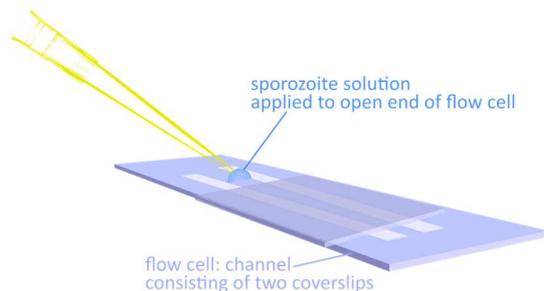consisting of two coverslips

Figure 10: Sample preparation. Schematic illustration of an open flow cell built with two coverslips spaced by two stripes of double-sided sticky tape forming a channel. The empty flow cell is loaded with sporozoite solution by adding it to one end of the flow cell. Subsequently it is pulled into the channel by capillary forces. After 10 min of incubation, the bead solution is applied and pulled through the flow cell with tissue paper substituting the previous volume.

2.4.3 Experimental procedure

The HOT was here used with a stationary optical trap. By moving the microscope stage and thereby the flow chamber in the x–y plane, floating beads were caught from the bead solution and remained stationary in the field of view while gliding sporozoites attached to the bottom coverslip surface moved beneath the trapped particle. The optically trapped bead was then positioned above the front end of the gliding sporozoite and subsequently lowered onto the top of sporozoite in z-direction using the piezo stage, until sporozoite and bead were both in focus.

2.4.4 Retrograde flow experiments

For investigating the transport speed of beads along the sporozoite, beads were merely held with the lowest laser power (9 A corresponding to around 10 pN and just above the limit needed to keep beads from escaping due to Brownian motion) possible. As soon as bead and sporozoite were brought into contact, all sporozoites pulled the bead out of the center of the laser trap. The sporozoites translocated the bead toward their posterior end. Sporozoites were only probed once to minimize potential laser-induced damage (Hegge et al., 2012). Retrograde flow movies were imaged with a framerate of 60–100 Hz. The positions of the beads were extracted from the recorded images by particle tracking using Griers MATLAB routines (Crocker and Grier, 1996). The calculated speeds were smoothened with a moving average of 333 ms width.

2.5 Atomic Force Microscope

The Atomic Force Microscope is a member of the scanning probe microscope family and was invented by Binnig, Quate, and Gerber, in 1986 (Binnig et al., 1986). Atomic-scale imaging was obtained within the first year of the invention (Binnig et al., 1987), but it took a few years before atomic imaging of nonconductive surface was achieved, which facilitated investigation of biological samples. The following development to operate in liquid environments and at ambient temperatures maintaining the native state of the sample led the multifunctional analysis of biomolecules and cells at (sub-) cellular resolution (Dufrene et al., 2017).

2.5.1 AFM principle: Dynamic mode

A variety of modes to characterize biological samples have been created over the years. Dynamic mode (originally termed tapping or oscillation mode) was invented to minimalize friction and the forces applied between the tip and the sample and is therefore the most suitable AFM mode to map topography of a soft biological sample (Li et al., 2006; Moller et al., 1999). During dynamic mode, the cantilever is oscillated at or near its resonance and interacts with the sample as the probe "taps" along the surface.

Before the cantilever tip is engaged on the sample, the cantilever oscillates in free space away from the sample, close to its resonant frequency. As the tip approaches the sample surface, interactions of the cantilever tip with the sample surface cause changes in the resonance frequency and amplitude. Both, the phase shift of the resonance frequency and the oscillation amplitude can be chosen as the feedback parameter. Deviations from the setpoint, the oscillation amplitude of the cantilever at which the tip taps the sample surface, are detected and a controller counteracts these deviations. As an example, when the tip encounters a surface feature (valley or protrusion) the controller is trying to keep the feedback parameter constant at its setpoint value by adjusting the z piezo to move the cantilever tip up and down. The resulting z piezo - movements provide the height information to create the surface topography (Figure 11).
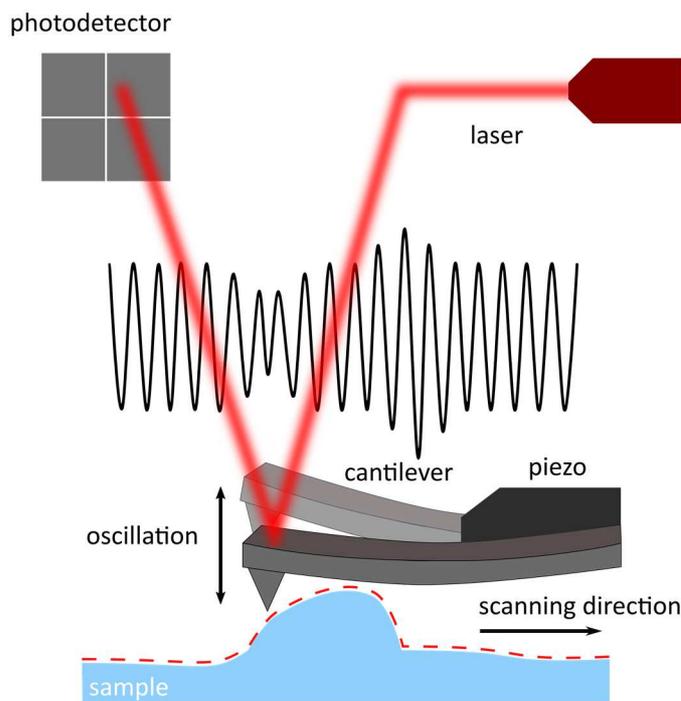

Figure 11: Illustration of AFM-based imaging of native biological sample. Cantilever is oscillated near its resonance frequency. Interaction between tip and sample change both amplitude and resonance frequency allowing them to be used as feedback parameters for contouring sample surface.

2.5.2 Sample preparation for AFM imaging

From a late-stage-dominated *P. falciparum* parasite culture, 1 ml was collected. The cell suspension was stained with 2 % filtered Giemsa solution, incubated for 10 min and subsequently centrifuged at 500 x g for 3 min. About 3 µl of pellet were used to make a thin blood smear on a clean glass slide. The smear was air-dried. This simple treatment reduced the risk of artifacts to a minimum.

A grid was glued to the back of the glass slide with nail polish. The iRBCs were identified with a 40x objective at a widefield microscope and their locations on the grid were noted. The sample could then be loaded to the AFM and the scanning could be started instantly.

2.5.3 AFM imaging

AFM images were captured with the JPK Nano Wizard III mounted on an inverted microscope. Images for knob density examinations were captured in air under ambient conditions with tapping mode using a silicon cantilever with a spring constant of 21-98 N/m and a resonant frequency of 146-236 kHz. The images were 256 x 256 pixels and captured at a scan speed of 0.5-1.0 Hz depending on the scan size, which ranged from 1-10 µm. In order to minimize the noise, integral and proportional gains as well as scan speed were optimized individually.

The knob density of each iRBC was based on two separate images covering different areas, preferably where the parasite had not deformed the infected erythrocyte surface. Image sizes varied around 2,5 x 2,5 µm^2 and higher magnification around 1,7 x 1,7 µm^2. The identification of knobs was achieved by comparing the amplitude image and the height image. Previous studies have established that the knobs are uniformly distributed over the surface of the erythrocyte, irrespective of the parasite developmental stage or erythrocyte surface topography. This validates a global density determination based on these minor areas (Arie et al., 2005; Nagao et al., 2000). From knob height and diameter values, the knob surface was calculated using the formula of a spherical cap:
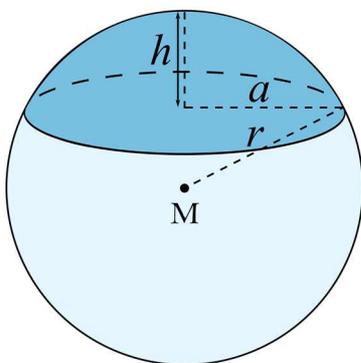
$$spherical\ cap = \pi(a^2 + h^2)$$

Figure 12: Spherical cap as approximation for knob surface on infected erythrocytes. M = middle point, r = radius, h = cap height, a = cap radius

2.6 Molecular biology

2.6.1 PCR

Polymerase chain reaction (PCR) is used for amplification of specific DNA fragments. Primer pairs (forward and reverse) are designed to bind at specific sites flanking the gene of interest. The length and the GC-content determine the annealing temperature. For subsequent cloning steps the restriction motives need to be attached to the primer sequences accordingly. A *Taq* polymerase was used for analyzing genomic DNA (gDNA) of transgenic parasites for integration or knock out of a specific sequence. For cloning purposes, a more accurate high-fidelity DNA polymerase (Phusion) was used to reduce errors during amplification.

Following reaction mixes where used:

Reaction mix Taq		PCR program		
0.25 µl	Primer 1	94 °C	5min	
0.25 µl	Primer 2	94 °C	30 s	
2.5 µl	10 x buffer	different annealing temp.	30 s	x 25-30 cycles
1.5 µl	MgCl$_2$	°C	1min per 1000 bp + 30 s	
2.5 µl	dNTPs	60 °C	10 min	
0.25 µl	Taq	60 °C	∞	
2 µl	gDNA	4 °C		
ad 25 µl	dm H2O			

Reaction mix Phusion		PCR program		
0.25 µl	Primer 1	98 °C	30 s	
0.25 µl	Primer 2	98 °C	10 s	
10 µl	5 x Phusion HF	different annealing temp.	30 s	x 25-30 cycles
5 µl	buffer	°C	30 s per 1000 bp	
0.5 µl	dNTPs (2 mM)	72 °C	10 min	
2 µl	Phusion	72 °C	∞	
ad 50 µl	gDNA	4 °C		
	dm H2O			

Primer design and determination of corresponding annealing temperatures were performed using the freely available software program ApE ('A plasmid Editor': http://biologylabs.utah.edu/jorgensen/wayned/ape/). All primer sequences are listed the appendix (7.1)

2.6.2 Gel electrophoresis

Separation of DNA fragments by size was done by electrophoresis in agarose gels. Gels were prepared from 0.8 - 1 % agarose solution in 1xTAE buffer. The mixture was heated until the agarose was completely dissolved and stored at 60 °C. After casting the gels and allowing them to solidify, they were placed into an electrophoresis chamber and filled with 1x TAE buffer. Samples were mixed with loading dye containing Midori Green (1:500) for visualizing the DNA and pipetted in the gel pocket. For size estimation of the DNA fragments 3 µl of a 1 kb DNA ladder was loaded onto the gel. Depending on the size of the DNA fragments, gels ran at 120-175 V for 10 - 30 min. Separated DNA fragments were visualized under UV light and documented with a CCD camera.

2.6.3 Extraction of DNA fragments from agarose gel

After electrophoresis, the desired DNA fragments were cut from the gel, melted and purified using the High Pure PCR Product Purification Kit according to the manufacturer's protocol. The DNA was eluted from the column with 35 µl of dm H_2O.

2.6.4 Restriction digest

For cloning procedures and control digests, restriction endonucleases with the respective buffer ensuring optimal reaction conditions were used to cut vector an insert. Digest reactions were incubated for at least 2 hours at 37 °C. In order to prevent re-ligation of the vector, 1 µl of calf intestine alkaline phosphatase (CIAP) was added to the reaction dephosphorylating the 5' end and incubated for 1 hour.

2.6.5 DNA Ligation

For DNA ligation, insert and vector (3:1) were incubated with 10x ligation buffer and 5 units of T4-DNA-ligase for 2 h at room temperature.
Also, the pGEM®-T Easy Vector System was used for cloning of PCR products. Since the ligation works over the AAA and TTT-overlap respectively of the DNA-fragments, PCR-products needed to be polyadenylated. The reaction mix contains 1 µl Taq DNA polymerase, 10x reaction buffer with $MgCl_2$, dATP (0.2 mM) and the purified PCR product. Demineralized water is added to

final volume of 10 µl and incubated at 70 °C for 15-30 min. For the ligation reaction 1-2 µl of the polyadenylated product were used.

2.6.6 Transformation

Plasmid amplification was achieved by transformation of bacteria. For this, 35 µl of XL1-Blue competent cells were thawed, 0.68 µl of ß-mercaptoethanol were added and the cells were incubated for 10 min on ice. Then 5 µl of the ligation product or 1 µl of a 1:100 dilution of the plasmid was added, and the cells were incubated for 30 min on ice. A heating block was pre-warmed to 42 °C, the bacteria were incubated for 50 s on 42 °C, then stored on ice for 2 more minutes. Bacteria and ligation reaction were directly plated onto LB-agar with ampicillin and incubated at 37°C overnight.

If the transformation was done with the pGEM-T easy vector, 100 µl transformation culture was transferred onto a LB/ampicillin/IPTG/X-Gal plate. After overnight incubation at 37°C, white colonies could be selected (inactivation of ß-galactosidase in case of successful cloning).

2.6.7 Liquid culture and extraction of plasmid DNA from *E. coli*

For liquid cultures, 4 ml of LB media containing the respective antibiotic were inoculating with a colony from an LB-agar plate and were placed in a shaking incubator at 37°C overnight. The extraction of plasmid DNA from *E. coli* was performed with the AccuPrep Plasmid Mini Extraction Kit according to the manufacturers protocols. Purified DNA was eluted with 35 µl dm H_2O.

There is also an alternative approach to purify DNA from bacteria: To the DNA containing solution, 1/10 of the starting volume of 3 M sodium acetate, 2.5 of the starting volume of 100 % cold EtOH and 1 µl of glycogen was added. After inverting the tube, it was cooled to -20 °C for 1 hour. The DNA becomes visible after precipitation. The solution was centrifuged for 30 min at 4 °C with 14.000 rpm and the supernatant was removed. After drying the pellet in air, it was re-dissolved in the appropriate volume with dm H_2O.

2.6.8 DNA sequencing

From a standard miniprep, 10 µl of plasmid were diluted with 25 µl of dm H_2O. If nonstandard primers were necessary, the primers were diluted 1:10 in dm H_2O. Samples were placed in the GATC drop box at DKFZ Heidelberg and sequenced by GATC, Konstanz, Germany.

2.7 Genetic manipulation of *Plasmodium berghei* parasites

2.7.1 Recipient vector

A modified vector *Pb*262 (Dennis Klug) was used as a recipient vector for cloning the different TLP tail mutants. The recipient vector (Figure 13) contains an ampicillin resistance gene for selection in bacteria (pink) and an origin of replication (black). The *human* dihydrofolate reductase (*h*DHFR; turquoise) confers resistance to pyrimethamine (positive selection). This gene is followed by 3' untranslated region (*Pb* DHFR 3' UTR; gray) and expression is driven by an ef1α-promoter (yellow). For negative selection a *y*FCU (fusion gene of the yeast cytosine deaminase and uridyl phosphoribosyl transferase, green) cassette is included as well. The *tlp* homology region lacking the C-terminus and the 3'UTR of *tlp* (both blue) were introduced to enable double homologous recombination into the *tlp* locus.
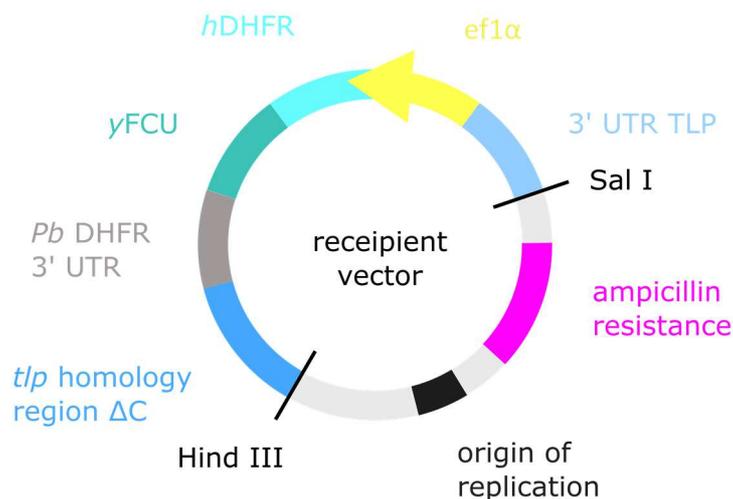

Figure 13:Vector map of modified Pb262 vector.

After successful integration of the receiver line into the endogenous locus of wild type parasites (*Pb*ANKA wild type), the TLP tail constructs with the respective mutation were introduced in a second transfection step using the "gene in marker out" strategy (Lin et al., 2011).

2.7.2 Overnight blood culture

For transfection of *Plasmodium berghei* parasites with DNA-constructs, infected mouse blood was cultured overnight to enrich the schizont stage. Under a sterile workbench 75 ml of T-medium was prepared, sterile filtered and stored. Then, 20 ml of T-medium were transferred to a culture flask and 10 ml with 250 µl Heparin were mixed in a 15 ml falcon. Both were kept at 37°C. The infected blood was gained by cardiac puncture from an infected mouse, added to the prepared falcon tube and centrifuged 8 min at 1000 rpm. The pellet was resuspended in 10 ml of T-Medium and very carefully, added dropwise to the culture flask. The culture was placed in an incubator at 37 °C, 90 % N_2, 5 % O_2 and 5 % CO_2 for 16-18 h.

2.7.3 Schizont isolation and electroporation

The overnight blood culture was subjected to density gradient centrifugation. The blood was transferred to a 50 ml falcon, underlaid with 10 ml Nycodenz (55%) and subsequently centrifuged for 25 min at 1000 rpm without brake. Purified schizonts were isolated from the interphase between Nycodenz and T-Medium with a Pasteur pipette and centrifuged for 10 min with 1000 rpm. For each transfection, 1 ml of T-Medium was added to the pellet.

For the electroporation with the Amaxa ™ Human T Cell Nucleofector ™, the linearized DNA (5 - 10 µg) was added to 100 µl of nucleofector. One ml of resuspended schizonts was centrifuged 15 s at maximum speed, the pellet resuspended in the prepared nucleofector with DNA and added to an Amaxa cuvette. After electroporation with program U33, 50 µl of T-Medium were added and the entire volume was transferred into an Eppendorf tube using an Amaxa pipette. The sample was intravenous (IV) injected in the lateral tail vein of a naïve mouse using an insulin syringe.

2.7.4 Selection for *Plasmodium berghei* transfectants

After 24 hours, the drinking water was substituted with water containing pyrimethamine (0.7 mg/ml). Parasites that contain the *h*DHFR, which confers resistance to pyrimethamine, were selected (positive selection). The negative selection based upon transgenic expression of a bifunctional protein *y*FCU (Braks et al., 2006). The drug 5-fluorocytosine (5-FC, dose 1 mg/ml) is metabolized to generate 5' fluorocytosine triphosphate (5-FCTP), a lethal analogue of CTP.

Administration of the drug takes place one day after transfection via drinking water. The drug needs to be renewed after two days. Only parasites that have lost the selection cassette survive the treatment. These parasites are then selection-marker free and could be subjected to further genetic manipulation.

2.7.5 Isolation of *Plasmodium* genomic DNA from mouse blood

To isolate gDNA from blood stages, a mouse with a respective parasitemia of ≥ 2 % was bled by cardiac puncture. For this, a 1 ml syringe was prepared by coating it with heparin, then the mouse was anesthetized. After checking for reflexes, the blood was drawn from the atrium. The blood was added to 13 ml PBS containing saponin (0.03%) and centrifuged for 8 min at 2800 rpm at 4 °C with brake. The pellet was washed with PBS and resuspended in 200 µl PBS for immediate use or storage at -20 °C. For extraction of the gDNA, the DNeasy Blood & Tissue Kit was used according to the manufacturer's protocol.

2.7.6 Limiting dilution

If genotyping using PCR of parasites gDNA confirmed correct integration after transfection, a stabilate of the parental parasite line was thawed and injected intraperitoneally (IP) into a naïve mouse. Parasitemia was monitored and did not exceed 1 %. The harvested blood was diluted to 0.9 parasites per 100 µl of PBS and 10 mice were injected IV with 100 µl each. If mice developed parasitemia, the parasites were isolated and their gDNA checked for integration via PCR.

2.8 Animal work

2.8.1 Ethics statement

All animal experiments were performed according to GV-SOLAS and FELASA standard guidelines. Animal experiments were approved by the responsible German authorities (Regierungspräsidium Karlsruhe). *Plasmodium berghei* parasites were maintained in NMRI mice that were obtained from Charles River Laboratories or JANVIER. The prepatency after sporozoite infection as well as parasite growth were determined with C57Bl/6 mice from

Charles River Laboratories or JANVIER. All transfections and genetic modifications were done in the *Plasmodium berghei* ANKA strain (Vincke and Bafort, 1968).

2.8.2 Infection of mice with *Plasmodium berghei*

After blood was taken from a mouse via cardiac puncture, stabilates containing 100 µl of infected blood and 200 µl of freezing solution were mixed, snap frozen and stored in liquid nitrogen. Thawing one of those stabilates and injecting the blood intraperitoneally (IP) into a new mouse lead to a new infection. Parasitemia was monitored by piercing the tail of the mouse with a sterile cannula and smearing a drop of blood onto a glass slide creating a thin smear of erythrocytes. The smear was fixed with 100% methanol for 10 seconds and stained in a 10 % Giemsa staining solution for at least 15 minutes. Thereafter, the slide was rinsed with tap water and analyzed under the light microscope with a 100x objective (NA 1.25 oil immersion).

2.8.3 Preparation of midgut and salivary gland sporozoites

Assessing the number of midgut and salivary gland sporozoites helps identifying a possible defect in egress from oocysts or salivary gland invasion. Sporozoites were isolated from midguts and salivary glands of infected mosquitos between day 17 and day 24 post infection. For counting sporozoites, infected salivary glands or midguts of at least 5 mosquitoes were crushed with a pestle to release the sporozoites. Free sporozoites were counted in a Neubauer counting chamber and diluted with RPMI medium. The counting chamber was loaded with 10 µl solution and sporozoites were allowed to settle for 5 min prior to counting. Sporozoites were counted using a light microscope and 40-fold magnification.

2.8.4 Infection by mosquito bites and sporozoite injections

In order to test the transmission potential of generated parasite lines, mice were infected by mosquito bites and sporozoite injections. To investigate natural transmission, mosquitoes (17 - 24 days post infection) were separated in cups of 10 each and starved for 6 - 8 h. Subsequently naïve C57Bl/6 mice were anaesthetized by intraperitoneal injection of a mixture of ketamine and xylazine. Anaesthetized mice were placed on the prepared cups and

mosquitoes allowed to bite and feed for approximately 10 min. Mosquitoes that had taken a blood meal were dissected afterwards to determine sporozoite numbers within salivary glands.

For the injection of salivary gland sporozoites, the salivary glands of mosquitoes (17 - 24 days post infection) were dissected in RPMI medium. Infected salivary glands were crushed with a pestle to release the sporozoites and diluted with RPMI medium to 100 salivary gland sporozoites per 100 µl. Sporozoite solutions were injected intravenously in the tail vein of naive C57Bl/6 mice. The parasitemia of infected mice was monitored by daily blood smears from day 3 on up to day 7. Blood smears were stained in Giemsa solution and counted using a light microscope with a counting grid. The time difference between infection and observation of the first blood stage was determined as prepatency.

2.8.5 Mosquito infection

Mosquitoes of *Anopheles stephensi* (from the FDA500 strain) were reared in the insectary of the of Center of Infectious Diseases, Department of Parasitology at Heidelberg University under standard conditions at 28 °C and 80% humidity. About 3 days before hatching of the mosquitoes, a stabilate with *Plasmodium berghei* blood stages was injected IP into a NMRI mouse. Infected mice were bled by cardiac puncture once parasitemia reached ~2% and used for a fresh blood transfer of 20,000,000 parasites each into two naïve mice. Mice that had obtained a blood transfer were kept for further 3-4 days and mosquito were allowed to feed, if at least one exflagellation event per field of view was observed.

Mosquitoes were starved prior to blood feeding by removing the sugar pad the night before. Anesthetized mice (110 µl of ketamine/xylazine solution) were placed on top of the mosquito cage for 10 minutes on each side. After the bloodmeal, mosquitoes were incubated at a constant CO_2 level, at 21 °C until needed. Mosquitoes were sustained with cotton pads soaked in either 1 % sea salt solution or 10 % sucrose solution.

2.9 Microscopy

Live microscopy of *Plasmodium berghei* sporozoites was performed with an inverted Axiovert 200M (Carl Zeiss) fluorescence microscope. The sample was illuminated using a halogen lamp

or mercury lamp with appropriate filter sets. The microscope was equipped with a CoolSnap HQ2 high resolution CCD Camera. Images were acquired using the Axiovision 4.7.2 software.

2.9.1 Immunofluorescence assay

An Immunofluorescence assay was performed to visualize GFP tagged TLP in sporozoite. For this, dissected salivary gland sporozoites were allowed to attach and glide for 20 min in RPMI/ 3 % BSA on round glass cover slips before fixation with 4 % paraformaldehyde. After 30 min incubation the samples were washed with PBS before blocking with PBS / 2 % BSA for another 30 min. In parallel a second set of sporozoites samples was treated with 0.2 % Triton-X 100 in blocking solution to permeabilize the cells. Both samples were incubated with primary antibody solution containing α-GFP antibody (rabbit monoclonal, 1:200 dilution) for 1 h at RT in the dark and subsequently washed with PBS. The secondary antibody (Alexa Fluor 594 goat anti-rabbit IgG antibody, 1:500 dilution) was added with Hoechst (1:1000 of a 10 mg/ml stock solution) and incubated for another hour. After washing with PBS, excess liquid was removed, and the coverslips were transferred upside down with mounting medium onto a glass slide. The samples were allowed to dry before examination at the Axiovert 200M fluorescence microscope with 40-fold magnification.

2.9.2 Gliding assay of sporozoites

In order to investigate possible phenotypes in adhesion and moving abilities, gliding assays were performed. Mosquitoes infected with *Plasmodium berghei* were used for investigation of salivary gland sporozoites 17-24 days post infection. The desired number of mosquitoes was taken from the cage and kept on ice for a few minutes. Unconscious mosquitoes were washed in 70 % ethanol to reduce hydrophobicity of the carapace and stored in PBS. Dissection of mosquitoes was conducted in PBS under a Binocular Nikon SMZ 1500 with GFP illumination using two G27 cannula on 1 ml syringes. The head of the mosquito was pulled off the thorax; exposed salivary glands were severed and transferred into 50 µl of RPMI on ice. After releasing sporozoites from the salivary glands by homogenizing the solution with a plastic pistil, the suspension was centrifuged for 2 min at 7000 rpm. The excess of supernatant was discarded and the sporozoites pellet was resuspended in RPMI/3% BSA and thereby activated. Sporozoite solution was added to a 96 - well plate with an optical bottom and

centrifuged for 3 min at 1000 rpm. Gliding sporozoites were observed under 25x objective (water, NA 0.8). Movies were recorded in differential interference contrast (DIC) for 5 minutes with 3 Hz at room temperature. Image analysis was done with FIJI (Schindelin et al., 2012) and the plugin "Manual tracking".

Alternatively, sporozoite of the *tlp*-GFP parasite line were imaged using a spinning disc confocal microscope (Nikon Ti series) with 60-fold magnification (NA 1.49).

2.9.3 Flow experiments

Sporozoites were placed in an uncoated flow chamber, allowed to adhere for 10 min and imaged at room temperature. The flow movies were always performed at the same position relative to the flow in order to exclude symmetric variations between the experiments. The acquisition rate was 1 Hz and images were collected with a 10x Apoplan objective (air, NA 0.25) in air. After 100 s, 2 ml of medium were added to one of the reservoirs to induce a flow and the same number of pictures was recorded during flow. Image analysis was done in FIJI by counting the circles sporozoites achieved during 100 s before flow and 100 s after flow.
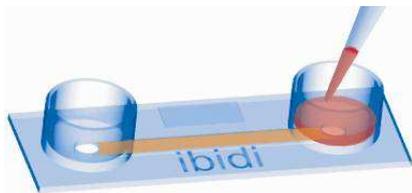

Figure 14: Experimental design of flow experiments: The sporozoite solution was loaded into the flow chamber and allowed to settle. After 10 min incubation, circling parasites were imaged with 1 fps for 100 s before flow was induced with 2 ml (reservoir on the right). Movies were recorded for another 100 s seconds under flow conditions.

2.10 Statistics, Tools and Software

2.10.1 Bioinformatic analysis

Plasmodium berghei sequences were retrieved from the PlasmoDB database (http://plasmodb.org/plasmo/, version 26 to 31). Potential signal peptides and transmembrane domains were predicted using TMHMM (http://www.cbs.dtu.dk/services/TMHMM-2.0/) and other known domains were predicted using SMART (http://smart.emblheidelberg.de/).

2.10.2 Data analysis and statistics

Statistical analysis was performed with the program GraphPad Prism 5.0. Normality of datasets was tested with a Kolmogorov-Smirnov test/ D'Agostino-Pearson normality test/

Shapiro-Wilk-Test. For normal distribution, significance was tested with a One-way ANOVA test or a paired t test (two datasets). If data was not normally distributed, significance was tested with a Kruskal-Wallis test (more than two datasets) or a Mann-Whitney test (two datasets). Optical tweezers movies were processed with FIJI (Schindelin et al., 2012) and analyzed with MATLAB. Statistical analyses for the force experiments were done using Fisher's exact test. Numbers of sporozoites pulling beads out of the trap were first determined for every experimental day and subsequently averaged over all days. Determining the total percentages (*i.e.*, combining the numbers from of all days of observed events) led to almost the same result. This showed that we can directly use the total percentage for force evaluation

3 Results

How the molecular motor of *Plasmodium* sporozoites is organized to enable efficient forward movement is currently not well understood. It is clearly a complex interplay of multiple proteins inside and outside of the sporozoite. A previous study reported for the first time events that happen on the outside of the sporozoite. Munter *et al.* observed that immature sporozoites isolated from the hemolymph transported a small piece of cell debris back and forth along the membrane. The movement of the particle stopped immediately upon addition of 2 μM CytoD (Munter et al., 2009). This observation led to the idea of using optical tweezers with trapped polystyrene beads as handles to investigate sporozoites. In this work, I focus on measuring the forces and the speed of retrograde flow during continuous gliding of the *Plasmodium* sporozoite.

3.1 Optical tweezer experiments

The following optical tweezer experiments were performed together with Dr. Martin Streichfuss in collaboration with the Department of Prof. Joachim Spatz at the Institute of Physical Chemistry at the University of Heidelberg. Prior experiments with the same instrument were published in Hegge *et al.,* 2012, where sporozoites were directly trapped in the focus of the laser beam. In addition to wild type, also transgenic sporozoites lacking a TRAP-family protein as well as sporozoites treated with actin-modulating drugs were examined to analyze adhesion formation.

In our approach, sporozoites were allowed to adhere to the glass bottom of the flow cell (see section 2.4.2). After incubation, the medium (RPMI/ 3 % BSA) was exchanged for a bead solution. Beads were captured from the solution with the laser trap and positioned onto the front end of the gliding sporozoite, which moved on the glass support in characteristic counter clock-wise circles. At low laser intensities, sporozoites pulled the bead out of the focus of the trap immediately after contact and transported it towards the end of the cell. The sequence of a typical experiment is visualized in Figure 15: an optically trapped bead is moved towards the sporozoite (I+II) and positioned onto the front end (III). The sporozoite pulls the bead out of the trap center as soon as both are in contact (IV) and transports the bead to the rear of the cell (V). We believe that this transport represents retrograde flow, an actin-myosin driven process that has already been observed in higher eukaryotic cells. The transport of beads on

the parasite surface reflects indirectly the movement of actin filaments and coupled surface proteins. The adhesins facing the substrate provide handholds for the flowing actin creating the traction needed to push the cell forward.
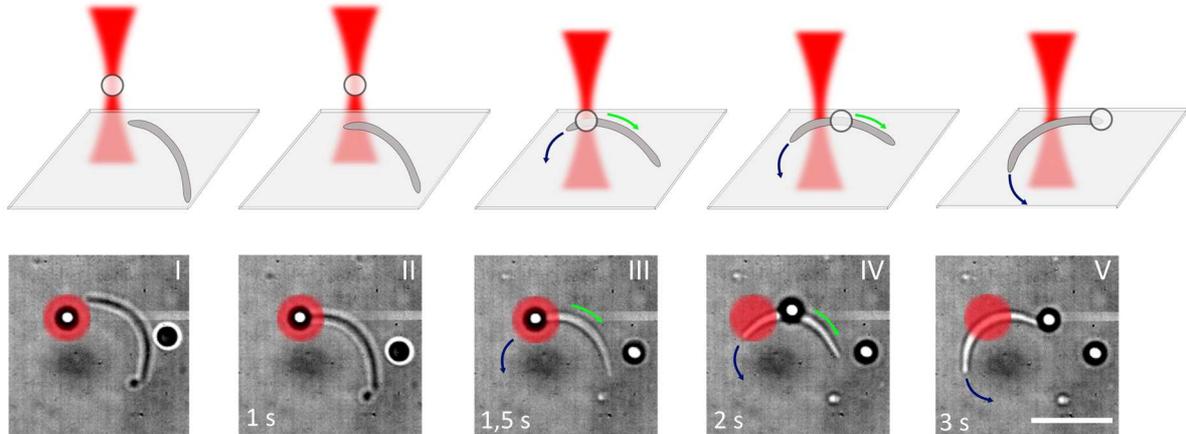

Figure 15: Image series of an optically trapped bead moved towards a circling sporozoite. The top panel is a schematic of the side view of the experiments, while the lower panel shows the field of view at the microscope. The red halo indicates the position of the trap that surrounds the captured bead (black circle with white center). (I) The captured bead is in focus (white center) while the sporozoite is circling below (gray, not in focus). (II) The captured bead is positioned over the front end of the moving sporozoite. (III) The bead is lowered down in z-direction on top of the sporozoite until contact is established. Sporozoite and bead are both in focus (both appear white). Blue arrow indicates the forward movement of the sporozoite. Green arrow shows the transport direction of the bead. (IV) The sporozoite pulls the bead from the center of the laser beam and transports the bead to the end of the cell. At the same time, the sporozoite continues to glide forward on a circular trajectory. (V) The sporozoite moves further, while the bead reaches the rear end of the cell. Scale bar: 10 µm.

First, we tested whether size or functionalization of the beads mattered for transport of the beads (Figure 16). We found that the difference in retrograde transport speed between plain and streptavidin-coated 1 µm beads was statistically significant (p = 0.003). However, there was no difference between 1 µm, 2 µm and 3 µm streptavidin-coated beads. This suggests, that the contact area between sporozoite and bead does not influence the ability of the sporozoite to move the bead at a certain speed. Thus, 2 µm streptavidin-coated polystyrene beads were used for the remainder of this study.
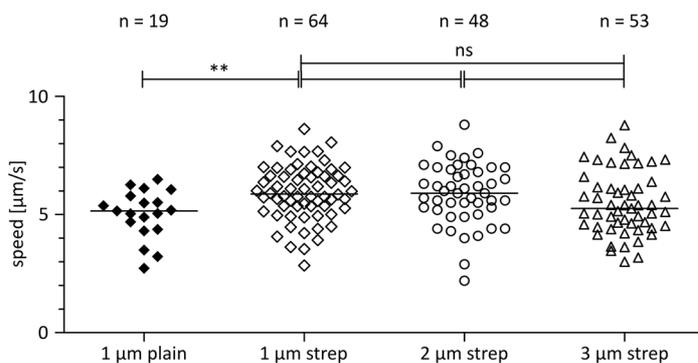

Figure 16: Bead size and functionalization. Transports speeds of beads with different sizes and functionalization. Comparison of plain 1 µm (black diamonds) beads with streptavidin-coated beads (white diamonds) shows statistically significance (t-test, p-value 0,003), but no significant difference between the different bead sizes

3.1.1 Retrograde flow in *Plasmodium* sporozoites

The transport events described in Figure 15 were recorded with a high-speed camera allowing us to measure the speed of the retrograde flow on the back of the sporozoite. The trajectory of the bead followed the outline of the crescent-shape of the sporozoite and is shown in Figure 17 A. All speed curves started with a steep slope corresponding to the acceleration of the bead until a plateau of 5-7 µm/s was reached (Figure 17 B). When the bead arrived at the end of the cell, the speed decreased again. Then, the beads either dissociated from the sporozoites or stayed attached to the end of the cell.
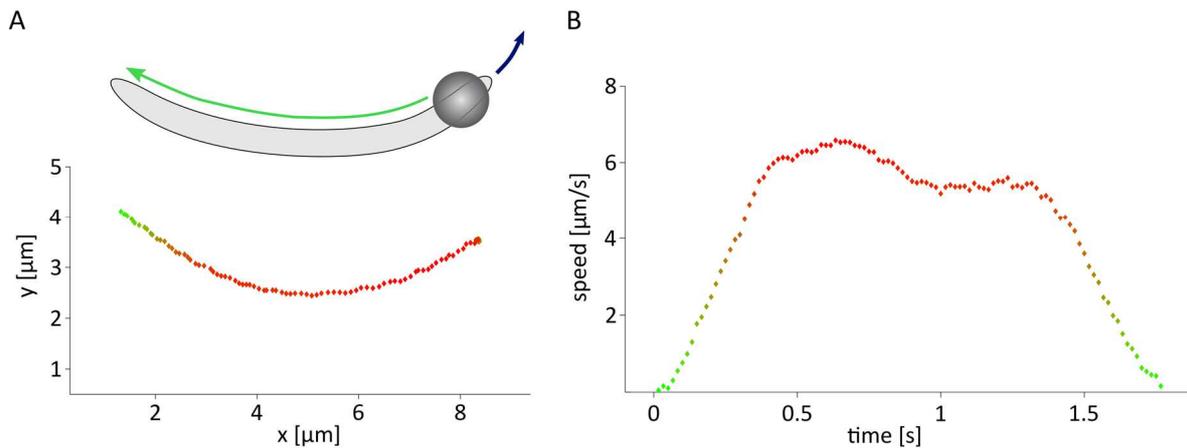

Figure 17: Tracked bead movement along the sporozoite. (A) Exemplary trajectory of tracked bead positions during one recorded transport event. Top: Schematic of counter clockwise moving sporozoite illustrating the corresponding transport event. The bead was positioned on the front end of the sporozoite and transported to the posterior end (green arrow) opposite to the gliding direction (dark blue arrow). Colour code of trajectory: fast speed is shown as red dots and slow speed *i.e.* start of movement (acceleration, not visible in A) and deceleration in green. (B) Corresponding speed curve of transported bead. Peak speed of the plateau: 6 µm/s.

The bead movement described in Figure 17 represents a typical speed curve, that was observed for over 50 % of the cases (Figure 18), where the bead was transported in one movement without interruptions. Alternatively, bead transport also occurred in a step-wise
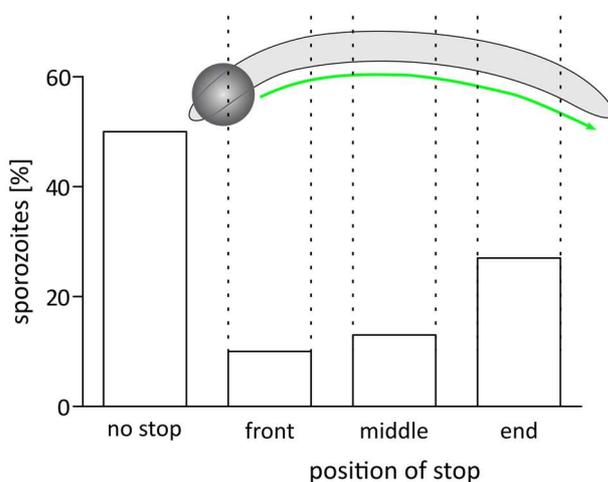

Figure 18: Bead stop events along the length of the sporozoite. The majority of beads got transported in one go, while the other half of transport events occurred with stops at different positions (front, middle or end). On occasion, sporozoites transported with multiple stops (not included). This analysis covered 219 sporozoites.

fashion. Only 10 -13 % of the transported beads stopped in the font or middle section of the sporozoite, while approximately 25 % of the beads stopped at the end before being translocated to the very rear of the cell (Figure 18).

3.1.2 Force measurements

In addition to calculating the speed of the retrograde flow in sporozoites, we employed the optical tweezers set up to measure the forces acting on the beads when in contact with the gliding sporozoite. Figure 19 illustrates how sporozoites tried to pull the bead from a stiffer trap generated by higher laser powers. After depositing the bead onto the sporozoite (I) the bead was displaced from the trap (II), but was still in the force field of the laser trap. Here, the sporozoite did not manage to overcome the optical force and the bead was drawn back to the center of the trap (III). The sporozoite needed two more attempts to successfully pull the bead out of the trap center and transport it to the rear of the cell (IV).
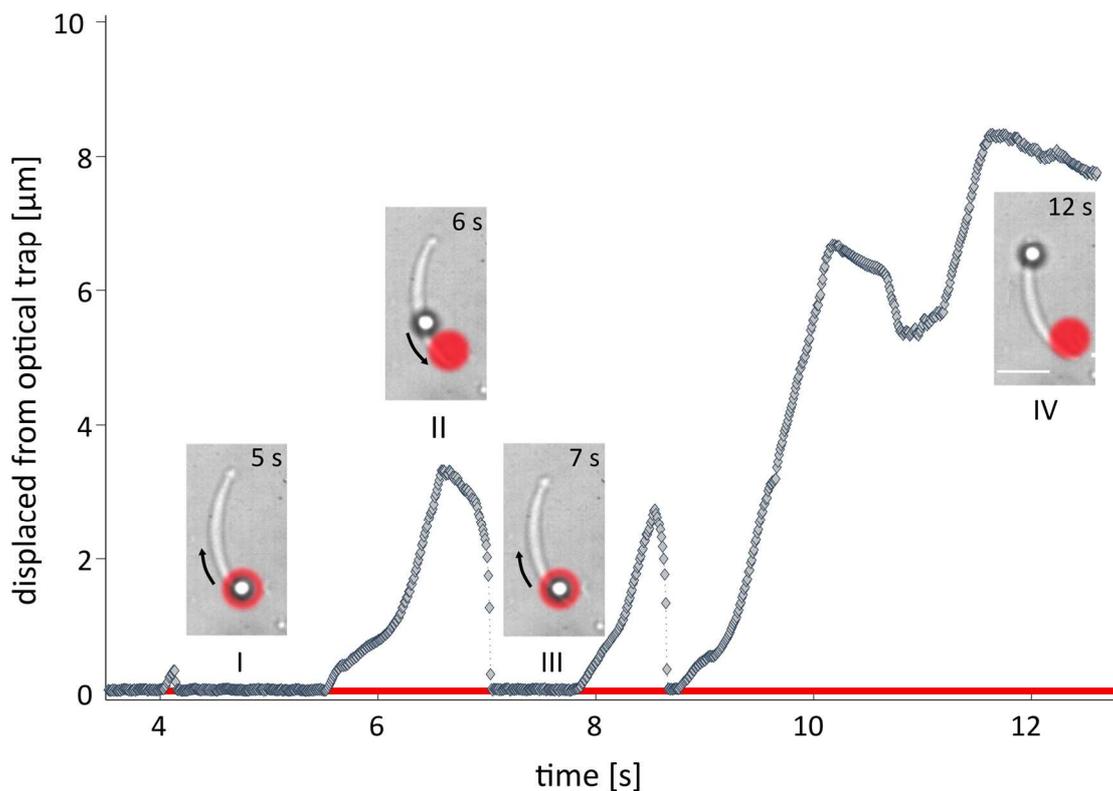

Figure 19: Bead displacement events at a higher force. Trajectory (blue) represents tracked bead positions as the sporozoite tried to pull the bead out of the trap over time. The red horizontal line indicates the static center of the trap. Initial phase (I) and microscopy image show bead and sporozoite in contact. Then, the sporozoite displaced the bead from the trap center (II), but the bead snapped back into the focus of the trap (III). Eventually, the sporozoite managed to pull the bead out of the trap and translocated it to the end of the cell (IV). Black arrows indicate bead displacement from the trap and movement back in. Scale bar: 5 µm.

3.1.2.1 Calibration

In order to determine forces quantitatively with the optical tweezers, the strength of the trap needed to be calibrated. The calibration was performed in two different ways (described in detail in Methods and Materials 2.4.1). The measurements led to a linear slope of the escape
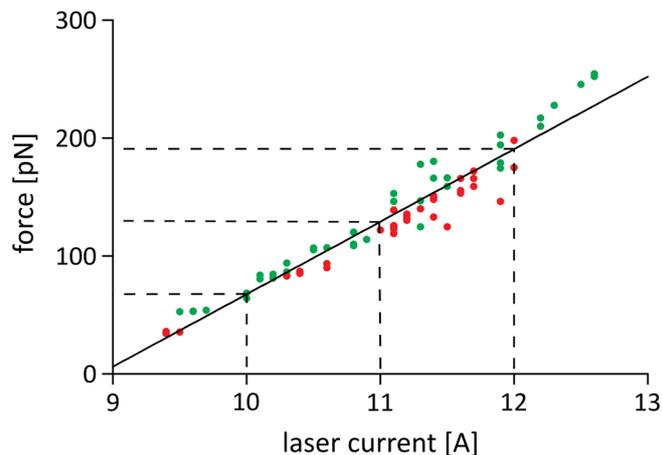

Figure 20: Stokes calibration of optical tweezers. Linear correlation between laser current [A] and force [pN] obtained from two different calibration approaches in a flow cell under constant flow rates: 1st approach (red): a single particle was trapped at high diode current, which was then gradually lowered until bead was displaced by the flow. 2nd approach (green): a higher bead concentration was used and the diode current varied until bead was only briefly trapped in the trap center.

force versus laser power (Figure 20). According to this calibration curve, the diode currents of 10, 11 and 12 Ampere corresponded to escape forces of 70, 130 and 190 pN respectively, while a laser power of 9 Ampere corresponded to less than 10 pN. We then challenged sporozoites to overcome these forces.

3.1.2.2 Force experiments of *Plasmodium* sporozoites

In this first part of the study, we investigated two parasites strains: *Plasmodium berghei* (strain NK65) sporozoites expressing a cytoplasmic green fluorescent protein (GFP) under the stage-specific circumsporozoite protein promoter (Natarajan et al., 2001) resulting in very strong fluorescence at the sporozoite stage. This parasite line served as wild type control in the following experiments. The second type of *Plasmodium berghei* sporozoites we analyzed, lacked the TRAP-like protein (*tlp(-)*, ANKA strain*)* and expressed GFP under the control of the ef1α-promotor (Hellmann et al., 2011; Hellmann et al., 2013) yielding cytoplasmic fluorescence throughout all stages of the life cycle. First, we tested wild type sporozoites for their capacity to overcome forces of 70 pN, 130 pN and 190 pN. As expected, the number of sporozoites managing to overcome the optical force decreased with increasing optical counter force.

The fractions of sporozoites, that managed to displace the bead out of the trap are shown in Figure 21. At 70 pN, 74 % of wild type sporozoite successfully pulled the bead out of the laser trap. At 130 pN, the percentage of wild type sporozoites, that exerted enough force to pull the bead from the trap center was reduced to 40%. At the highest optical counterforce of 190 pN only 20% of wild type sporozoite could overcome this force.
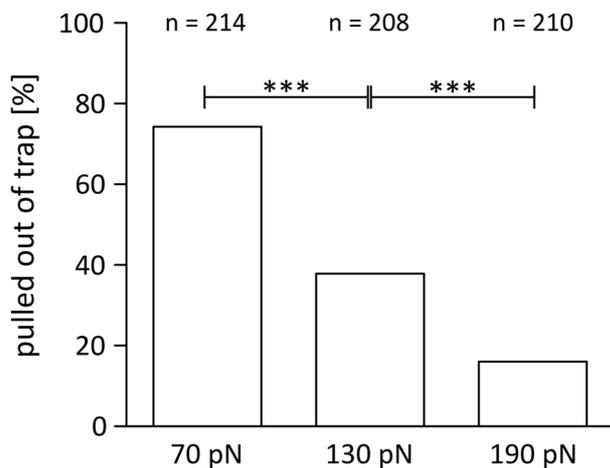

Figure 21: Wild type sporozoites can overcome forces of up to 190 pN. For each force, more than 200 sporozoites were measured over seven separate days from different mosquito cages. Bars represent the percentages of sporozoites that managed to pull the bead out of the trap at the respective forces. Significance was tested with Fisher's exact text.

3.1.3 Actin-modulating drugs affect force and retrograde flow in sporozoites

To test how actin dynamics are involved in the speed of retrograde flow and force production, the effects of actin-modulating drugs on wild type sporozoites were investigated. cytochalasin D (CytoD) inhibits actin filament growth presumably leading to short filaments while jasplakinolide (Jas) stabilizes filaments by blocking filament disassembly. Both drugs were administered at low concentrations (50 nM and 200 nM).

The average retrograde flow speed of wild type sporozoites was 5-7 µm/s (Figure 22 A). In the presence of 50 nM CytoD, the speed of retrograde flow did not change, but decreased significantly under 200 nM CytoD. After addition of 50 nM Jas, retrograde speed was almost twice as high compared to the flow of wild type sporozoites.

In the force experiments, low concentrations of the actin-modulating drugs reduced the ability of wild type sporozoites to pull beads out of the trap significantly at all three forces (Figure 22 B). The effect of 50 nM Jas at 70 pN seemed more pronounced than for CytoD. Wild type sporozoites treated with 200 nM CytoD were already severely weakened at 70 pN, therefore no further experiments were conducted at 130 pN or 190 pN.
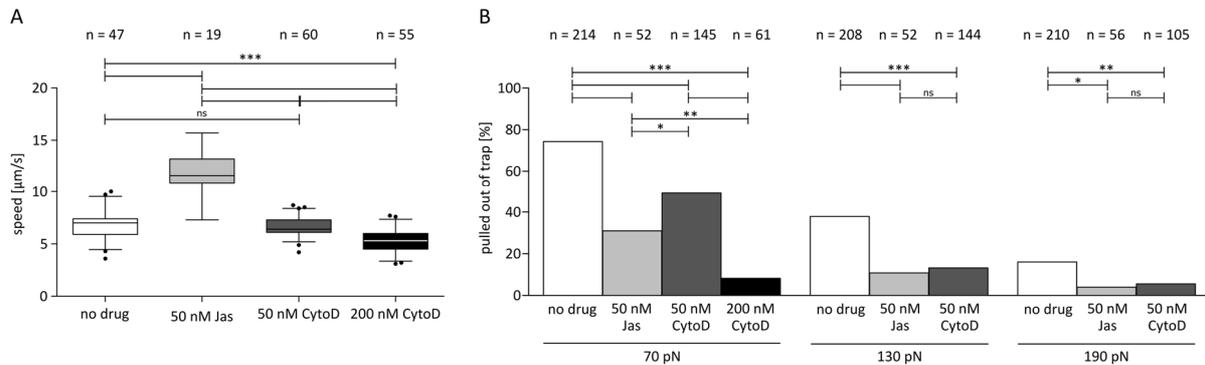

Figure 22: Actin-modulating drugs affect force and retrograde flow in sporozoites. (A) Retrograde flow speeds were assessed for wild type sporozoites (CSGFP, white) in the absence or presence of CytoD (dark gray) and Jas (light gray) at indicated concentrations. Number of sporozoites measured for each group are displayed above the respective boxes. Statistical test: One-way ANOVA. Boxplots: the boxes contain 50% of data and whiskers indicate 5 – 95 %. The horizontal bar shows the median. (B) Force plot of wild type sporozoites probed at 70 pN, 130 pN and 190 pN in the absence or presence of actin modulating drugs. Note that for wild type sporozoites treated with 200 nM CytoD, experiments were only conducted at 70 pN. n = number of sporozoites probed. Significances were tested with Fisher's exact text.

3.1.4 Force and retrograde flow in *tlp(-)* sporozoites

Sporozoites lacking the surface protein TLP glide normally, invade into and replicate in the liver, albeit at a slightly reduced rate if injected directly into the blood (Heiss et al., 2008; Moreira et al., 2008). However, during natural transmission through a bite of an infected mosquitoes, the parasite load in the liver was 10-fold decreased (Moreira et al., 2008). Adhesion strength and attachment were already investigated in flow assays (Hegge et al., 2010). Here, induced flow compensated for the absence of TLP on the parasites surface and sporozoites moved more continuously and similarly to wild type sporozoites before flow.

To further investigate the function of TLP in force transmission, tlp knock out (*tlp(-),* (Hellmann et al., 2011) sporozoites were tested in the above-described tweezer assays. The speed of transported beads on *tlp(-)* sporozoites was much faster than in wild type sporozoites (Figure 23 A). The speed median as wells as the speed peaks were up to twice as high, the latter reaching values between 12 and 15 µm/s. The average speed of the retrograde flow in wild type sporozoites treated with 50 nM Jas (Figure 23 A) was similar to *tlp(−)* sporozoites without

any drug treatment. Low concentration of Jas or CytoD did not strongly affect the transport speed of *tlp(−)* sporozoites, while 200 nM of CytoD slowed down the retrograde flow significantly (Figure 23A).

We also investigated the force *tlp(-)* sporozoites could overcome (Figure 23 B). Compared to wild type sporozoites, only 20 % of the sporozoites lacking TLP managed to pull the bead out at 70 pN. Since this number was reduced even further at 130 pN, we did not test the knock-
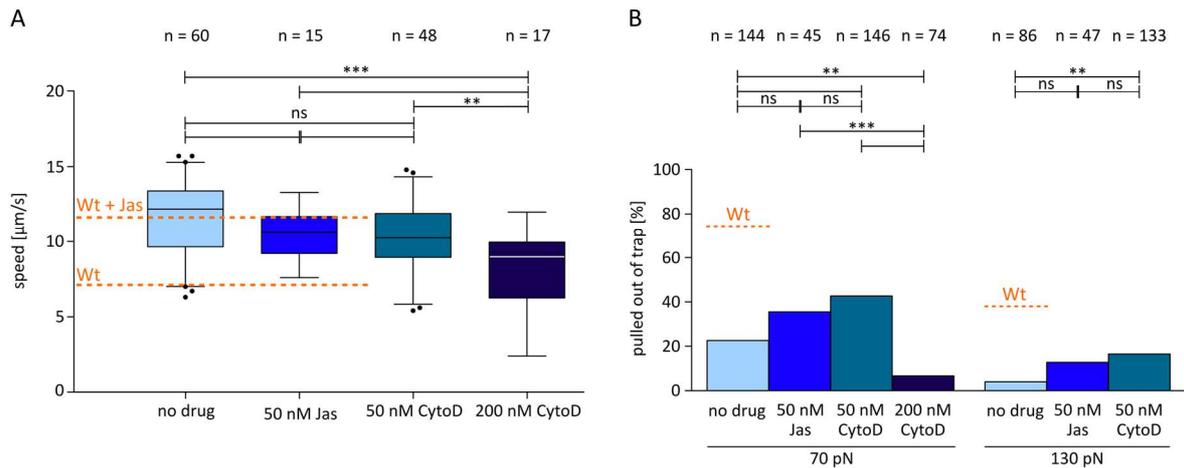

Figure 23: Optical tweezer analysis of *tlp(-)* sporozoites with and without drug treatment. (A) Retrograde flow speeds were assessed for *tlp(-)* sporozoites (light blue) in the absence or presence of CytoD (dark blue) and Jas (blue) at indicated concentrations. Number of sporozoites measured for each group are displayed above the respective boxes. Bottom orange dashed line represents the average flow speed of wild type sporozoites and the top orange dashed line indicates the speed of wild type sporozoites with 50 nM Jas. Statistical test: One-way ANOVA. Boxplots: the boxes contain 50% of data and whiskers indicate 5 – 95 %. The horizontal bar shows the median. (B) Force plot of *tlp(-)* sporozoites probed at 70 pN and 130 pN in the absence or presence of actin modulating drugs. Orange dashed lines represent the corresponding percentages of wild type sporozoites. Note: Since the percentage of *tlp(−)* sporozoites was already low at 130 pN, no further experiments were conducted at higher forces. n = number of sporozoites probed. Significances were tested with Fisher's exact text.

out sporozoites with 190 pN. After addition of Jas and CytoD at low concentration, more sporozoites displaced the bead at both tested forces, but the effect was only significant for 50 nM of CytoD (Figure 23 B) It seemed, that the drug could partially compensate for the defect occurring in the *tlp (-)* sporozoites. However, addition of high concentration of CytoD, reduced the force production again.

3.1.5 Treatment of sporozoites with CytoD delays bead transport

Not only retrograde flow and force were impaired under actin-modulating conditions, but also the initial contact phase between bead and sporozoite could be affected. During assessment of sporozoites treated with 200 nM CytoD, we realized that transport initiation was significantly delayed. Thus, we re-analyzed the retrograde flow data and determined the time until sporozoites transported the bead after contact. Beads were transported almost immediately after being positioned onto the sporozoite surface on both wild type and *tlp(−)* sporozoites (Figure 24). Jas had no effect on wild type or *tlp(−)* sporozoites regarding time until transport. However, after incubation with increasing concentrations of CytoD, sporozoites of both parasites lines took significantly longer to initiate retrograde flow of the bead.
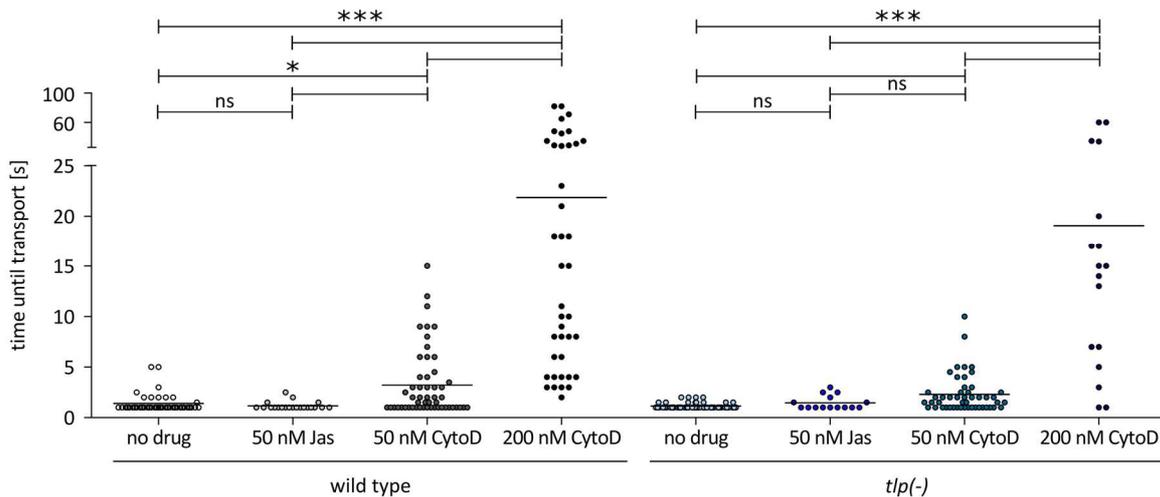

Figure 24: Time until bead transport initiation after contact between bead and wild type or *tlp(−)* sporozoites in the absence or presence of actin modulating compounds. Horizontal bars indicate median. Significance: Kruskal-Wallis Test

3.2 Generation of parasite lines

3.2.1 Receiver lines

In order to dissect the localization and the functional regions of TLP in more detail, an intramolecular GFP tag and two additional mutants of the *tlp* gene carrying modified C-termini and a wild type reconstitution to restore the phenotype, were generated (Figure 25).
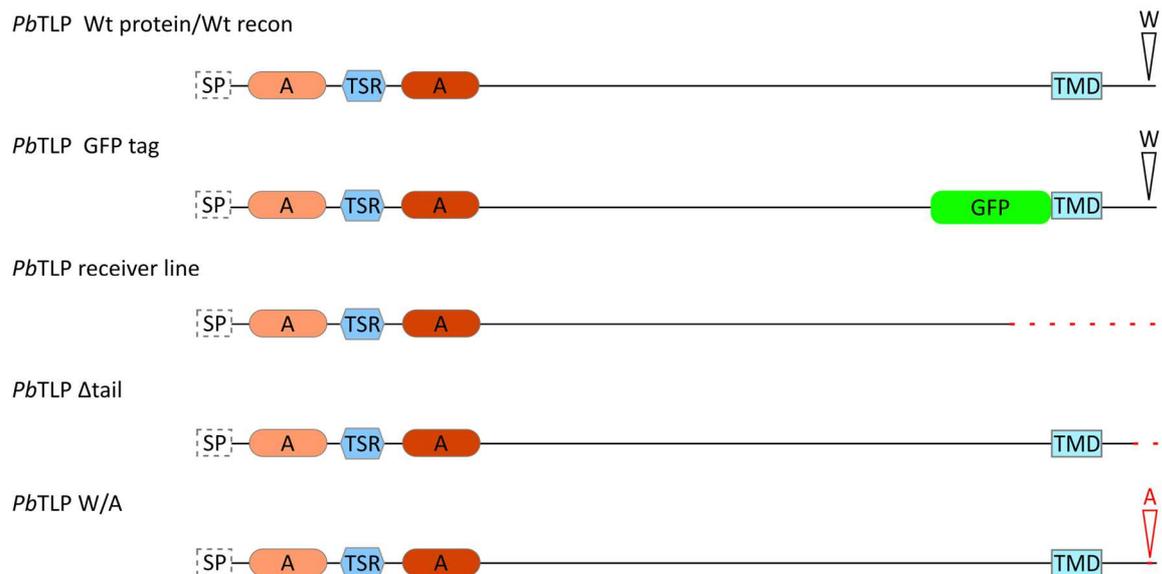

Figure 25: Overview of *Pb*TLP wild type, generated GFP tag and truncated proteins. The receiver line lacks the C-terminus including the transmembrane domain indicated by the red dashed line. The GFP tag is localized in front of the transmembrane domain. The TLP tail deletion is missing 14 amino acids, while in the last TLP tail mutant the penultimate tryptophan is substituted with an alanine.

For easier and faster transfections, we first created two receiver lines: One based on a parasite line expressing GFP under the ef1α-promotor and mCherry (red fluorescent protein) under the stage-specific circumsporozoite protein promoter (referred to as red-green line "RG", Dennis Klug) and another one based on the non-fluorescent *Pb*ANKA background. The latter was used to introduce a GFP tag in front of the transmembrane of the *tlp* gene.

To generate the receiver lines, we used the *Pb*262 vector (Dennis Klug) and modified it by introducing homology regions of *tlp* (Figure 26 A). This vector was transfected into the two respective background parasite lines to achieve homologous recombination at the *tlp* locus.

The results of the genotyping PCR are shown in Figure 26 B. The respective DNA was integrated correctly, resulting in bands with the expected fragment sizes.
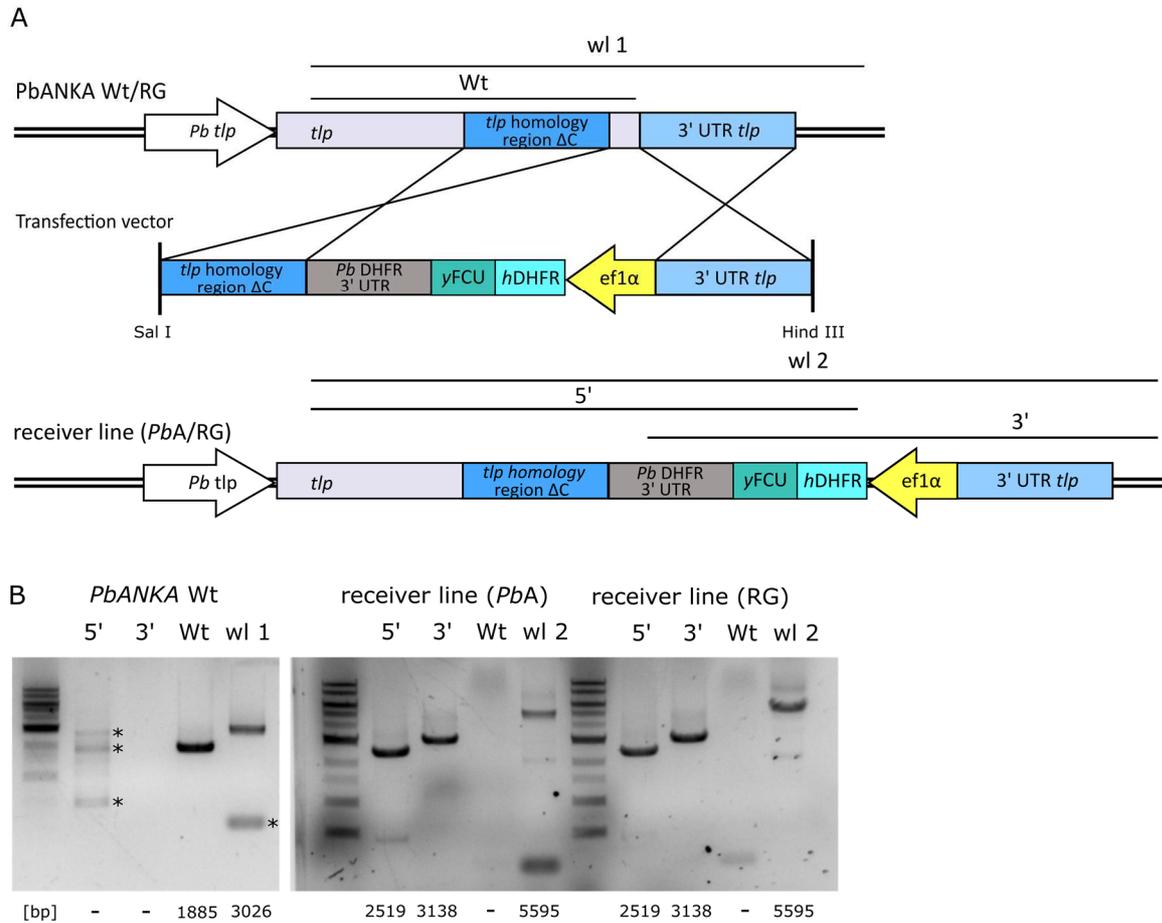
Figure 26: (A) Generation of receiver lines. Homologous recombination of the *tlp* homology region containing a truncated C-terminus (ΔC) and the 3' UTR of *tlp* (both blue). After integration, the receiver lines contained a *y*FCU-*h*DHFR fusion protein (turquoise) allowing for positive and negative selection. (B) Left panel shows exemplary wild type control (*Pb*ANKA): expected products (amplicon size indicated below the lanes) for the Wt control and for the whole locus were amplified. Right panel displays both receiver lines: successful 5' and 3' integration, missing band for wild type *tlp* and longer fragment for the whole locus. Unspecific bands are marked with asterisks (*). Marker: 1kb DNA ladder.

3.2.2 Localization of TLP

In the second step, a GFP-tag was transfected into the non-fluorescent receiver line (rl *Pb*A, Figure 27). Using the gene-in-marker-out (GIMO) strategy (Lin et al., 2011), the GFP was introduced into the *tlp* locus thereby also reconstituting the C-terminus that had been missing in the receiver line.

The GFP-tag was introduced in front of the transmembrane domain, resulting in an extracellular location (Figure 27 C). Successful integration of the GFP-tag was confirmed by PCR (Figure 27 B).
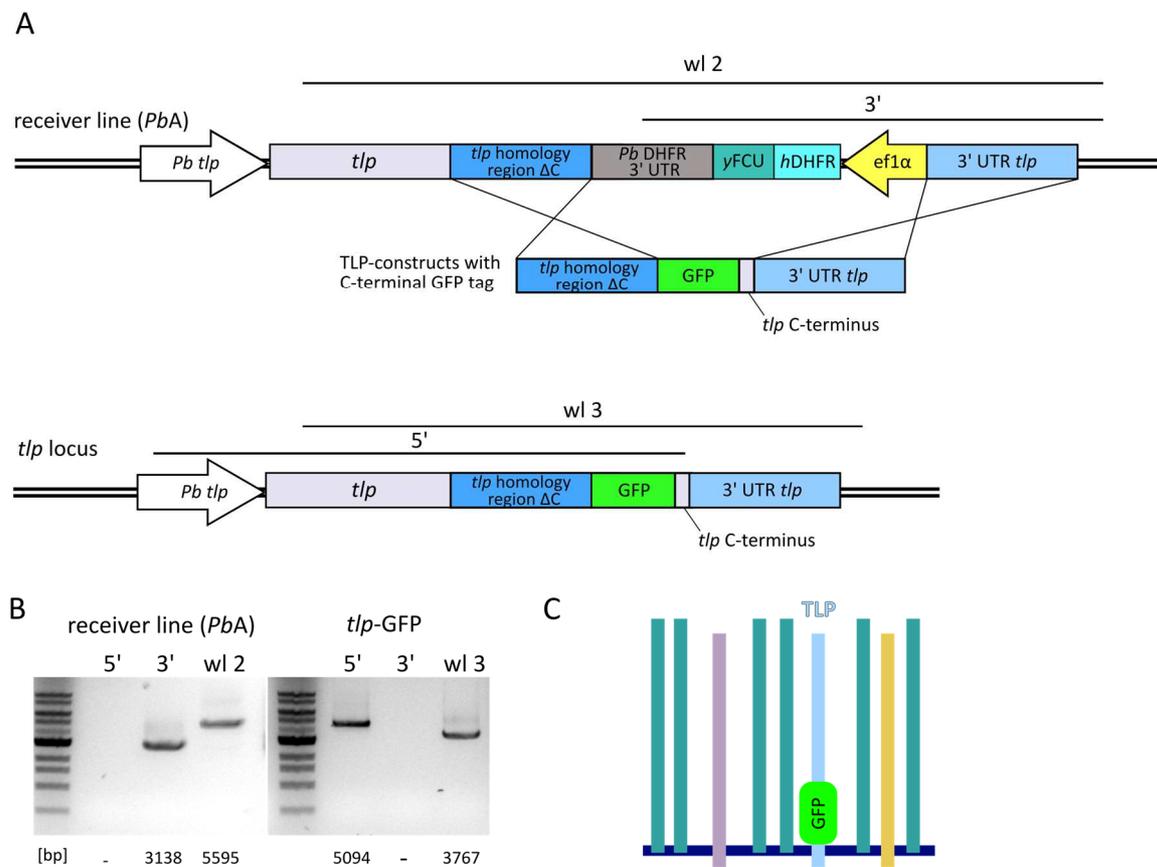
Figure 27: (A) Transfection of GFP tag into non-fluorescent receiver line (rl *Pb*A). Homologous recombination was achieved via the *tlp* homology region and 3' UTR of *tlp*. Note that the resulting parasite line contains no more vector-DNA. (B) Left panel shows integration bands of the receiver line (*Pb*A) that amplified the selection marker cassette (3') and shows a longer whole locus band (wl2). The right panel displays successful integration of the GFP-tag (5') and lacks the selection marker (no 3' and shorter whole locus 3). Marker: 1kb DNA. Expected amplicon sizes are shown below the lanes. (C) Schematic localization of the GFP-tag within TLP with respect to the plasma membrane. TLP topography shown with a single transmembrane domain.

Salivary gland sporozoites (day 17 post infection) of the *tlp*-GFP parasite line displayed heterogenous localization of TLP (Figure 28). The fluorescence appeared distributed along the cells in various intervals with different intensities. Figure 28 shows sporozoites performing collective motion. This phenomenon termed whirls or vortices formation was described by Konrad Beyer in detail, where 5-100 closely packed sporozoites move together in circles. These structures form after sporozoites get activated within the salivary glands and migrate at their periphery between basal membrane and acinar cells (Beyer, 2017).
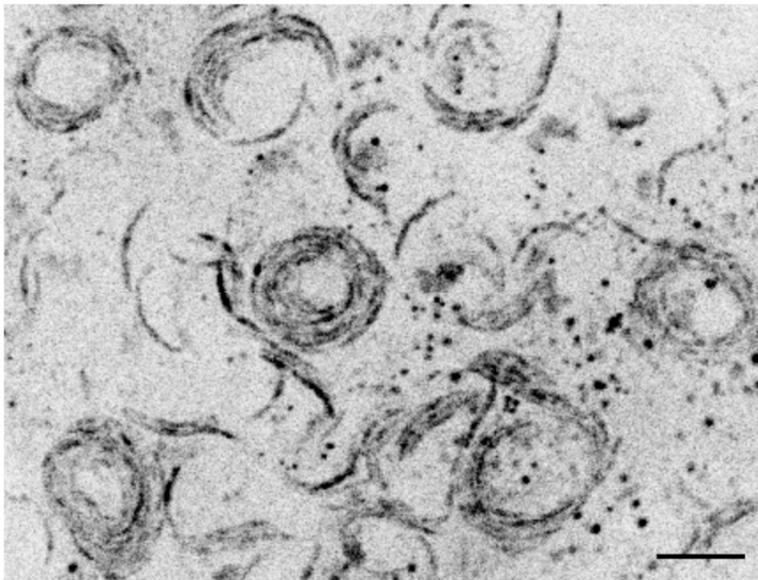
Figure 28: Live *tlp*-GFP sporozoites forming vortices after being activated within the salivary gland. Sporozoites displayed diverse GFP-signal patterns. Scale bar:10 µm

In addition, I performed immunofluorescence on *tlp*-GFP sporozoites by detecting fluorescence derived from the GFP-tag and by also staining GFP with antibodies as fluorescence of the GFP-tag was impaired by the fixation (Figure 29). The Hoechst-staining showed the nucleus while sporozoites were outlined in DIC. After permeabilization with Triton, GFP fluorescence was stronger and more distinct. In both staining approaches, GFP localization appeared fragmented and could be consistent with a vesicular distribution. This pattern was also observed in a different parasite line where TLP contained an N-terminal GFP tag (Singer, 2017).

| | DIC | Hoechst | GFP | anti-GFP |

Figure 29: Immunofluorescence staining of *tlp*-GFP salivary gland sporozoites. In addition to detecting the fluorescence of the GFP-tag, the fixed sporozoite samples were incubated with anti-GFP antibody and subsequently with a secondary antibody to vis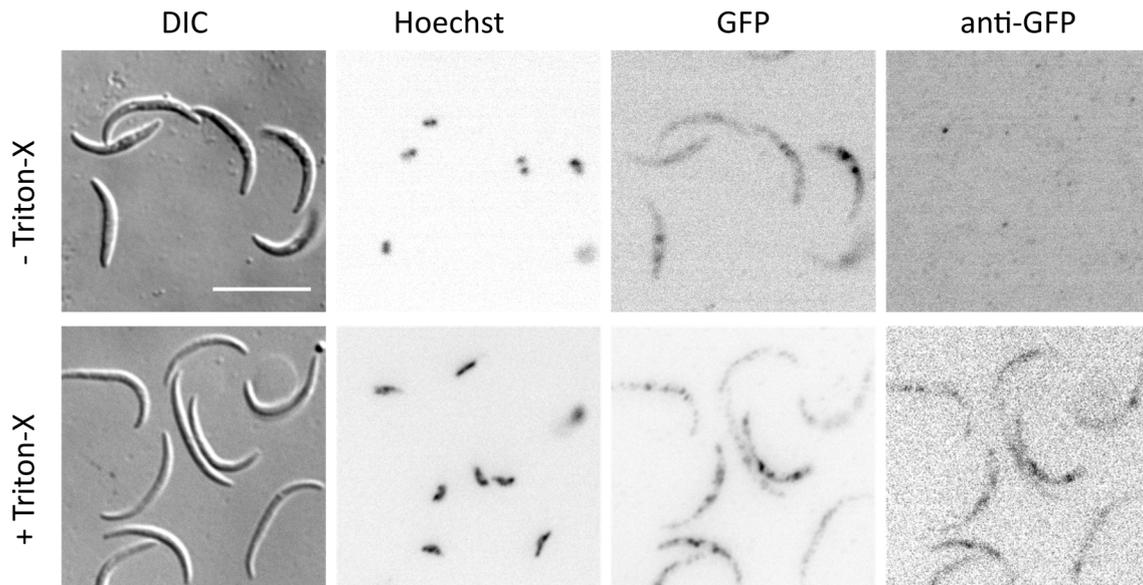ualize GFP. Hoechst stained the nucleus. The lower panel illustrates sporozoites treated with Triton-X to permeabilize the cells. Scale bar: 10 µm.

3.2.3 TLP tail mutants

The fluorescent receiver line (RG) was used to transfect the TLP tail mutants. (Figure 30 A). The wild type reconstitution (Wt recon) was included to restore the incomplete *tlp* wildtype locus of the receiver line and should phenotypically behave like wild type parasites. The first mutant was a tail deletion (Δtail), which is missing 15 amino acids of the C-terminus. In the second mutants, the penultimate tryptophan was substituted with alanine (W/A).

The different constructs carrying the altered versions of the TLP tail regions were transfected into the receiver line (RG) to achieve homologous recombination (Figure 30). Panel B illustrates successful integration of mutant constructs (Wt recon, Δtail or W/A). The absence of 5' amplicons was seen only in the receiver line, the presence of the C-terminus and smaller whole locus fragment showed that the desired mutations had been integrated.
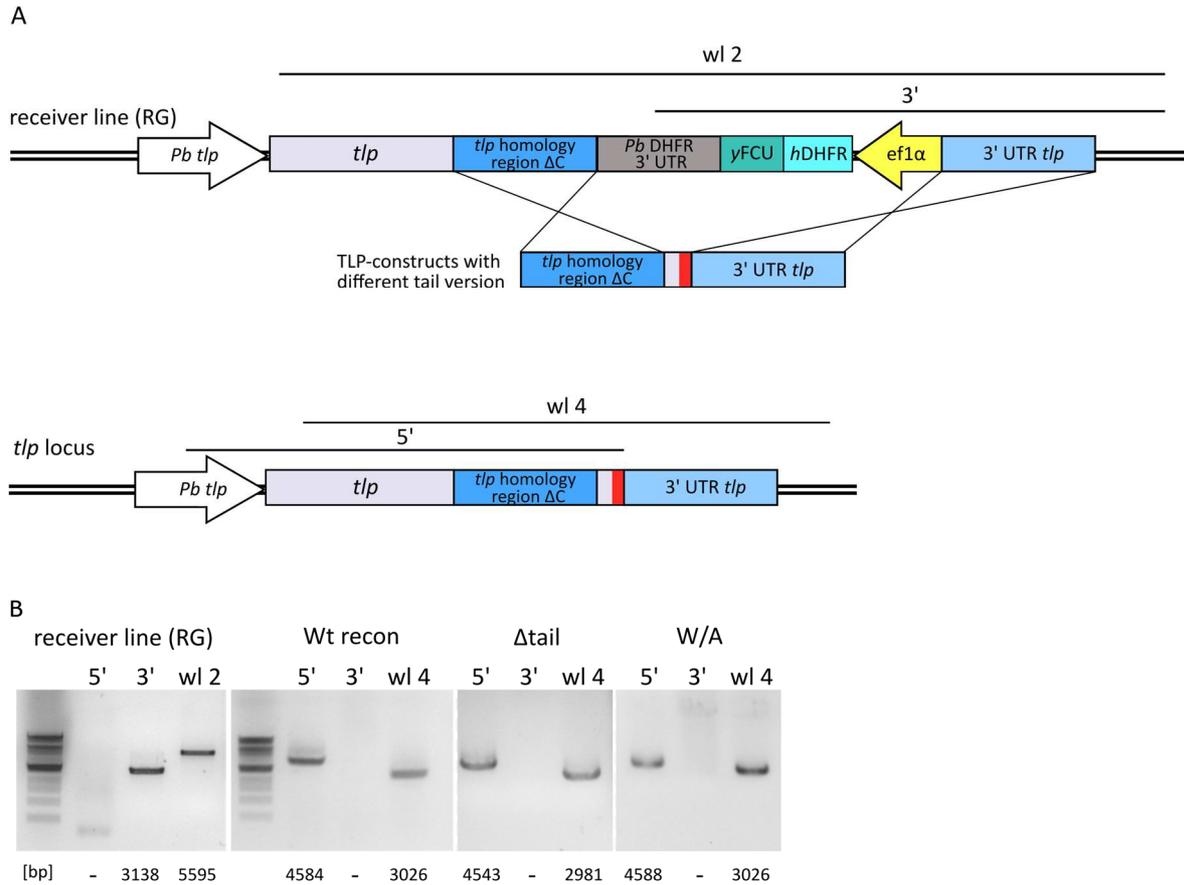
A

B

Figure 30: Generation of transgenic parasite line. (A) Replacement of the C-terminal part of the *tlp* locus in the receiver line with the TLP tail mutants was accomplished through double homologous recombination. The red box indicates the different tail versions. (B) Integration was verified by amplifying the fragments shown as black lines in A. This showed that the Wt recon (2nd panel), the Δtail with a slightly shorter whole locus PCR product (3rd panel) and the amino acid substitution (W/A) were properly integrated. PCR-products of the receiver line (1st panel) were absent in mutant clonal lines. Marker: 1kb DNA ladder. Expected amplicon sizes are indicated below the lanes.

The alignment of the protein sequence in Figure 31 shows the *Pb* TLP wild type proteins with the truncated receiver line and the mutated TLP tail versions.
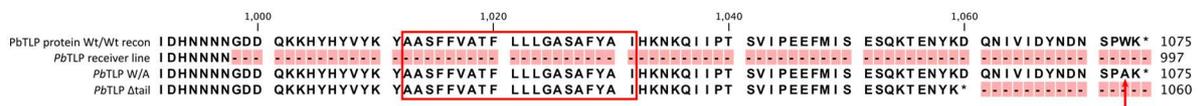
Figure 31: Alignment of *Plasmodium berghei* TLP C-termini. The receiver line (second row) was lacking a part of the tail region including the transmembrane domain (red box, position 1012-1031) compared to the complete TLP (top row). The C-terminus of the receiver line (RG) was replaced with three versions of the TLP tail: The amino acid swap from tryptophan (W) to alanine (A) (indicated by the red arrow), the Δtail lacking 15 amino acids and the Wt recon identical with the original TLP (top row).

69

3.3 Characterization of TLP tail mutants

3.3.1 *In vivo* experiments

A comprehensive expression profile analysis of the parasite transcriptome using quantitative reverse transcriptase PCR (qRT-PCR) was performed by Mirko Singer in the Frischknecht lab. Here, I only show the results for the TRAP-family proteins for the different sporozoite stages in the mosquito normalized to CSP. Samples (cDNA) of purified and unpurified midgut sporozoites (MGS; 12 post infection), hemolymph sporozoites (HLS; day 14 post infection) and salivary gland sporozoites (SGS; day 17 post infection) were prepared. Subsequently the transcription profile of TRAP, TLP and S6 was analyzed in comparison to CSP within the different samples. As expected CSP was highly expressed throughout the sporozoite stages in the mosquito (Figure 32). The level of TRAP stayed stable over time. The mRNA of TLP was almost not detectable in midgut sporozoites, but was highest in salivary gland sporozoites, while S6 expression decreased over time and was lowest in salivary gland sporozoites. The absence of TLP expression at the midgut stage is supported by the lack of fluorescent signal of a TLP parasite line N-terminally tagged with GFP (Mirko Singer, personal communication) as well as the intramolecularly tagged TLP generated in this thesis.
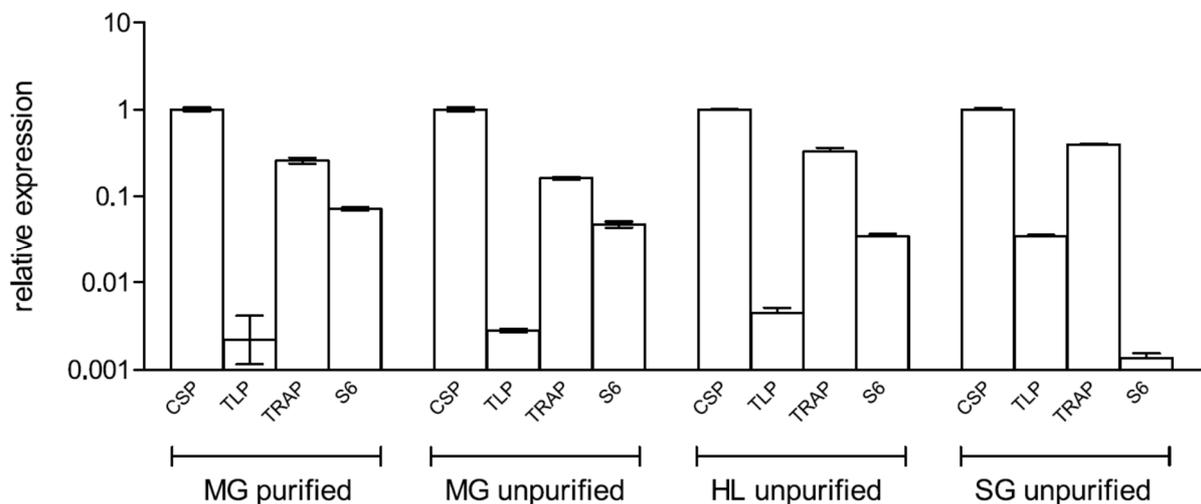
Figure 32: Quantitative RT-PCR on cDNA generated from midgut sporozoites, hemolymph sporozoites and salivary gland sporozoites. Transcription levels of CSP, TRAP, TLP and S6 were determined by using gene specific primers. Error bars: Standard deviation of three technical replicates.

According to the qRT-PCR results, TLP seemed to be dispensable during sporozoite maturation. Therefore, strong effects on midgut, hemolymph and salivary gland sporozoite

numbers were not expected. Quantification of midgut and salivary gland sporozoites (day 17-24) for the mutant lines as well as for the wild type were summarized in Table 1.

Table 1: Absolute numbers in midgut and salivary gland sporozoites. Sporozoites were counted between day 17 and 24 post infection. Data represent 2 to 3 different feeding experiments per line and sporozoite numbers were assessed from at least three different days for each cage. Mosquitoes were pre-selected as all parasite lines were fluorescent.

parasite line	midgut sporozoites	salivary gland sporozoites	MG/SG
wild type (RG)	82,000	18,000	0.21
tlp(-)	95,000	19,000	0.20
receiver line (RG)	48,000	11,000	0.22
Δtail	74,000	13,000	0.17
W/A	60,000	13,000	0.21
Wt recon	92,000	17,000	0.18

The salivary gland to midgut sporozoite ratio of all parasite lines ranged from 0.17 to 0.22 indicating that parasites develop without impairment, egress normally from oocysts and invade salivary gland at normal rates. The differences in absolute numbers are likely due to different infection rates of mosquito cages and normal variations in infection of salivary glands. In addition, wild type and the knock-out parasite have completed the whole life cycle more frequently and might therefore have better adapted to switching between the mammalian host and the mosquito vector.

Additionally, we tested how fast these parasites were able to establish an infection in the mammalian host. Therefore, the prepatent period, the time until the parasites are detectable in the blood was determined. For this, mice were injected with 100 salivary gland sporozoites IV or were infected via natural transmission by allowing 10 infected mosquitoes to bite. Heiss *et al.* reported for the *tlp(-)* half day delay in prepatency after rats received infectious mosquito bites, while Hellmann *et al.* described, that sporozoites lacking TLP (parasites used during this thesis) needed a whole day longer than wild type sporozoites to establish a blood stage infection in C57Bl/6 mice after receiving infectious mosquito bites (Heiss et al., 2008; Hellmann et al., 2011).

In my experiments, after injection of 100 sporozoites IV, wild type parasites were detected after 3,75 days in the blood. The prepatency after by bite experiments was 3,5 days (Table 2). The knock-out and the Δtail parasites were detected in the blood more than one day later than wild type and the other TLP tail mutants after IV injection. This delay was also observed in the bite back experiments for the Δtail (5 days), but at a lesser extend for the *tlp(-)* (4 days).

Results

The receiver line lacking a substantial portion of the TLP tail region including the C-terminal transmembrane domain should in theory mimic the knock out phenotypically and should serve as an internal negative control for the TLP tail mutants. The parasites of the receiver line caused blood infections only with a slight delay after IV injection (4.38 days) and almost a day delay after natural transmission (4.25 days). The mutant parasite lines W/A and the Wt reconstitution had no strong delay compared to the wild type in both *in vivo* assays.

Table 2: Transmission potential of the generated TLP tail parasite lines in comparison to wild type and *tlp(-)*. The prepatency is determined as the time between infection and the first observation of blood stages and is given as the mean of all mice that became blood stage positive. All experiments were performed with C57/BL6 mice. Mosquitoes for bite back experiments were pre-selected.

parasite line	100 Spz IV [day]	parasitemia at day 6 [%]	bite back [day]	Ø sporozoite number of bite back mosquitoes	parasitemia at day 6 [%]
wild type (RG)	3.75 (8/8)	1.27	3.5 (4/4)	12,300	2.23
tlp(-)	4.88 (8/8)	0.31	4.0 (4/4)	8,400	1.70
receiver line (RG)	4.38 (8/8)	0.48	4.25 (4/4)	11,000	0.46
Δtail	4.88 (8/8)	0.25	5.0 (4/4)	5,200	0.08
W/A	4 (8/8)	0.53	3.75 (4/4)	3,400	0.86
Wt recon	4 (8/8)	0.83	3.25 (4/4)	5,600	1.35

Infections with 100 wild type sporozoites (IV) led to the highest parasitemia of 1.27 % while bite back experiments with 5-10 infected mosquitoes led to the maximal parasitemia of 2.23 %. Sporozoites lacking TLP and or lacking the C-terminus (Δtail) showed the lowest parasitemia after IV injection on day 6 (0.31 % and 0.25 % respectively). However, blood stages of the *tlp(-)* line reached an average parasitemia of 1.7 % on day 6 after mosquito bites, while the parasitemia for Δtail was the lowest (0.08 %). Parasites of the amino acids swap (W/A) led to an average parasitemia of 0.53 % after IV injection and 0.86 % after by bite experiments. The parasitemia of the Wt recon resembled wild type percentages (0.83 % IV and 1.35 % by bite). Parasitemia progressions of the above-described parasite lines are shown in Figure 33. After injection of 100 sporozoite IV, the mutant parasite lines grew slow and in a similar way, while the wild type parasites (green) grew faster. The Wt recon (orange), line reached an equally high parasite number in the blood on day 7. In Figure 33 B, after natural transmission though infectious mosquito bites, the *tlp(-)* line (blue) initially grew slowly, but had a steep slope that peaked with the highest parasitemia at day 7. The wild type parasite line (green) and the Wt recon (orange) grew in a similar fashion. The W/A mutant (yellow), Δtail (red) and receiver line (purple) display a comparable course of infection and grew slowly.
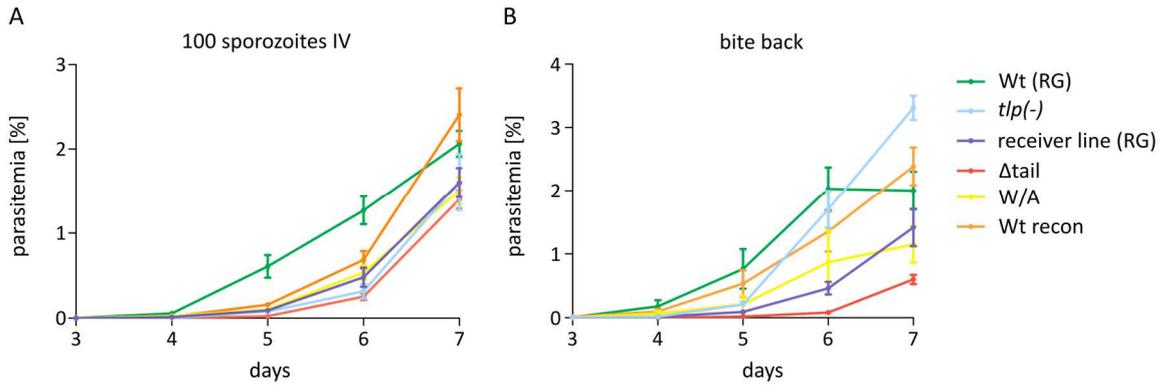
Figure 33: *In vivo* experiments in C57Bl/6 mice. Course of infection followed from the first detection of an erythrocytic-stage parasite in Giemsa-stained blood smears after transmission by infected mosquitoes (A) and after injection of 100 sporozoites IV (B). Mice were sacrificed on day 7 post infection. Error bar: Standard error of the mean from 8 mice in IV injections and 4 mice in bite back experiments.

To facilitate the visualization of the prepatency and parasitemia from table 2, I incorporated both parameters in Figure 34. I grouped the generated parasite lines according to their genotype. The first group consisted of the wild type and the Wt reconstitution (controls), the second group combined the values of the knock-out, the receiver line and the Δtail (deletions), while the W/A point mutation remained separate. As seen for the pre-grouped parasite lines, the data of both *in vivo* assays suggests that the average prepatency of the controls and the W/A parasite line was the same, while the deletions displayed a delay. The parasitemia was highest for the wild type controls, while it was much lower for both the deletions and the single amino acid swap.

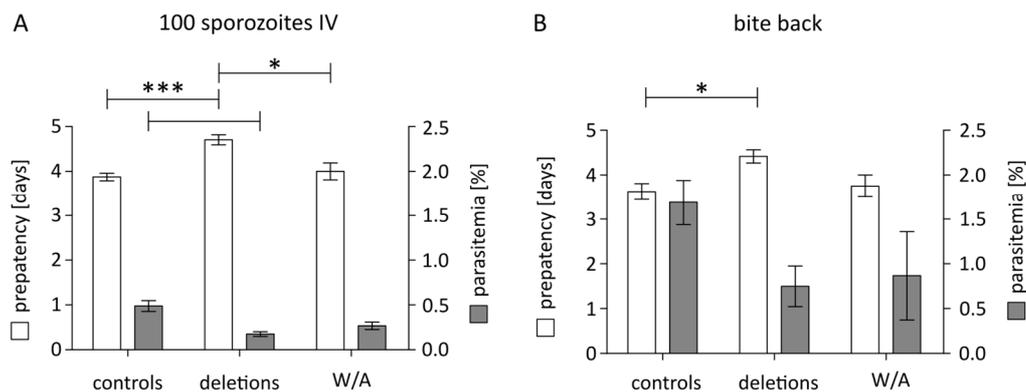Figure 34: *In vivo* data of prepatency (white bars) and parasitemia (black) in groups combining wild type and Wt recon as controls, *tlp(-)*, receiver line and the Δtail as deletions and W/A for the infections with (A) 100 sporozoites IV and (B) after infectious mosquito bites. Statistical test: Kruskal-Wallis. Only significant differences were shown; all other differences were not significant.

3.3.2 *In vitro* experiments

The gliding assays of salivary glands sporozoites were performed to investigate differences in moving patterns *in vitro* hinting towards a possible phenotype *in vivo*. The results are summarized in Figure 35. For each parasite line, approximately 50 sporozoites were analyzed. Sporozoites of all investigated parasite lines moved consistently without any obvious impairment or striking phenotypes. There is a statistical difference between Δtail, wild type, *tlp(-)* and receiver line sporozoites. Yet, speed values are between 1-3 µm/s which is considered in the normal range. This suggests that this assay is either not sensitive enough to spot a possible difference in gliding behavior or these sporozoite have no defect in gliding *in vitro.*
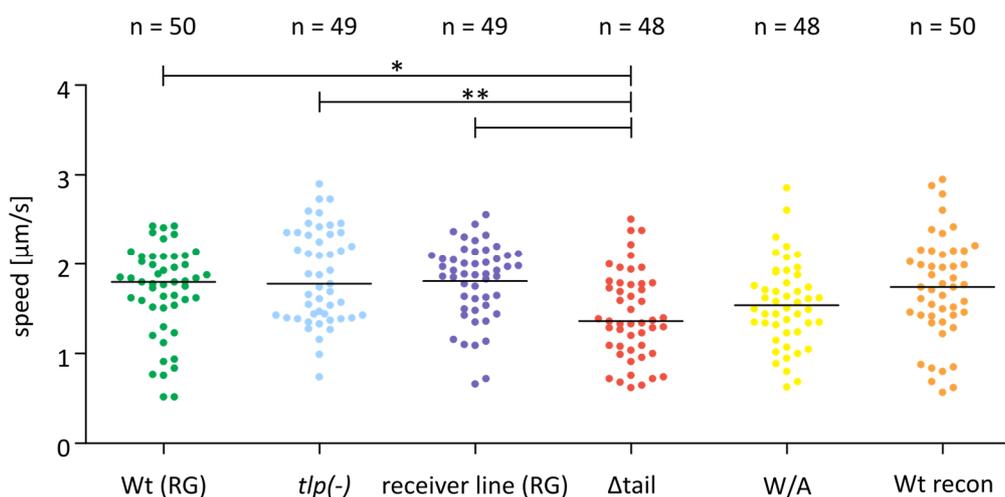
Figure 35: Speeds of sporozoites from mutant parasite lines in comparison with wild type sporozoites moving in 96-well plate with an optical bottom. Gliding sporozoites were imaged for 5 min with 3 Hz and subsequently manually tracked in FIJI (Schindelin et al., 2012). Only the comparison of the Δtail with Wt (RG), *tlp(-)* and the receiver line (RG) was significant, but values lay within the normal range between 1-3 µm/s. All other groups are not significant. Statistical test: not normally distributed, non-parametric test: Kruskal-Wallis-test. Only sporozoites classified as gliding were examined. Bars indicate the median.

In order to tease out the subtle difference in the TLP tail mutants, sporozoites of the respective mutant were tested for their capacity to move under flow. In Hegge *et al.,* 2010, it was described, that wildtype sporozoite slow down under flow conditions, while the gliding speed of *tlp(-)* sporozoites was increased under flow. The stability of gliding sporozoites was evaluated by counting the number of circles described by motile sporozoites during 100 s before and after flow (Figure 36).

In contrast to Hegge *et al.,* 2010, the average number of circles under flow was reduced for all tested parasite lines (Table 3). The difference of circles before and after flow was statistically

significant for all parasite lines except for the receiver line (Figure 36). Also, the ratio before to after flow was lowest for the receiver line (1.20). The next lowest ratios were determined for the *tlp(-)* (1.29) and Δtail (1.43) sporozoites. This suggests that these parasite lines were able to move almost as efficiently during flow as in the absence of it (although the difference between before and after flow is statistically significant).

Table 3: Summary of flow assay experiments from wildtype, TLP knockout and TLP tail mutants. Data was collected from at least 2 different experiments from 2 different mosquito cages/feedings. At least 50-60 salivary gland sporozoites (17-24 days post infection) were analyzed for each parasite line.

Parasite line	Mean circles/100 s before flow	Mean circles/100 s after flow	ratio before/after flow	number of analyzed sporozoites
Wt (RG)	4.7	2.3	1.95	55
tlp(-)	4.0	3.1	1.29	60
receiver line (rl) (RG)	2.7	2.3	1.20	55
Δtail	3.3	2.3	1.43	60
W/A	4.0	2.2	1.81	61
Wt recon	2.4	1.3	1.92	53

*The ratios of the circles before/after flow after re-grouping the data suggested in Figure 34 reads: controls: 2.0, W/A: 1,8 and the deletions:1,3
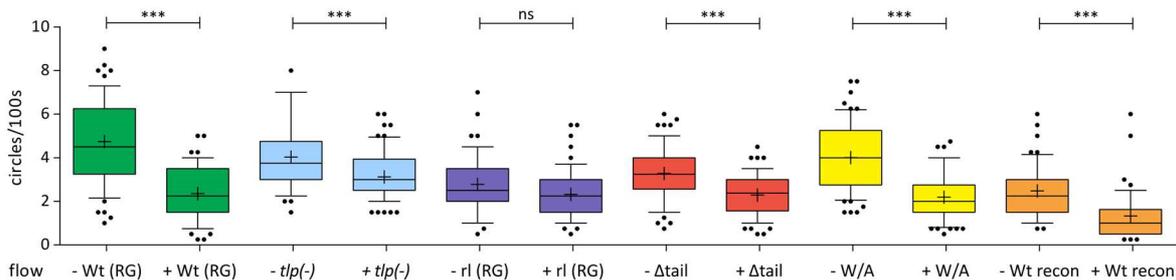
Figure 36: Induced flow '(+)' reduced average number of circles in all parasite line significantly except for the receiver line. Statistical test: not normally distributed, non-parametric t-test: Mann Whitney-test. Only sporozoites classified as gliding were examined. Whisker plots indicate 10 – 90% of all observed circles/100 s; box indicates 25–75 percentile; bar indicates median; + indicates arithmetic average.

Both *in vitro* assays examining the gliding capacity and moving patterns of the different parasite lines did not lead to strongly conclusive results although it appeared that the parasite lines that at least lacked the C-termini were not as sensitive to flow as the controls. The next step was to employ the optical tweezers set up and put the TLP tail mutants into relation with wildtype and the *tlp(-)* sporozoites.

3.3.3 Biophysical experiments: Optical tweezers (MMI CellManipulator)

For further analysis of the TLP tail mutants, new optical tweezers by MMI were used. This set up consists of an inverted microscope with a motorized stage and an electronically controlled, solid-state laser. The position of the trapping beam can be determined using computer-controlled galvo-mirrors. Drag force calibration to calculate the escape force is achieved by oscillating a bead trapped at a certain laser power with increasing frequencies until it is lost from the trap. The speed of the bead can be simply entered into the Stokes Equation with the values of bead diameter and viscosity of the surrounding medium to determine the drag force on the trapped particle.

Prior to investigating the TLP tail mutants, I tested the system with different wild type lines in order to reproduce the results from the experiments on the previously employed set up. However, the maximal force sporozoites produced in the new set up was 30 pN instead of the previously measured 70 pN.
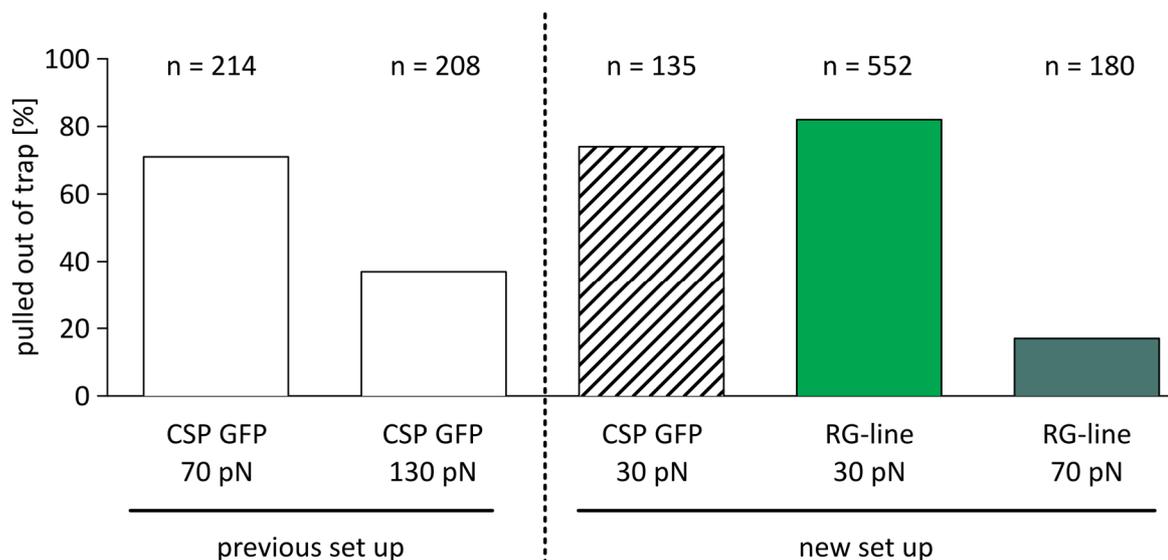
Figure 37: Comparison of wild type parasites of both the self-built and commercial optical tweezer systems at 70 pN and 130 pN (left side) or rather 30 pN and 70 pN (right side).

With the new optical tweezers, approximately 70 % of wildtype sporozoites (CSGFP, NK65 background) pulled the bead out of the laser trap at 30 pN (Figure 37, bar with stripes). In the former set up, the same percentage of sporozoites produced more than double the force, *e.g.* 70 pN (white bar). Over 80 % of the other wild type parasite line (RG-line, *Pb*ANKA) which is the appropriate wild type control for the TLP tail mutants, managed to pull the bead out at 30

pN. If the force is increased to 70 pN at the new system, only 17 % of the sporozoites were able to overcome the force with this laser power. When we almost doubled the force at the old system, approximately 40 % of the tested sporozoite pulled the bead out of the trap. Taking these results into account, I went on and challenged the TLP tail mutants with 30 pN and also re-measured the *tlp(-)* as reference.
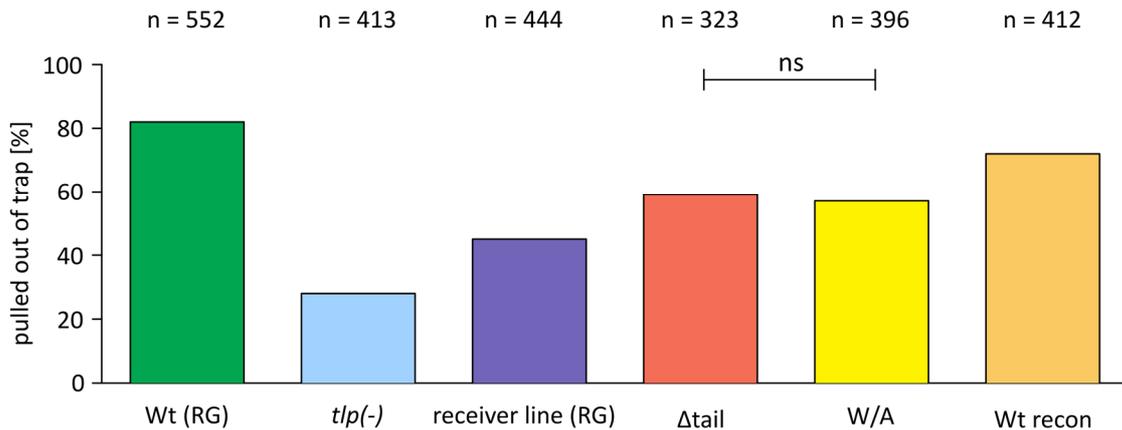
Figure 38: Force plot of wild type and TLP tail mutant salivary gland sporozoites probed at 30 pN. Forces of wildtype ranged between 70-80 % (green). Knock-out sporozoites (blue) were the weakest and TLP tail mutants ranked in between. Only Wt recon (orange) achieves comparable percentages. All tested parasite lines were highly significant different from each other except for the tail deletion and the amino acid swap. n = number of sporozoites probed. Significance bars from Fisher's exact test. The data was accumulated together with RISE student Sydney Sparanese.

The wildtype parasite line (RG: green) led to comparable results with the previous investigated wild type parasite line (CS GFP, bar with stripes Figure 37). 72-80 % of these tested sporozoites pulled the beads out at a laser trap force of 30 pN. The *tlp(-)* sporozoites were significantly weaker (Figure 38, blue bar). Only 28 % managed to pull the bead out. Surprisingly, the receiver line was stronger and 40 % produced a force of at least 30 pN. The sporozoites of the Δtail and the amino acid swap mutant (W/A) both pulled approximately 60 % of beads out of the trap. Sporozoites of the Wt recon restored the phenotype: 74 % pulled the bead out of the trap. Compared to the previous experiments, sporozoites of the *tlp(-)* parasite line were a bit stronger in the new tweezers set up (28 % vs. 20 %), which is also true for results of the wild type sporozoites (80 % vs. 72 %). The proportion between wildtype and knock-out stayed the same. The force experiments could only partially support the results from the cell motility based assays.

3.4 AFM analysis of *P. falciparum*-infected erythrocytes

The implementation of atomic force microscopy in malaria research can provide valuable new insight regarding knobs on the surface of infected erythrocytes (IEs). The dimension of these knobs is below the resolution limit of standard optical microscopy and their visualization necessitates nanometer resolution, which can be provided by AFM.

The experimental outline is displayed in Figure 39. Giemsa-stained blood smears from a late-stage dominated *Plasmodium falciparum* blood culture were mounted onto the AFM holder. Under ambient conditions, air dried infected erythrocytes were imaged in dynamic mode. The cantilever's oscillation amplitude changed with sample surface topography, and the topography image was obtained by monitoring these changes and closing the z feedback loop to minimize them. Exemplary AFM micrograph of infected erythrocytes at the trophozoite- and schizont-stage with corresponding light microscope images stained with Giemsa are illustrated in Figure 40. The knob protrusions are difficult to

Figure 39: Atomic Force Microscope imaging in dynamic mode. Sample under investigation: infected erythrocyte with knobby surface. Cantilever is oscillated close to resonance frequency. Height changes alter the cantilever oscillation, which is used to adjust the tip-sample distance. Note: drawing not to scale

identify at this whole-cell magnification and the precise calculation of knob density necessitates a lower scan size, where the separate knobs become much more evident and distinguishable (Figure 40 B, C). The 3D aspect of the AFM images is achieved by a color scaling with a dark color for low lying areas and the protrusions becoming gradually brighter (Figure 40 B, C, D).

A
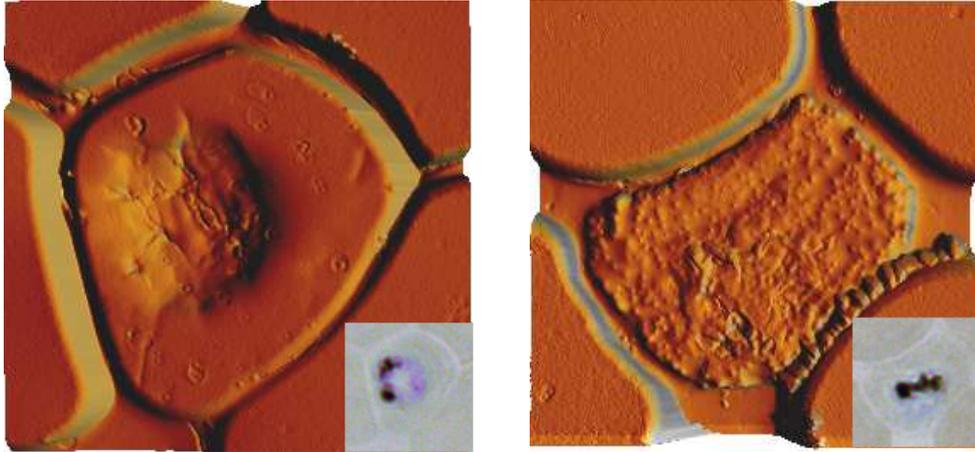
B
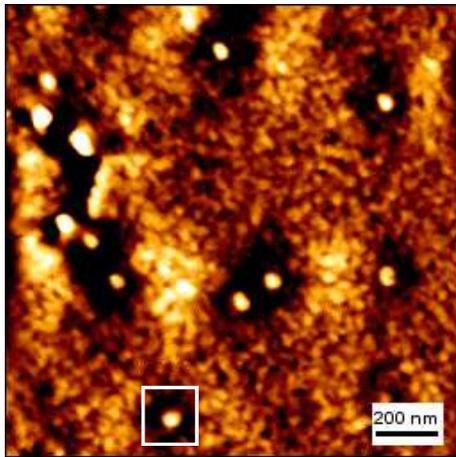
C
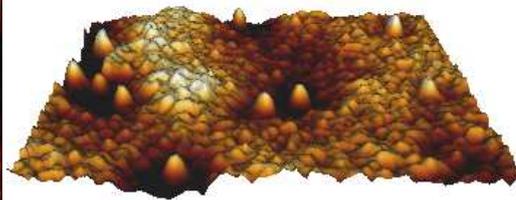
D
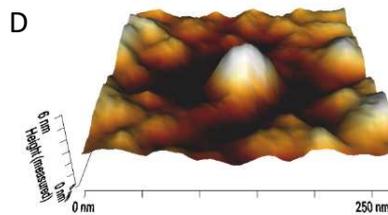
Figure 40: Analysis of infected erythrocyte surfaces at different magnifications. AFM micrographs of a trophozoite (left) and a schizont (right). The scan width was 10 µm. The corresponding light microscope images on the bottom right corner was Giemsa-stained and imaged using a 100x oil immersion objective). Note: The part of the erythrocyte membrane directly above the parasite is depressed. Only areas where the parasite has not disturbed the surface are used for analysis (B) Height image of 1.5 x 1.5 µm scan area showing knobs on the surface (bright spots) and (C) the corresponding 3D reconstruction. The knob density of this section was 5.3 knobs/µm^2 (D) Zoom in of B (white square) of a single knob after 3D reconstruction.

For measurement of the knob dimensions *i.e.* height and diameter, the height image (measured) of the AFM scan was analyzed with the cross-section tool of the JKP processing software (Figure 41).
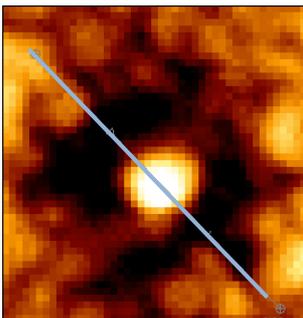
A   B
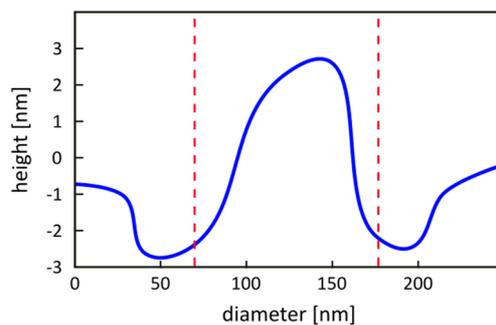
Figure 41: (A) Exemplary height image of a single knob (white box in Figure 40 B+D). (B) Line plot across the knob displayed in (A). Blue line follows the outline of the knob. Red dotted vertical lines flank the knob indicating the width, in this case approx. 100 nm the height corresponds to 5 nm.

3.4.1 Knob density of parasite - infected erythrocytes expressing *var*2CSA

The objective of the AFM experiments in this thesis was to determine the knob density of the lab-adapted parasite strain FCR3 expressing the *Pf*EMP1 variant *var*2CSA implicated in pregnancy-associated malaria. Samples were taken at three times point during the intra-erythrocytic cycle from a tightly synchronized parasite cell culture and subsequently analyzed at the AFM. This was done in collaboration with Dr. Cecilia Sanchez from the group of Prof. Michael Lanzer at the University of Heidelberg.

For each time point at least 12 cells were analyzed (Figure 42). The knob density of the first time point (20 – 24 h) ranged between 1 - 5 knobs/μm^2. For the 2nd time point (27 – 31 h), knob number increased to 5 - 16 knobs/μm^2 which was followed by a decrease in knob number with 4 - 8 knobs/μm^2 for the last time point (35 – 39 h).
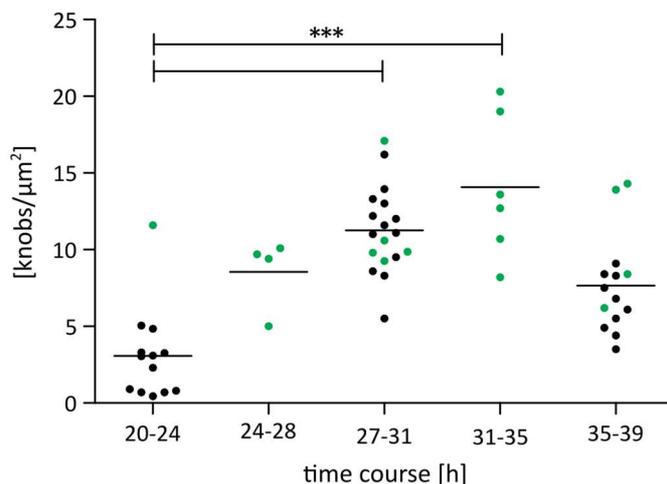
Figure 42: Quantification of knobs from combined data sets of time course (black dots) and mixed population (green dots) (Rieger et al., 2015). Knob density increased over time until 31 - 36 h post infection. Knob number on infected cells (35 – 39 h post) infection decreased. Statistical analysis: data not normally distributed. non-parametric test: Kruskal-Wallis-Test, horizontal bar: median

In addition to the data from the time course, knob quantification data I obtained for a publication (Rieger et al., 2015) was included in the plot since the parasite line FCR3 expressing the same *Pf*EMP1 variant was analyzed in this study (Figure 42). The parasite culture was not synchronized at the time; hence the parasite age was assessed by their morphology after Giemsa - staining at the light microscope. The data set complemented the knob numbers from the time course. Knob numbers reached a maximum at 31 – 35 hours. Again, knob densities on schizonts (35-39 h) seemed to drop in this data set. After testing for normal distribution, a non-parametric test (Kruskal-Wallis) showed significant differences between the first time point and 27 – 35h and 31 - 35h.

3.4.2 Knob morphology and formation in parasitized HbAA and HbAS erythrocytes

Hemoglobinopathies partially protect carriers from the severe, life-threatening manifestations of the *P. falciparum* pathogenesis. For this part, the AFM was employed to examine parasite-infected erythrocytes with different hemoglobin variants with regard to knob density and morphology. Samples were provided by Christine Lansche from the group of Prof. Michael Lanzer. The parasite lines were selected to predominantly express three *Pf*EMP1 *i.e.* IT4var 13, IT4var25, and IT4var66, which were shown to confer binding to CD36 and ICAM-1 (Avril et al., 2013; Brown et al., 2013) both host cell receptors of activated endothelial cells. The parasites were cultured with blood from healthy donors (HbAA) and with blood from patients who carry the heterozygous sickle cell trait (HbAS). The culture was categorized into trophozoites (24 ± 6 h post invasion) and the more mature schizont stage (36 ± 6h post invasion).

After AFM scanning the infected erythrocyte surface of the respective parasite populations, I calculated the knob densities and measured the knob dimensions of each cell. The range of the knob densities as well as the knob height and diameter including the knob surface values were summarized in Table 4.

Table 4: Summary of knob density of HbAA/HbAS trophozoites and schizonts. Range of densities represented counting of 16 HbAA and HbAS trophozoites. Knob number of schizonts were counted from 10 cells. From each cell five knobs were measured for this analysis. The median is displayed in brackets.

	HbAA trophozoites	HbAA schizonts	HbAS trophozoites	HbAS schizonts
knob density [knobs/µm^2]	1.6 - 10.5 (4.60)	3.7 - 12.9 (6.48)	1.3 - 9.5 (3.18)	2.9 - 9.5 (6.17)
knob diameter [nm]	51 - 125	56 - 135 nm	57 - 130	66 - 146
knob height [nm]	3 - 16	4 - 18	5 - 20	5 - 25
knob surface [nm^2]	2156 - 12429 (4700)	2630 - 13804 (6146)	2651 - 14618 (7961)	3295 - 17193 (7811)

The single knob density values are plotted in Figure 43 A and knob height and diameter were used to calculate the surface of the knob which is shown in Figure 43 B. The knob surface was approximated as as sperical cap (see Methods and Materials 2.5.3). I found no statistical significant differences in knob densities between trophozoites (Figure 43 A) or schizonts of erythrocytes carrying HbAA or HbAS. However, knobs appeared more abundant on infected erythrocytes at the schizont stage (median 6,48 and 6,17) than at the trophozoite stage (median 4,60 and 3,18). The knobs on parasitized HbAS erythrocytes of trophozoite and

schizont stages seemed of very similar sizes (Figure 43 B and Table 4). Trophozoites in red blood cells carrying wild type hemoglobin had the smallest knobs (Figure 43 B), but knob surface of parasitized HbAA erythrocytes increased during the development of the parasite (Figure 43 B). The average knob surface of trophozoites HbAS erythrocytes were larger compared to trophozoites of HbAA erythrocytes. The statistical analysis showed no significant difference in knob numbers between schizonts in HbAA erythrocytes and schizonts in HbAS erythrocytes, but Table 4 suggests, that schizonts in HbAS erythrocytes tend to have slightly larger knobs.
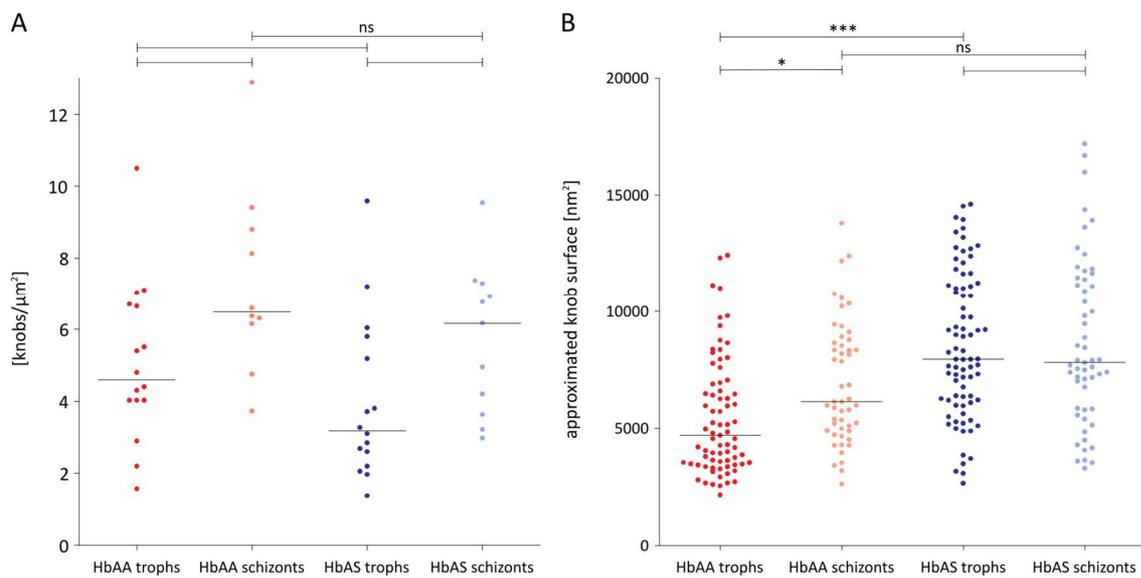
Figure 43: Knob densities and dimensions of late parasite stages on healthy and HbAS erythrocytes. (A) Knob density counted on parasitized HbAA erythrocytes over time. Trophozoites in red (n = 16) and schizonts in pink (n = 10) in comparison with knob density of iRBCs with HbAS. Trophozoites in blue (n = 16) and schizonts in light blue (n = 11) (B) Knob surface approximated as a spherical cap calculated by using diameter and height values. Statistical analysis: data not normally distributed; non-parametric test: Kruskal-Wallis.

.

4 Discussion

Cell migration and the interplay of adhesion, force and retrograde flow has been investigated for decades in many different types of cells. In this thesis, I studied the force generation and actin flow in *Plasmodium berghei* sporozoites and the role of the surface protein TLP during gliding motility.

4.1 Optical tweezers measure forces on the cellular and single-molecule level

In order to understand force production during cell motility, measuring cellular force globally and forces on the single - molecule level are equally important. Optical tweezers can do both and have been key to resolve the mechanisms behind the power strokes, steps and forces of cytoskeletal motors. Force clamps or isotonic clamps are used to study displacement measurements of processive molecular motors like myosin V (Rief et al., 2000). The distance between the bead and the trap is continuously monitored through a position detector. As the distance of the bead to the trap center changes, a feedback system rapidly moves the trap to keep the distance, and thus the force, constant (Figure 44 A).

Opposite to this configuration is feedback-enforced position-clamping. The center of the trap moves by the amount proportional to the applied force, essentially preventing bead movement. The displacement of the trap position is used as a measure for the isometric forces of myosin motors. This was first introduced for the 'three bead assays'. Here, an actin filament is suspended between two beads that are held by separate traps and single myosin molecules are coated onto the surface of a silica bead (Figure 44 B). The bead position and thus the myosin power stroke was monitored by a quadrant photodiode detector (4QD). This assay was mainly used to investigate non-processive molecular motors such as skeletal muscle myosin (Finer et al., 1994; Molloy et al., 1995).
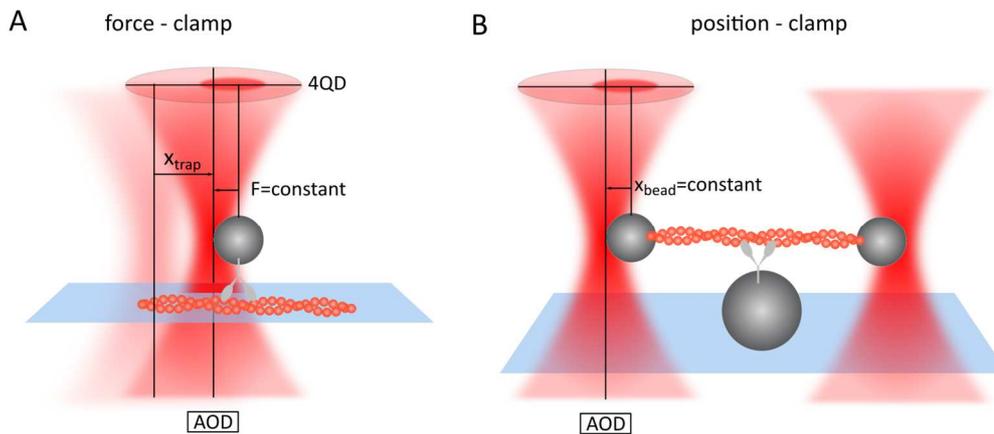
Figure 44: (A) Force-clamp or isotonic clamp: A feedback system moves the trap to keep the force on the bead constant. The trap movement (x_{trap}) corresponds to the displacement of the motor protein. (B) Position-clamp: Two polystyrene beads are stably held in the laser traps with an actin filament suspended between them. In closed feedback, the bead position (x_{bead}) is detected and thereby the force measured. The bead position is imaged onto a four-quadrant detector (4QD) and the positions are monitored with nanometer resolution.

Investigation of *Plasmodium* motor components in *in vitro* gliding assay only using purified protein is challenging because, parasite-actin is highly unstable (Skillman et al., 2011; Vahokoski et al., 2014) and might be incompletely folded when expressed in heterologous expression systems (Olshina et al., 2016). Only recently, a study could demonstrate, that *Pf*ACT1 and *Pf*MyoA (which requires an UCS family chaperone) and can be heterogeneously and functionally expressed yielding result comparable with skeletal muscle actin in *in vitro* motility assay (Bookwalter et al., 2017).

At the beginning of this study recombinant functional MyoA was not available so we used optical tweezers to analyze the cellular forces of whole gliding salivary gland sporozoites. These motile cells are equipped with a minimal set of regulatory elements and functional proteins hence possibly bridging our knowledge of complex cellular forces of higher eukaryotes and *in vitro* - measured single-molecule forces. The sporozoite serves as a model to understand the underlying mechanism of adhesion, force production and cell motility.

4.2 Force in *Plasmodium* sporozoites

In contrast to previously described motility experiments with proteins that assess the force of single myosins, we determined the maximal cellular force that sporozoites can produce by measuring the escape force *i.e.* the force necessary to completely pull the bead out of the trap. During my thesis I worked with two optical tweezer systems that led to results

considerably differing from each other. Since the previous holographic optical tweezers set up was not available anymore, it was challenging to retrace technical differences. Both systems were calibrated measuring the escape force by applying an external drag force, however the drag forces were generated using different approaches. At the first system, the constant flow velocity was achieved by a syringe pump pulling at a constant rate generating the desired steady flow of the bead solution. By tracking beads moving in the same focus plane the corresponding velocity of the flow was calculated. The new system allowed escape force determination by harmonically oscillating the trapped bead using a galvo-mirror with a horizontal amplitude. The oscillation frequency at which the bead is lost, provides the threshold frequency for calculating the escape force at the chosen laser intensity. To verify the results from the oscillation process, I calculated the escape force manually with the given parameters, checked the software-assisted amplitude by tracking the bead displacement as well as piezo-stage movement and confirmed the pixel factor by using a calibration slide. I found no evidence for any miscalculations.

Beside the technical differences of the two systems, also environmental parameters must be considered as they might affect sporozoite gliding behavior and thus the observed differences in force generation. For instance, temperature changes strongly influence sporozoite motility. At 37°C, sporozoites moved faster, but for a shorter period of time, while gliding speed of sporozoites at 24°C remained constant over a longer time period (Hegge et al., 2009). Also, long radiation exposure (over 200 s at 100 mW) was shown to limit sporozoite survival (Hegge et al., 2012). I did not investigate the effects of phototoxicity at the new system, however all probed sporozoites moved either continuously under the laser trap or recovered gliding afterwards, ensuring cell viability. The near-infrared wavelength of the lasers from both set ups (1064 nm and 1070 nm respectively) is well-suited to investigate biological samples due to their low absorption in this range. Taken together, the cause responsible for the difference in maximal force could not be resolved yet and needs further investigation. Whether sporozoites can produce on average 100 pN (70 – 190 pN, HOT) or only 30 pN (CellManipulator) makes a substantial difference for estimating the number of myosin heads responsible for that generated force.

Previous investigations using the three-bead assay have recorded single myosin II (double-headed myosins) isometric forces varying from 1 to 7 pN (Finer et al., 1994). Also, single heads are capable to move actin and produce force, suggesting that a dimeric structure is not necessary for effective force generation *in vitro* (Molloy et al., 1995). However, it was shown that a single-headed myosin generates half the displacement and unitary force of double-headed myosin (Tyska et al., 1999). Based on this, it was proposed that only one head productively interacts with actin whereas the second head weakly interacts, optimizing the mechanical performance of the second head.

Force in *Apicomplexan* parasites is also produced by a single-headed myosin class. Another study using a laser trap set up stated that *T. gondii* tachyzoites produce forces of 3.3 pN along the main axis theoretically involving around 8 myosin heads (Stadler et al., 2017) inferring that a myosin head produces 0.2 to 0.6 pN (Rao et al., 2009; Vanburen et al., 1995). Both studies referenced in this paper, were performed with double-headed myosins isolated from mammalian muscle tissue. Since there is conflicting evidence on how much force can be generated by myosin heads and the fact, that we determined the escape force in our experiment in contrast to other studies makes the interpretation and possible conclusion regarding of myosin heads involved more difficult.

Independent from this problem, the space the glideosome can occupy in *Plasmodium* sporozoite and the availability of actin filaments is limited. Studies on *Apicomplexan* actin reported that *T. gondii* actin and *Plasmodium* actin I form filaments only ∼100 nm in length (Dobrowolski et al., 1997; Sahoo et al., 2006; Schmitz et al., 2005; Schmitz et al., 2010; Vahokoski et al., 2014). Since MyoA is anchored into the IMC of the *Plasmodium* sporozoite facing outward (Jones et al., 2012), it can only bind to actin filaments in a certain orientation. Therefore, a potential binding site on actin in a matching position becomes available only every half-axial repeat on the filament. This corresponds to a distance of every 37 nm in mammalian cells (Mehta et al., 1999) and parasite actin II while in parasite actin I the crossover distance amounts to 40.6 nm (Vahokoski et al., 2014). This model assumes a static state of the actin filament being incapable to twist or change its position along its axis, which suggests that only three myosin heads can bind to an actin filament of that length (Figure 45). According to

this, the measured forces in our experiments and available binding site on the actin filament do not add up.

A possible explanation for this could be that more than one actin filament might be accessible for one myosin head at the time or more myosin heads are allowed to bind on available actin binding sites at once. Also, a cooperative effect that would increase the force with the number
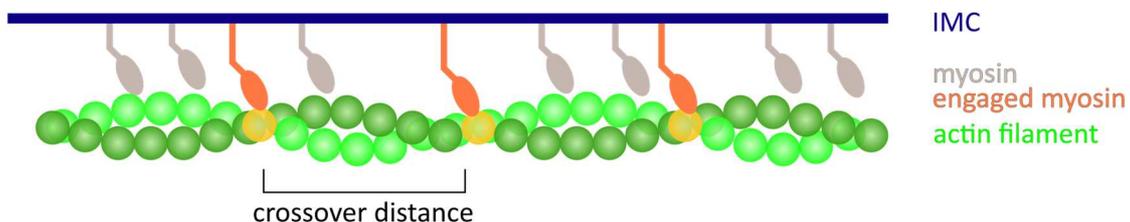
Figure 45: Hypothetical model of available actin binding sites for myosin heads. Myosin heads (orange) can bind to actin (green) every half-axial repeat on the filament (yellow monomer). The cross-over distance in mammalian actin and parasite actin II is 37 nm and for parasite actin I is 40.6 nm.

of engaged myosin molecules might be possible. Further, it must be considered that force generation and directed movement on actin are possible only during periods when the myosin is strongly bound to actin. The fraction of the ATPase cycle that the myosin spends in these strong-binding states is called the duty ratio (De La Cruz and Ostap, 2004). It was described, that *Tg*MyoA has a very low duty ratio of 0.77 % *in vitro* (Heaslip et al., 2010), which means, that in order to achieve continuous actin filament movement, a higher density of myosins is required to ensure that at least one is bound to the actin filament at any given instant.

Regarding the maximal forces we measured on the dorsal side of the sporozoites, our results were similar to those obtained with traction force microscopy measuring forces exerted on two-dimensional elastic substrates with imbedded fluorescent bead (Munter et al., 2009). Both methods measured forces in the same magnitude, but it is not known, how many receptor-ligand interactions are responsible or needed for the generated force. Estimating the contact area between bead and sporozoite and speculating about the engaged receptor number is difficult because we could not monitor the z-displacement of the trapped bead in our experiments. Studies of cellular forces using optical tweezers on fibroblasts (Schwingel and Bastmeyer, 2013) and on keratocytes (Galbraith and Sheetz, 1999) also reported forces, that fit the range of our values (80 - 160 pN). It seems that despite the differences in the machinery of those organisms, the net productive outcome of the force generating units that move a bead, is similar. The nature of bonds, that hold together our cells are noncovalent including van der Waals forces, hydrogen bonds or ionic bonds. The typical rupture force of

the strongest non-covalent bond between a receptor and a ligand reported for biotin-streptavidin interaction was found to be 160 pN (Florin et al., 1994). It is likely, that the generated force in our experiments might consist of several non-covalent bonds formed by sporozoite adhesins with host cell receptors. However, pure binding of the bead is probably also facilitated through the GPI-anchored circumsporozoite protein (CSP), which covers the most of the sporozoite surface (Swearingen et al., 2016). In order to activate sporozoite for gliding the medium contains 3 % BSA coating the beads possibly rendering the interaction between bead and sporozoite unspecific. Future experiments could include experiments in BSA-free medium and functionalized beads with specific ligands to dissect, which surface proteins are involved in mediating force and retrograde flow.

4.3 Retrograde flow in *Plasmodium* sporozoites

When sporozoites manage to pull the bead out of the laser trap, the bead is subsequently transported to the rear of the cell. This observation of retrograde flow was essentially first described in the late 19th century on motile gregarines moving ink particles along the cell body (Schewiakoff, 1894). Other early papers reported the same phenomenon referred to as "capping". It is defined as transport or redistribution of objects or molecules cross-linked to cell surface proteins toward the basal end of the cell. Capping was reported in *Eimeria* (Russell and Sinden, 1981), *Plasmodium* (Stewart and Vanderberg, 1991), *Gregarina* (Russell, 1983), and *Toxoplasma* (Dzbenski et al., 1976), but only on fixed parasites. Active transport of concanavalin-A coated microspheres was shown in living *Gregarina* at similar speeds to that of forward motion of the parasite (King, 1981). The current model proposes, that in migrating cells, actin polymerization occurs at the leading edge and is followed by retrograde motion of the actin network towards the cell center (Alexandrova et al., 2008; Gardel et al., 2008).

This is the first study investigating quantitatively retrograde flow in *Plasmodium* sporozoites. The measured speed of transported beads was faster (~ 7 μm/s) than the forward gliding of the sporozoite (~ 1-3 μm/s). The bead which has a relatively low mass enables us to track retrograde flow on a small contact area, while retrograde flow occurring on the side of the substrate, providing a larger contact area and thus a bigger resistance, ultimately enables the sporozoite to pull itself forward. We believe, that the sporozoite is equipped with the same machinery on its ventral and dorsal side only differently engaged to its optimal function. This

also agrees with the force data generated with different techniques (TFM at the ventral vs. OT at the dorsal side). An *in vitro* motility assay measured sliding velocities of actin filaments (rabbit skeletal actin) interacting with *Tg*MyoA of 5.2 µm/s (Herm-Gotz et al., 2002) and the most recent study conducted with parasite-derived motor components reported speed of 3 µm/s (Bookwalter et al., 2017), both supporting our observed retrograde flow speeds in wild type sporozoites. However, randomly-oriented and inactive myosins might limit the speed of the filaments (Homsher et al., 2003; Homsher et al., 1992). The fast flow could result from interactions between the myosin motor and actin filament coupled with transmembrane proteins. Upon engagement, surface adhesins would then link motor activity to retrograde flow, slowing it down for effective force transmission. Alternatively, the fast retrograde flow could also be explained by the secretion of membrane material (*e.g.* from micronemes) onto the parasite surface at the apical end followed by flow toward the rear due to the constant shedding of membranes at the posterior end. Currently, there are no other techniques available to support this linear motor model or to show actin flow. Parasite-actin cannot be visualized and other attempts using coronin mCherry, an F-actin binding protein, as a marker have failed to visualize actin filament transport. After activation, coronin re-localizes to the rear of the cell, but it was not possible to resolve the dynamics of this process. Also, FRAP-experiments, photo-bleaching a small patch of the plasma membrane containing CSP tagged with GFP, never led to any conclusive results, since the fluorescence recovered within ms from surrounding material and rearward flow was never documented (Singer, 2017).

It was hypothesized, that beads are moving along underlying paths organized along the cortical microtubules ensuring directionality (Stadler et al., 2017). Whether the structures underneath the pellicle serve as trajectories for bead translocation in sporozoites was not assessed in this thesis, but could be investigating by transgenic parasites with fewer numbers of microtubules (Benjamin Spreng unpublished data). As microtubules only span two thirds of the sporozoite length, but beads are transported to the very end of the cell, this theory seems, however, unlikely.

4.4 Modulation of actin dynamics interfere with force and flow

By treating sporozoites with increasing concentration with the actin polymerization inhibitor cytochalasin D, retrograde flow and force development are both affected. Intriguingly, the

speed of retrograde flow is affected to a lesser extent which is somewhat similar to the retrograde flow in higher eukaryotic cells (Forscher and Smith, 1988). The drug interacts with the barbed end, therefore preventing filament growth. Yet, it appears that the resulting short filament are moved back by myosins at the same speed and are still able to link to transmembrane proteins while gliding motility is already strongly impaired at 50 nM CytoD (Munter et al., 2009). Our findings that sporozoites produce less force under the influence of CytoD, have also been reported by traction force analysis, where parasites gliding on elastic substrates showed traction forces of about half of control forces (Munter et al., 2009). Previous studies on *Apicomplexan* parasites demonstrated that motility is blocked by CytoD (Dobrowolski and Sibley, 1996), but more specifically when sporozoites were allowed to settle in the presence of CytoD, most sporozoites attach only at the apical end (Hegge et al., 2010), whereas incubation with CytoD during gliding resulted in firm substrate attachment (Hegge et al., 2010; Munter et al., 2009). This suggests that actin dynamics not only play a role in gliding, but also in (secondary) adhesion site formation prior to motility. There is evidence that CytoD might have other targets or consequences than actin destabilization, although this effect only seems to occur at concentrations above 0.5 µM (Whitelaw et al., 2017).

The addition of the actin filament stabilizing agent Jasplakinolide caused an increase in retrograde flow and a reduction in force. In a different study, the same Jas-concentration (50 nM) led to increased gliding speeds in sporozoites, while higher concentrations of Jas resulted in less adhesion dynamics and weaker adhesion forces (Munter et al., 2009). Also, *T. gondii* tachyzoites moved faster after Jas-treatment, but also less productively with frequent changes in direction (Wetzel et al., 2003). The same study showed that Jas led to an interwoven organization of actin filaments instead of parallel bundles in untreated parasites. Further, Jas induces actin polymerization at the anterior end of the parasite, which causes the formation of a prominent apical protrusion (Shaw and Tilney, 1999) (Kudryashev unpublished). These studies suggest that dynamic and tightly regulated turnover of actin filaments is essential to achieve directional and productive motility. The lack of filament alignment might explain the impaired force transmission in our experiments.

On the other hand, longer filaments after the addition of Jas (Sahoo et al., 2006) could also facilitate tracks for faster bead transport. However, *T. gondii* tachyzoites treated with Jas (2 µM) displayed large bead displacements in random directions possibly suggesting that at this

concentration actin filament grow too long and or too quickly with insufficient orientation (Stadler et al., 2017). Transport in misoriented directions was only observed in immature sporozoites isolated from the hemolymph. The beads (or mosquito debris) were translocated back and forth on these sporozoites that display a type of motility termed patch-gliding (Munter et al., 2009) that is typical for hemolymph but not observed for salivary gland sporozoites (Figure 46). The peak speed of this bi-directional transport of beads reached values up to 12 µm/s, which is similar to retrograde flow speed of wild type sporozoites treated with 50 nM Jas. Thus, the potential to generate high flow speed is already present in immature sporozoite, but it is likely caused by a non-linear motor machinery rather than by drug-induced filaments. Alternatively, these hemolymph sporozoites might produce longer filaments, as they might not express high enough amounts of actin filament regulators.
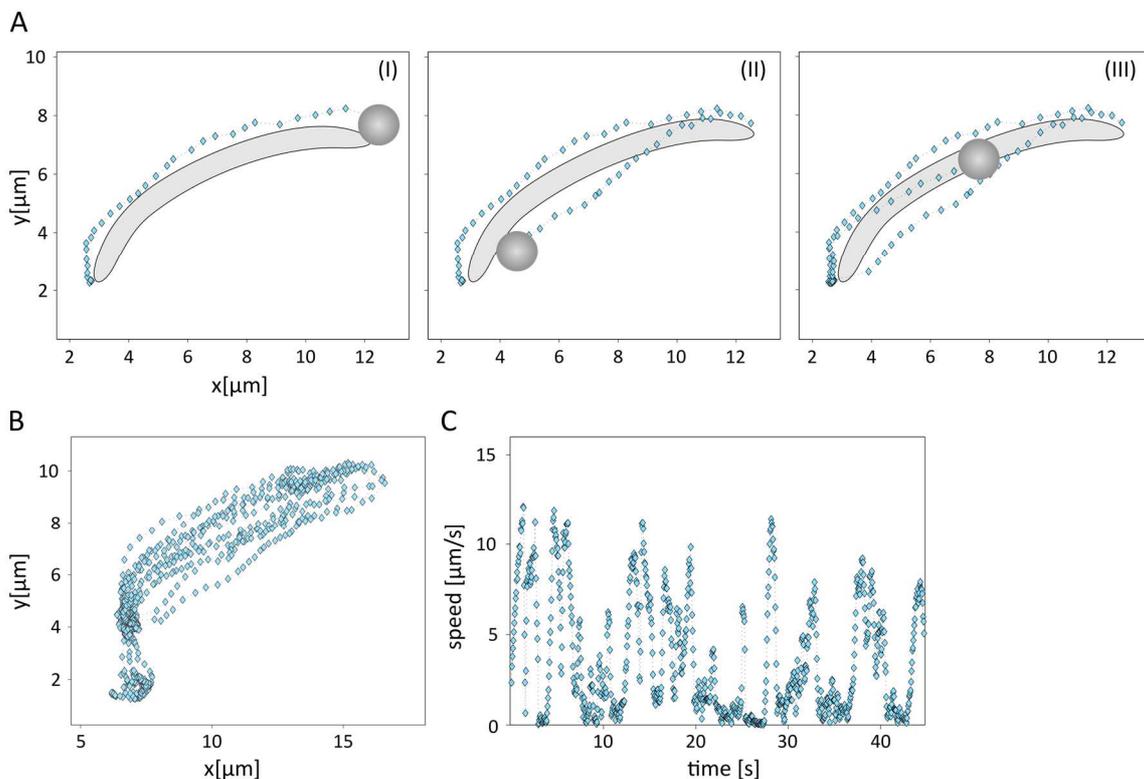
Figure 46: Bead trajectory along immature sporozoite isolated from the hemolymph (day 14 post infection). (A) Image sequence illustrates bead displacement along the hemolymph sporozoite. The bead is deposited on the front end of the sporozoite and translocated to the rear end of the cell (I). Then, the bead is moved back to the front end (II) and back again (III). (B) This back and forth transportation of the bead along the sporozoite surface is repeated multiple times summarized in the last panel showing the full trajectory plot over 40 s. (C) Corresponding speed plot with peaks of up to 12 µm/s.

The initiation of the bead transport is only affected by higher concentration of CytoD (200 nM) implying a role for actin filaments in coupling the bead to retrograde flow, but provides no direct further clue to understand the function of actin in this context.

4.5 TLP controls retrograde flow for force transmission

The force that propels the sporozoite forward is mediated by TRAP family proteins including TLP. They are secreted from micronemes to the plasma membrane of sporozoites after activation, (Carey et al., 2014) and are translocated to the posterior end during cell migration and invasion (Montagna et al., 2012). The localization of the signal from the C-terminally tagged TLP was rather inhomogeneous, but could be consistent with micronemal vesicles (Figure 28). TLP could not be detected on the sporozoite surface by antibody staining suggesting that TLP is either not exported to the surface, only present in undetectable amounts or not accessible by antibodies. To circumvent the latter, sporozoites could be treated with phospholipase C to cleave off the dense coat of GPI-anchored CSP and make the TLP more easily accessible. According to a comprehensive surface proteome analysis, expression of TLP was found to be two order magnitudes lower than TRAP or CSP (Lindner et al., 2013).

In the absence of TLP, sporozoites produce less force while the retrograde flow is increased compared to wild type sporozoite. In the force experiments, low concentrations of actin-modulating drugs could partially compensate for the lack of TLP. Jas had already been shown to rescue the decreased wild type and *tlp(-)* sporozoite motility on soft substrate (Hellmann et al., 2013), suggesting that increased actin polymerization might for example influence dynamics of protein secretion by raising the number of other adhesins on the sporozoite surface. However, how the effect of both drugs probably leading to shorter and more stable actin filaments positively influence the force production is not clear.

The retrograde flow in *tlp(-)* sporozoite was almost twice as high compared to wild type sporozoites, but when treated with Jas, wild type sporozoites reached similar values. Sporozoites lacking TLP, albeit showing the same phenotype as Jas-treated sporozoites, probably have a different underlying mechanism for enabling fast retrograde flow. One hypothesis, how retrograde flow and force are influenced by actin-modulating drugs and in the absence of TLP is illustrated in Figure 47. In wild type sporozoites, actin filaments could be organized either parallel to each other by TRAP-family proteins and/or bound myosin molecules. The force and actin flow lead to optimal gliding motility (Figure 47 A). The addition of CytoD leads probably to shorter filaments where less myosin heads and also fewer surface proteins can bind which might result in less force and slower flow (Figure 47 B). Under

stabilizing conditions, actin filaments are most likely longer and/or more numerous enabling faster flow, but skewed arrangements might disrupt effective force transmission (Figure 47 C). Without TLP in the plasma membrane, actin filaments could be less aligned possibly explaining the defect in force production and increased actin flow speed, because a speed controlling element is missing (Figure 47 D). Sporozoites with mutated profilin, an actin-binding protein sequestering G-actin to control actin polymerization *i.e*. filament length, were also characterized with fast retrograde flow rates and a defect in force production (Moreau et al., 2017). However, some of these mutant sporozoites were able to glide normally, while others were significantly impaired in gliding. These experiments point out that measuring flow speed and force is not enough to predict the interplay of the motor components on gliding behavior and that this needs further investigation. One of the main challenges that must be addressed is the visualization of F-actin in Plasmodium sporozoites at high resolution, which is currently not possible.
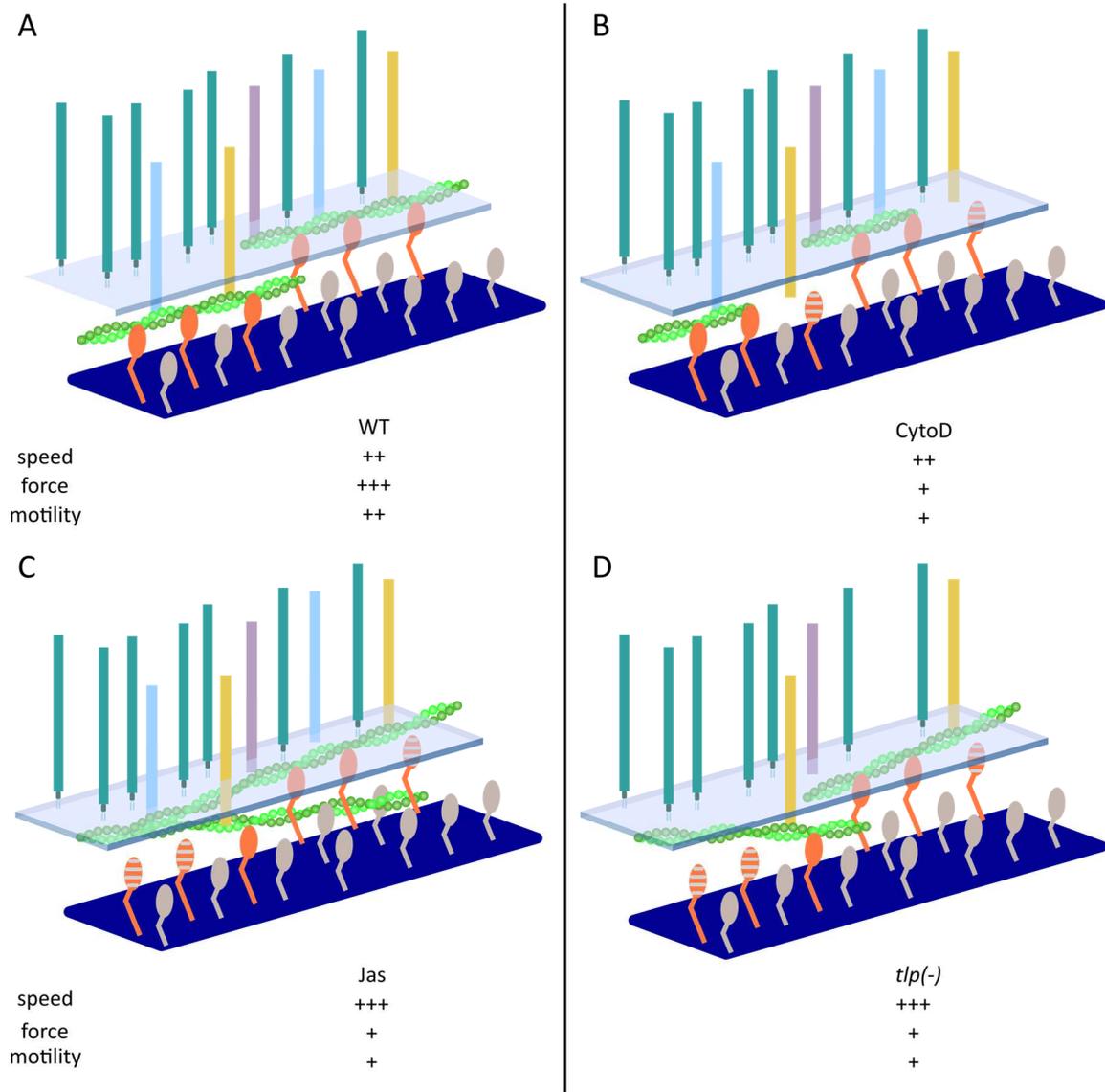
Figure 47: Speculative model of how actin organization affects retrograde flow, and myosin engagement sporozoite motility. The actin filaments (green) are bound and arranged by surface proteins: TLP (blue), TRAP (yellow) and S6 (violet). Note: CSP (dark green) does not connect with actin filament. The myosin heads (orange) interact with actin binding sites, while some myosin heads are not engaged (gray). Under actin-modulating conditions and in the absence of TLP, myosin heads that have no longer contact to the actin filament are depicted in gray/orange. The IMC anchoring the myosin molecules is illustrated in dark blue, while the plasma membrane has a transparent appearance. Plus signs indicate the level of speed, force and motility.

4.5.1 TLP as a "molecular clutch"

As suggested, TLP might act either in arranging actin filaments, limiting filament length or function as a "molecular clutch" integrating the retrograde flow of actin into directed force for motility. When the clutch is engaged, there is a decrease in the retrograde flow because the cytoskeleton-substrate linkage enables an effective transmission of the acto-myosin forces to the substrate via the adhesion complexes. In contrast, when the clutch is not

engaged (or a surface protein is missing) the loose coupling between the cytoskeleton and substrate results in an ineffective force transmission to the substrate and actin filaments are pushed backwards resulting in faster retrograde flow. By alternating between engaged and disengaged TLP (and possibly other surface adhesins such as TRAP), the parasite might regulate the formation and turnover of distinct adhesion sites during forward movement (Munter et al., 2009). During motility the sporozoite forms adhesion sites at the front, glides over them and needs to break these adhesion sites in the back of the cell to create progress. This process of alternating between attaching to and detaching from the substrate at certain regions is called "stick-slip" in which cells show cycles of fast and slow movement (Figure 48). The slip-like rapid movements are characterized by high turnover of adhesive sites, which correspond to a loose clutch, while less turnover is associated with slower movement (sticking) fitting the model of an engaged clutch and is associated with more force transmitted to the substrate.
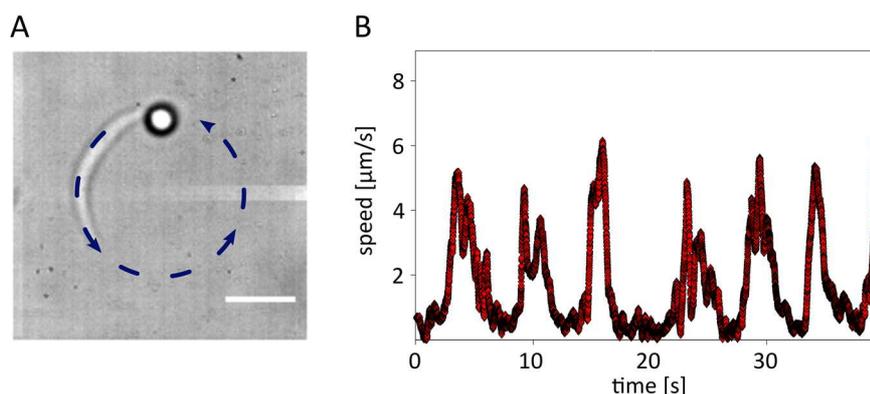
Figure 48: Illustration of a continuously gliding sporozoite with stick-and-slip phases (A) Image series of a gliding parasite with a bead stuck to the rear end performing multiple circles (blue dashed line). (B) The corresponding speeds exemplify the stop and go (slow and fast) movement of the sporozoite with peak speeds of up to 6 µm/s. Scale bars: 5 µm.

One example of a protein essential for gliding that can be engaged or disengaged, is TRAP, which can exist in two conformational states (open and closed) (Song et al., 2012), depending on ligand binding and possibly tensile force. This structural change could affect the interaction of TRAP with the gliding machinery, which might influence the behavior of the parasite. This mechanism has not yet been described for TLP, but it suggests that *Apicomplexan* adhesins are able to differentially function according to their environment.

4.5.2 Alternative function of TLP

As the C-terminus of TRAP has been implicated in regulating and possibly in signaling during gliding motility (Heiss et al., 2008; Kappe et al., 1999), I also investigated the C-terminus of TLP was in more detail. To that end I created several TLP mutants with altered C-termini: either introducing a point mutation (the least invasive alteration), deleting an intracellular acidic stretch (14 amino acids) or the whole C-terminus including the transmembrane domain (77 amino acids: receiver line, the most invasive alteration).

Surprisingly, all of the TLP tail mutants were able to produce more force than *tlp(-)* sporozoites. This suggests, that TLP does not fulfil the role of a classical micronemal adhesin, but might have a different function in force transmission during gliding. TLP could act as stabilizer of surrounding proteins (possibly taking on the role of the clutch) on the surface of sporozoite or might assemble them to initiate force transmission after activation (Figure 49 A, wild type II). TLP might indeed enable optimal force transmission by associating with other adhesins without involving the C-terminus (Figure 49 B, C). The lateral stabilization (black arrows) would be decreased in TLP tail mutants (Figure 49 B) and even further in the receiver line (C), but could only be completely lost in the *tlp(-)* parasites leading to the described
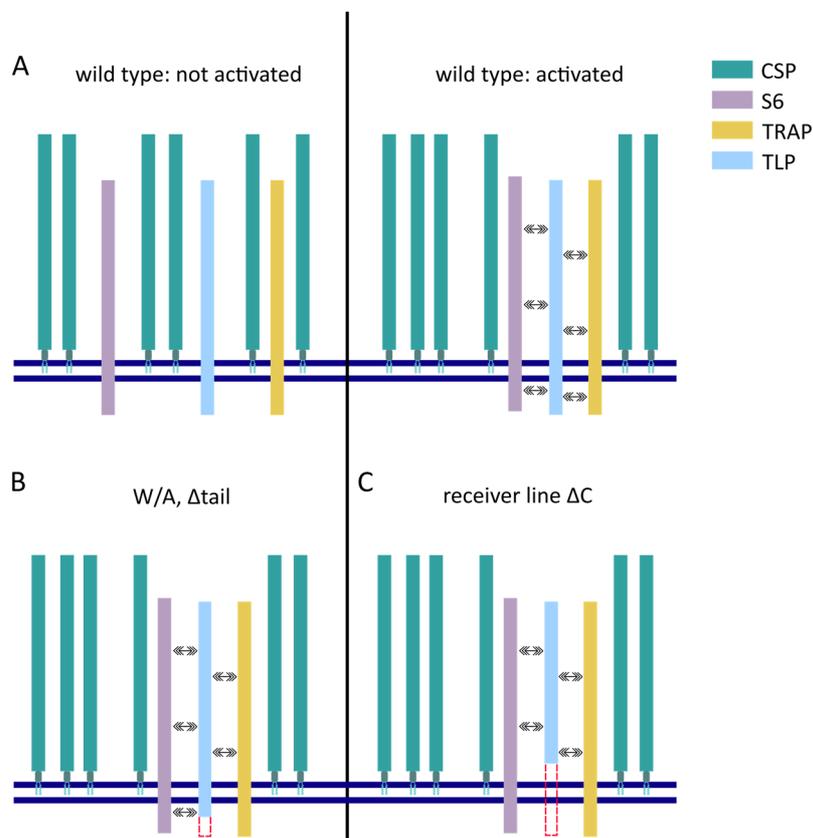
Figure 49: Hypothetical model of TLP localization within the plasma membrane. (A) The wild type situation in the non-activated state and activated state (for instance after contact with substrate or bead interaction). TLP (blue) recruits other adhesins (TRAP in yellow, S6 in violet) to confer optimal function. The arrows illustrate dynamic interaction between adhesins stabilising each other. (B) The TLP tail mutants lost stability, but are still able to recruit other adhesion and transmit force while (C) the receiver line is further impaired, but has residual function.

phenotype. Also, there is evidence that the cytoplasmic tail of TRAP can be replaced with that of TLP. As this only partially rescues the functionality of TRAP (Heiss et al., 2008), the cytoplasmic domain of TLP might only play a minor role in interacting with actin filaments. The importance of structural organization between integral membrane proteins has also been described for virus, e.g. the intracellular enveloped form of vaccinia virus where, protein function can still be accomplished even by restricted interaction (Rottger et al., 1999) supporting a similar model to that of TLP within the plasma membrane (Figure 49), where either a shortened C-terminus or the extracellular domains mediate interaction. As an example, Figure 50 illustrates that several transmembrane proteins exist in vaccinia virus. However, only one of them (A36R) directly impact actin dynamics, while the other transmembrane proteins laterally stabilize A36R. Together they initiate actin polymerization which pushes the virus forward, spreading the infection to neighboring cells.
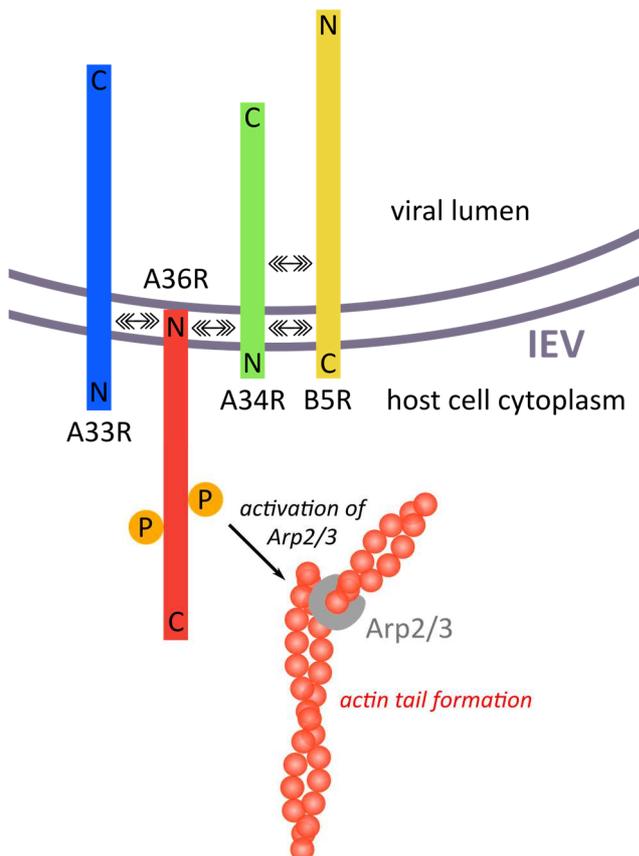
Figure 50: Model for vaccinia virus intracellular enveloped virus (IEV) membrane proteins. The protein A36R (red) responsible for actin tail formation by recruiting Arp 2/3. A33R (blue) stabilizes A36R through lateral interaction. Adapted from Rottger et al., 1999 and Ward et al., 2003

The latest annotation of TLP predicted the N-terminal signal peptide of TLP as a second transmembrane domain. This is supported by the presence of a tryptophan located at the potentially intracellular side of the transmembrane domain. Tryptophan residues were reported as a key residue in interactions of TRAP family adhesins with the cytoskeleton (Heiss et al., 2008; Kappe et al., 1999), but its role at the N-terminus of TLP has to be tested

experimentally. Yet, the existence of a second transmembrane domain could also help to explain the capacity of receiver line sporozoites to produce more force than *tlp(-)* sporozoites. To test this model of TLP, further experiments to show orientation and localization in the plasma membrane (FRET, high-resolution techniques) as well as evidence of interaction partners is needed. The recently in *Plasmodium* established method bioID (Kehrer et al., 2016a) used the biotin ligase BirA fused to the protein of interest which then subsequently biotinylated the surrounding proteins. This enables the identification of biotinylated proteins by mass-spectrometric analysis. Unfortunately, this was unsuccessful for TRAP fused to BirA leaving other techniques to explore interactions of TRAP-family adhesions with each other.

4.6 Imaging of *P. falciparum*-infected erythrocytes

Traditionally, transmission electron microscopy (TEM) and scanning electron microscopy (SEM) have been used to investigate the morphological changes of the parasitized red blood cells (Aikawa et al., 1983; Allred et al., 1986; Gruenberg et al., 1983). However, these techniques require extensive and time-consuming sample preparation which may affect the natural state of the cells.

Atomic force microscopy is a scanning probe technique that is based on mechanical interactions between the tip of a cantilever and a sample surface. It allows imaging of biological samples under physiological conditions down to nanometer scale resolution (Dufrene et al., 2017). Previous AFM-studies on malaria parasitized RBCs provided high quality images of knobs and allowed quantitative analysis (Li et al., 2006; Nagao et al., 2000; Quadt et al., 2012) and imaging of intracellular remodeled structures (Millholland et al., 2011; Shi et al., 2013).

4.6.1 AFM analysis of knob density and knob dimension

TEM data suggested that trophozoite-stage knobs appear smaller in diameter and denser than schizont-stage knobs (Langreth et al., 1978). In contrast, SEM studies described that knobs on trophozoite stage parasites become smaller, whereas knob density increases as parasites develop (Gruenberg et al., 1983). This tendency was also observed by AFM studies (Li et al., 2006; Nagao et al., 2000), although a decrease in knob number on late stages was also reported (Quadt et al., 2012). The measured knob densities vary greatly between the different

studies, because knob formation depends on the respective parasite line under investigation (Quadt et al., 2012), on culture conditions *in vitro* (Tilly et al., 2015) and also on the number of parasites inside the cell (Nagao et al., 2000).

Also, the sample preparation for electron microscopy might induce shrinkage of osmotically fragile infected erythrocytes (Gruenberg et al., 1983), which could result in the numeric discrepancy between the AFM and SEM data. A recent paper reported an estimated diameter of infected red blood cells by SEM (4.4 ± 0.4 μm) and a more physiological value of 8.0 ± 0.5 μm measured by AFM (Subramani et al., 2015). Inaccuracies in knob numbers could occur on late stage-infected cells *i.e.* schizonts which have a more distorted cell surface or membrane folds possibly concealing surface features and making a fraction of the knobs undetectable. However, during my measurements such uneven areas were disregarded, and images were only taken on relatively flat surface region. The knob density assessed in this study of the parasite line FCR3 expressing the *Pf*EMP1 variant *var*2CSA showed an increase over time, while knob numbers decreased again on infected erythrocytes at the schizont stage matching previously described data (Quadt et al., 2012).

Knobs of different lab- adapted parasite isolates investigated by TEM measure 30 - 40 nm in height (Aikawa, 1988) and with an average diameter of 100 nm and SEM data suggests a diameter range of 70 -160 nm (Gruenberg et al., 1983). AFM studies reported similar numbers for the knob diameter, but the values for the knob height were lower ranging on average between 5 to 10 nm (Aikawa et al., 1996; Li et al., 2006; Quadt et al., 2012) and up to 25 nm (Nagao et al., 2000). The values for the knob dimensions in this work were combined capturing the surface of the knob approximated as spherical cap.

4.6.2 AFM artefacts

When interpreting dimension measurements of a sample with the AFM, some precautions are needed with regards to instrumental artefacts. The AFM has a very high vertical resolution but
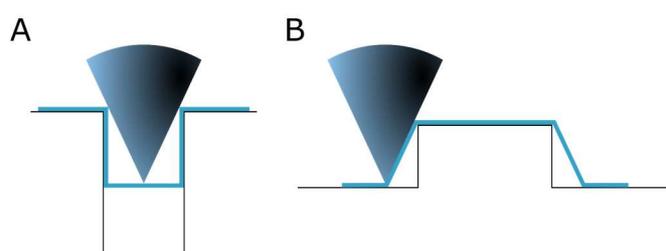

Figure 51: Effect of tip geometry on imaging. The outline (light blue) represents tip movement limited by its dimension following (A) a groove and (B) a protrusion. Due to finite size of the tip, artefacts are produced, and the resulting image is a convolution between the shape of the tip and the topography of the sample.

when probing soft biological samples there is a considerable deformation of the sample, which substantially lowers the vertical dimension of the surface features. In the lateral direction, the resolution is limited by the sharpness of the tip and small objects with dimensions close to the resolution will appear artificially enlarged as a consequence of the finite sharpness of the tip. The instrumental artefacts are expected to affect the samples in a proportional manner and magnify or diminish the knobs evenly for all infected erythrocytes.

4.6.3 Hemoglobin variants influence knob density and morphology

By analyzing the knob density and morphology on parasitized wild type and HbAS erythrocytes at the trophozoite and schizont stage, I contributed to a study that compared the adhesion dynamics in flow, cell shape, membrane elasticity and in silico modelling of these infected erythrocytes (Lansche et al., 2018 in preparation). I could show a 30 % reduction of knobs at the trophozoite stage on parasitized HbAS erythrocytes compared to infected erythrocytes with normal hemoglobin. However, the majority of knobs of these parasite population was significantly larger, a finding that was also reported on subsets of parasitized AS and SS erythrocytes (Cholera et al., 2008 Cyrklaff et al., 2016) and other hemoglobinopathic erythrocytes (Cyrklaff et al., 2012; Fairhurst et al., 2012; Taylor et al., 2013). This could mean, that the amount of knob material in HbAA and HbAS parasitized erythrocytes is similar, but differently distributed in the cell. However, it was proposed that this results from impaired trafficking of parasite-derived proteins to the host cell surface and disrupted interactions between the erythrocyte's membrane skeleton and the knobs (Cyrklaff et al., 2011).

The knob densities on both parasitized HbAA and HbAS erythrocytes at the schizont stage were comparable suggesting an optimum or maximum of knob prevalence for this particular parasite strain. The same could also be the case for the knob surface area, which was not statistically significant between infected HbAA and HbAS erythrocytes. This hypothesis is supported by the fact, that the knob size on parasitized HbAS erythrocytes is almost identical independent of parasite age.

The knob structures contribute to stiffening of the host cell plasma membrane, while the knob density is indicative of the number of possible *Pf*EMP1-ligand interactions and both play a part in defining binding capacity of mature infected erythrocytes. Thus, this AFM study helped to understand the adhesion dynamics of parasitized HbAA and HbAS erythrocytes.

5 Conclusion

This thesis provided new insight into the mechanism of gilding motility in *Plasmodium* sporozoites. The focus of my work was to study the function of the surface protein TLP in this process.

We created an experimental design in which optical tweezers, a non-invasive microscopic method that can manipulate small objects, enabled us to investigate live sporozoites moving in two dimensions. The data obtained using optical tweezers implicated that TLP controls the retrograde flow speed for optimal force generation, possibly by organizing actin filaments. I could show that retrograde flow in sporozoites is faster than the speed of their forward gliding and both force and retrograde flow depend on actin dynamics.

Further force experiments on sporozoites with truncated C-termini of TLP revealed that this protein might not directly interact with the actin-myosin motor but function by stabilizing surrounding surface proteins laterally. As a consequence, TLP as part of a macromolecular assembly might enable the cell to move forward at unusually high speeds.

.

6 References

Abercrombie, M., Heaysman, J.E., and Pegrum, S.M. (1970). The locomotion of fibroblasts in culture. 3. Movements of particles on the dorsal surface of the leading lamella. Exp Cell Res *62*, 389-398, PMID: 5531377.

Agop-Nersesian, C., De Niz, M., Niklaus, L., Prado, M., Eickel, N., and Heussler, V.T. (2017). Shedding of host autophagic proteins from the parasitophorous vacuolar membrane of Plasmodium berghei. Sci Rep *7*, 2191, PMID: 28526861.

Aikawa, M. (1988). Human cerebral malaria. Am J Trop Med Hyg *39*, 3-10, PMID: 3041856.

Aikawa, M., Kamanura, K., Shiraishi, S., Matsumoto, Y., Arwati, H., Torii, M., Ito, Y., Takeuchi, T., and Tandler, B. (1996). Membrane knobs of unfixed Plasmodium falciparum infected erythrocytes: new findings as revealed by atomic force microscopy and surface potential spectroscopy. Exp Parasitol *84*, 339-343, PMID: 8948323.

Aikawa, M., Rabbege, J.R., Udeinya, I., and Miller, L.H. (1983). Electron microscopy of knobs in Plasmodium falciparum-infected erythrocytes. J Parasitol *69*, 435-437, PMID: 6343577.

Alberts, B., Johnson, A., Lewis, J., Raff, M.C., Roberts, K., and Walter, P. (2002). Molecular biology of the cell, fourth edition edn.

Alexandrova, A.Y., Arnold, K., Schaub, S., Vasiliev, J.M., Meister, J.J., Bershadsky, A.D., and Verkhovsky, A.B. (2008). Comparative dynamics of retrograde actin flow and focal adhesions: formation of nascent adhesions triggers transition from fast to slow flow. PLoS One *3*, e3234, PMID: 18800171.

Allred, D.R., Gruenberg, J.E., and Sherman, I.W. (1986). Dynamic rearrangements of erythrocyte membrane internal architecture induced by infection with Plasmodium falciparum. J Cell Sci *81*, 1-16, PMID: 3525580.

Aly, A.S., and Matuschewski, K. (2005). A malarial cysteine protease is necessary for Plasmodium sporozoite egress from oocysts. J Exp Med *202*, 225-230, PMID: 16027235.

Amino, R., Giovannini, D., Thiberge, S., Gueirard, P., Boisson, B., Dubremetz, J.F., Prevost, M.C., Ishino, T., Yuda, M., and Menard, R. (2008). Host cell traversal is important for progression of the malaria parasite through the dermis to the liver. Cell Host & Microbe *3*, 88-96, PMID: 18312843.

Amino, R., Thiberge, S., Martin, B., Celli, S., Shorte, S., Frischknecht, F., and Menard, R. (2006). Quantitative imaging of Plasmodium transmission from mosquito to mammal. Nat Med *12*, 220-224, PMID: 16429144.

Andenmatten, N., Egarter, S., Jackson, A.J., Jullien, N., Herman, J.P., and Meissner, M. (2013). Conditional genome engineering in Toxoplasma gondii uncovers alternative invasion mechanisms. Nat Methods *10*, 125-127, PMID: 23263690.

Andreadaki, M., Morgan, R.N., Deligianni, E., Kooij, T.W., Santos, J.M., Spanos, L., Matuschewski, K., Louis, C., Mair, G.R., and Siden-Kiamos, I. (2014). Genetic crosses and complementation reveal essential functions for the Plasmodium stage-specific actin2 in sporogonic development. Cell Microbiol *16*, 751-767, PMID: 24471657.

References

Arie, T., Fairhurst, R.M., Brittain, N.J., Wellems, T.E., and Dvorak, J.A. (2005). Hemoglobin C modulates the surface topography of Plasmodium falciparum-infected erythrocytes. J Struct Biol *150*, 163-169, PMID: 15866739.

Ashkin, A., Dziedzic, J.M., Bjorkholm, J.E., and Chu, S. (1986). Observation of a Single-Beam Gradient Force Optical Trap for Dielectric Particles. Opt Lett *11*, 288-290, PMID: 19730608.

Avril, M., Brazier, A.J., Melcher, M., Sampath, S., and Smith, J.D. (2013). DC8 and DC13 var genes associated with severe malaria bind avidly to diverse endothelial cells. PLoS Pathog *9*, e1003430, PMID: 23825944.

Baer, K., Roosevelt, M., Clarkson, A.B., Jr., van Rooijen, N., Schnieder, T., and Frevert, U. (2007). Kupffer cells are obligatory for Plasmodium yoelii sporozoite infection of the liver. Cell Microbiol *9*, 397-412, PMID: 16953803.

Baker, R.P., Wijetilaka, R., and Urban, S. (2006). Two Plasmodium rhomboid proteases preferentially cleave different adhesins implicated in all invasive stages of malaria. PLoS Pathog *2*, e113, PMID: 17040128.

Bane, K.S., Lepper, S., Kehrer, J., Sattler, J.M., Singer, M., Reinig, M., Klug, D., Heiss, K., Baum, J., Mueller, A.K.*, et al.* (2016). The Actin Filament-Binding Protein Coronin Regulates Motility in Plasmodium Sporozoites. PLoS Pathog *12*, e1005710, PMID: 27409081.

Barry, A.E., Leliwa-Sytek, A., Tavul, L., Imrie, H., Migot-Nabias, F., Brown, S.M., McVean, G.A., and Day, K.P. (2007). Population genomics of the immune evasion (var) genes of Plasmodium falciparum. PLoS Pathog *3*, e34, PMID: 17367208.

Battista, A., Frischknecht, F., and Schwarz, U.S. (2014). Geometrical model for malaria parasite migration in structured environments. Phys Rev E *90*, PMID: 25375536.

Baum, J., Tonkin, C.J., Paul, A.S., Rug, M., Smith, B.J., Gould, S.B., Richard, D., Pollard, T.D., and Cowman, A.F. (2008). A malaria parasite formin regulates actin polymerization and localizes to the parasite-erythrocyte moving junction during invasion. Cell Host Microbe *3*, 188-198, PMID: 18329618.

Bergman, L.W., Kaiser, K., Fujioka, H., Coppens, I., Daly, T.M., Fox, S., Matuschewski, K., Nussenzweig, V., and Kappe, S.H. (2003). Myosin A tail domain interacting protein (MTIP) localizes to the inner membrane complex of Plasmodium sporozoites. J Cell Sci *116*, 39-49, PMID: 12456714.

Beyer, K. (2017). Collective motion and adhesin dynamics of Plasmodium sporozoites. In Parasitology - Center for Infectious Diseases (Heidelberg: University of Heidelberg).

Bhanot, P., Frevert, U., Nussenzweig, V., and Persson, C. (2003). Defective sorting of the thrombospondin-related anonymous protein (TRAP) inhibits Plasmodium infectivity. Mol Biochem Parasitol *126*, 263-273, PMID: 12615325.

Bhanot, P., Schauer, K., Coppens, I., and Nussenzweig, V. (2005). A surface phospholipase is involved in the migration of plasmodium sporozoites through cells. J Biol Chem *280*, 6752-6760, PMID: 15590623.

Billker, O., Lindo, V., Panico, M., Etienne, A.E., Paxton, T., Dell, A., Rogers, M., Sinden, R.E., and Morris, H.R. (1998). Identification of xanthurenic acid as the putative inducer of malaria development in the mosquito. Nature *392*, 289-292, PMID: 9521324

References

Binnig, G., Gerber, C., Stoll, E., Albrecht, T.R., and Quate, C.F. (1987). Atomic Resolution with Atomic Force Microscope. Surf Sci *189*, 1-6,

Binnig, G., Quate, C.F., and Gerber, C. (1986). Atomic force microscope. Phys Rev Lett *56*, 930-933, PMID: 10033323.

Blackman, M.J., and Bannister, L.H. (2001). Apical organelles of Apicomplexa: biology and isolation by subcellular fractionation. Mol Biochem Parasitol *117*, 11-25, PMID: 11551628.

Blanchoin, L., Boujemaa-Paterski, R., Sykes, C., and Plastino, J. (2014). Actin dynamics, architecture, and mechanics in cell motility. Physiol Rev *94*, 235-263, PMID: 24382887.

Bookwalter, C.S., Tay, C.L., McCrorie, R., Previs, M.J., Lu, H., Krementsova, E.B., Fagnant, P.M., Baum, J., and Trybus, K.M. (2017). Reconstitution of the core of the malaria parasite glideosome with recombinant Plasmodium class XIV myosin A and Plasmodium actin. J Biol Chem, PMID: 28978649.

Braks, J.A., Franke-Fayard, B., Kroeze, H., Janse, C.J., and Waters, A.P. (2006). Development and application of a positive-negative selectable marker system for use in reverse genetics in Plasmodium. Nucleic Acids Res *34*, e39, PMID: 16537837.

Brown, A., Turner, L., Christoffersen, S., Andrews, K.A., Szestak, T., Zhao, Y., Larsen, S., Craig, A.G., and Higgins, M.K. (2013). Molecular architecture of a complex between an adhesion protein from the malaria parasite and intracellular adhesion molecule 1. J Biol Chem *288*, 5992-6003, PMID: 23297413.

Bubb, M.R., Senderowicz, A.M., Sausville, E.A., Duncan, K.L., and Korn, E.D. (1994). Jasplakinolide, a cytotoxic natural product, induces actin polymerization and competitively inhibits the binding of phalloidin to F-actin. J Biol Chem *269*, 14869-14871, PMID: 8195116.

Bullen, H.E., Tonkin, C.J., O'Donnell, R.A., Tham, W.H., Papenfuss, A.T., Gould, S., Cowman, A.F., Crabb, B.S., and Gilson, P.R. (2009). A novel family of Apicomplexan glideosome-associated proteins with an inner membrane-anchoring role. J Biol Chem *284*, 25353-25363, PMID: 19561073.

Carey, A.F., Singer, M., Bargieri, D., Thiberge, S., Frischknecht, F., Menard, R., and Amino, R. (2014). Calcium dynamics of Plasmodium berghei sporozoite motility. Cell Microbiol *16*, 768-783, PMID: 24617597.

Carter, R., and Diggs, C.L. (1977). Plasmodia of rodents, Vol 3 (New York: Academic Press).

Cecconi, C., Shank, E.A., Bustamante, C., and Marqusee, S. (2005). Direct observation of the three-state folding of a single protein molecule. Science *309*, 2057-2060, PMID: 16179479.

Cholera, R., Brittain, N.J., Gillrie, M.R., Lopera-Mesa, T.M., Diakite, S.A., Arie, T., Krause, M.A., Guindo, A., Tubman, A., Fujioka, H.*, et al.* (2008). Impaired cytoadherence of Plasmodium falciparum-infected erythrocytes containing sickle hemoglobin. Proc Natl Acad Sci U S A *105*, 991-996, PMID: 18192399.

Clausen, T.M., Christoffersen, S., Dahlback, M., Langkilde, A.E., Jensen, K.E., Resende, M., Agerbaek, M.O., Andersen, D., Berisha, B., Ditlev, S.B.*, et al.* (2012). Structural and Functional Insight into How the Plasmodium falciparum VAR2CSA Protein Mediates Binding to Chondroitin Sulfate A in Placental Malaria. Journal of Biological Chemistry *287*, 23332-23345, PMID: 22570492.

Combe, A., Moreira, C., Ackerman, S., Thiberge, S., Templeton, T.J., and Menard, R. (2009). TREP, a novel protein necessary for gliding motility of the malaria sporozoite. Int J Parasitol *39*, 489-496, PMID: 19000911.

References

Cooke, B., Coppel, R., and Wahlgren, M. (2000). Falciparum malaria: sticking up, standing out and out-standing. Parasitol Today *16*, 416-420, PMID: 11006472.

Cooke, B.M., Lingelbach, K., Bannister, L.H., and Tilley, L. (2004). Protein trafficking in Plasmodium falciparum-infected red blood cells. Trends Parasitol *20*, 581-589, PMID: 15522668.

Cooper, J.A. (1987). Effects of cytochalasin and phalloidin on actin. J Cell Biol *105*, 1473-1478, PMID: 3312229.

Crabb, B.S., Cooke, B.M., Reeder, J.C., Waller, R.F., Caruana, S.R., Davern, K.M., Wickham, M.E., Brown, G.V., Coppel, R.L., and Cowman, A.F. (1997). Targeted gene disruption shows that knobs enable malaria-infected red cells to cytoadhere under physiological shear stress. Cell *89*, 287-296, PMID: 9108483.

Craig, A.G., Grau, G.E., Janse, C., Kazura, J.W., Milner, D., Barnwell, J.W., Turner, G., Langhorne, J., and participants of the Hinxton Retreat meeting on Animal Models for Research on Severe, M. (2012). The role of animal models for research on severe malaria. PLoS Pathog *8*, e1002401, PMID: 22319438.

Cramer, L.P. (1999). Role of actin-filament disassembly in lamellipodium protrusion in motile cells revealed using the drug jasplakinolide. Curr Biol *9*, 1095-1105, PMID: 10531004.

Crick, A.J., Theron, M., Tiffert, T., Lew, V.L., Cicuta, P., and Rayner, J.C. (2014). Quantitation of Malaria Parasite-Erythrocyte Cell-Cell Interactions Using Optical Tweezers. Biophysical Journal *107*, 846-853, PMID: 25140419.

Crocker, J.C., and Grier, D.G. (1996). Methods of digital video microscopy for colloidal studies. J Colloid Interf Sci *179*, 298-310, DOI: doi.org/10.1006/jcis.1996.0217.

Cyrklaff, M., Kudryashev, M., Leis, A., Leonard, K., Baumeister, W., Menard, R., Meissner, M., and Frischknecht, F. (2007). Cryoelectron tomography reveals periodic material at the inner side of subpellicular microtubules in apicomplexan parasites. J Exp Med *204*, 1281-1287, PMID: 17562819.

Cyrklaff, M., Sanchez, C.P., Frischknecht, F., and Lanzer, M. (2012). Host actin remodeling and protection from malaria by hemoglobinopathies. Trends in Parasitology *28*, 479-485, PMID: 22980758.

Cyrklaff, M., Sanchez, C.P., Kilian, N., Bisseye, C., Simpore, J., Frischknecht, F., and Lanzer, M. (2011). Hemoglobins S and C Interfere with Actin Remodeling in Plasmodium falciparum-Infected Erythrocytes. Science *334*, 1283-1286, PMID: 22075726.

Cyrklaff, M., Srismith, S., Nyboer, B., Burda, K., Hoffmann, A., Lasitschka, F., Adjalley, S., Bisseye, C., Simpore, J., Mueller, A.K.*, et al.* (2016). Oxidative insult can induce malaria-protective trait of sickle and fetal erythrocytes. Nat Commun *7*, 13401, PMID: 27824335.

Dao, M., Lim, C.T., and Suresh, S. (2003). Mechanics of the human red blood cell deformed by optical tweezers. J Mech Phys Solids *51*, 2259-2280, PMID: 20387977.

Dasanna, A.K., Lansche, C., Lanzer, M., and Schwarz, U.S. (2017). Rolling Adhesion of Schizont Stage Malaria-Infected Red Blood Cells in Shear Flow. Biophys J *112*, 1908-1919, PMID: 28494961.

De La Cruz, E.M., and Ostap, E.M. (2004). Relating biochemistry and function in the myosin superfamily. Curr Opin Cell Biol *16*, 61-67, PMID: 15037306.

References

Deitsch, K.W., and Wellems, T.E. (1996). Membrane modifications in erythrocytes parasitized by Plasmodium falciparum. Mol Biochem Parasitol *76*, 1-10, PMID: 8919990.

Di Cristina, M., Spaccapelo, R., Soldati, D., Bistoni, F., and Crisanti, A. (2000). Two conserved amino acid motifs mediate protein targeting to the micronemes of the apicomplexan parasite Toxoplasma gondii. Mol Cell Biol *20*, 7332-7341, PMID: 10982850.

Dobrowolski, J.M., Niesman, I.R., and Sibley, L.D. (1997). Actin in the parasite Toxoplasma gondii is encoded by a single copy gene, ACT1 and exists primarily in a globular form. Cell Motil Cytoskeleton *37*, 253-262, PMID: 9227855.

Dobrowolski, J.M., and Sibley, L.D. (1996). Toxoplasma invasion of mammalian cells is powered by the actin cytoskeleton of the parasite. Cell *84*, 933-939, PMID: 8601316.

Dondorp, A.M., Ince, C., Charunwatthana, P., Hanson, J., van Kuijen, A., Faiz, M.A., Rahman, M.R., Hasan, M., Bin Yunus, E., Ghose, A*., et al.* (2008). Direct in vivo assessment of microcirculatory dysfunction in severe falciparum malaria. J Infect Dis *197*, 79-84, PMID: 18171289.

Dondorp, A.M., Pongponratn, E., and White, N.J. (2004). Reduced microcirculatory flow in severe falciparum malaria: pathophysiology and electron-microscopic pathology. Acta Trop *89*, 309-317, PMID: 14744557.

Douglas, R.G., Amino, R., Sinnis, P., and Frischknecht, F. (2015). Active migration and passive transport of malaria parasites. Trends Parasitol *31*, 357-362, PMID: 26001482.

Dufrene, Y.F., Ando, T., Garcia, R., Alsteens, D., Martinez-Martin, D., Engel, A., Gerber, C., and Muller, D.J. (2017). Imaging modes of atomic force microscopy for application in molecular and cell biology. Nat Nanotechnol *12*, 295-307, PMID: 28383040.

Dzbenski, T.H., Michalak, T., and Plonka, W.S. (1976). Electron-Microscopic and Radioisotopic Studies on Cap Formation in Toxoplasma-Gondii. Infection and Immunity *14*, 1196-1201, PMID: 789242.

Egarter, S., Andenmatten, N., Jackson, A.J., Whitelaw, J.A., Pall, G., Black, J.A., Ferguson, D.J., Tardieux, I., Mogilner, A., and Meissner, M. (2014). The toxoplasma Acto-MyoA motor complex is important but not essential for gliding motility and host cell invasion. PLoS One *9*, e91819, PMID: 24632839.

Ejigiri, I., Ragheb, D.R., Pino, P., Coppi, A., Bennett, B.L., Soldati-Favre, D., and Sinnis, P. (2012). Shedding of TRAP by a rhomboid protease from the malaria sporozoite surface is essential for gliding motility and sporozoite infectivity. PLoS Pathog *8*, e1002725, PMID: 22911675.

Fairhurst, R.M., Baruch, D.I., Brittain, N.J., Ostera, G.R., Wallach, J.S., Hoang, H.L., Hayton, K., Guindo, A., Makobongo, M.O., Schwartz, O.M*., et al.* (2005). Abnormal display of PfEMP-1 on erythrocytes carrying haemoglobin C may protect against malaria. Nature *435*, 1117-1121, PMID: 15973412.

Fairhurst, R.M., Bess, C.D., and Krause, M.A. (2012). Abnormal PfEMP1/knob display on Plasmodium falciparum-infected erythrocytes containing hemoglobin variants: fresh insights into malaria pathogenesis and protection. Microbes Infect *14*, 851-862, PMID: 22634344.

Fairhurst, R.M., Fujioka, H., Hayton, K., Collins, K.F., and Wellems, T.E. (2003). Aberrant development of Plasmodium falciparum in hemoglobin CC red cells: implications for the malaria protective effect of the homozygous state. Blood *101*, 3309-3315, PMID: 12480691.

References

Finer, J.T., Simmons, R.M., and Spudich, J.A. (1994). Single myosin molecule mechanics: piconewton forces and nanometre steps. Nature *368*, 113-119, PMID: 8139653.

Florin, E.L., Moy, V.T., and Gaub, H.E. (1994). Adhesion forces between individual ligand-receptor pairs. Science *264*, 415-417, PMID: 8153628.

Forscher, P., Lin, C.H., and Thompson, C. (1992). Novel Form of Growth Cone Motility Involving Site-Directed Actin Filament Assembly. Nature *357*, 515-518, PMID: 1608453.

Forscher, P., and Smith, S.J. (1988). Actions of cytochalasins on the organization of actin filaments and microtubules in a neuronal growth cone. J Cell Biol *107*, 1505-1516, PMID: 3170637.

Fournier, M.F., Sauser, R., Ambrosi, D., Meister, J.J., and Verkhovsky, A.B. (2010). Force transmission in migrating cells. J Cell Biol *188*, 287-297, PMID: 20100912.

Frenal, K., Polonais, V., Marq, J.B., Stratmann, R., Limenitakis, J., and Soldati-Favre, D. (2010). Functional dissection of the apicomplexan glideosome molecular architecture. Cell Host Microbe *8*, 343-357, PMID: 20951968.

Frevert, U., Engelmann, S., Zougbede, S., Stange, J., Ng, B., Matuschewski, K., Liebes, L., and Yee, H. (2005). Intravital observation of Plasmodium berghei sporozoite infection of the liver. PLoS Biol *3*, e192, PMID: 15901208.

Fried, M., and Duffy, P.E. (1996). Adherence of Plasmodium falciparum to chondroitin sulfate A in the human placenta. Science *272*, 1502-1504, PMID: 8633247.

Friedl, P. (2004). Prespecification and plasticity: shifting mechanisms of cell migration. Curr Opin Cell Biol *16*, 14-23, PMID: 15037300.

Frischknecht, F., Baldacci, P., Martin, B., Zimmer, C., Thiberge, S., Olivo-Marin, J.C., Shorte, S.L., and Menard, R. (2004). Imaging movement of malaria parasites during transmission by Anopheles mosquitoes. Cell Microbiol *6*, 687-694, PMID: 15186404.

Frischknecht, F., Martin, B., Thiery, I., Bourgouin, C., and Menard, R. (2006). Using green fluorescent malaria parasites to screen for permissive vector mosquitoes. Malar J *5*, 23, PMID: 16569221.

Galbraith, C.G., and Sheetz, M.P. (1999). Keratocytes pull with similar forces on their dorsal and ventral surfaces. J Cell Biol *147*, 1313-1324, PMID: 10601343.

Ganter, M., Schuler, H., and Matuschewski, K. (2009). Vital role for the Plasmodium actin capping protein (CP) beta-subunit in motility of malaria sporozoites. Mol Microbiol *74*, 1356-1367, PMID: 19682250.

Gardel, M.L., Sabass, B., Ji, L., Danuser, G., Schwarz, U.S., and Waterman, C.M. (2008). Traction stress in focal adhesions correlates biphasically with actin retrograde flow speed. Journal of Cell Biology *183*, 999-1005, PMID: 19075110.

Ghumra, A., Semblat, J.P., Ataide, R., Kifude, C., Adams, Y., Claessens, A., Anong, D.N., Bull, P.C., Fennell, C., Arman, M.*, et al.* (2012). Induction of strain-transcending antibodies against Group A PfEMP1 surface antigens from virulent malaria parasites. PLoS Pathog *8*, e1002665, PMID: 22532802.

References

Glenister, F.K., Coppel, R.L., Cowman, A.F., Mohandas, N., and Cooke, B.M. (2002). Contribution of parasite proteins to altered mechanical properties of malaria-infected red blood cells. Blood *99*, 1060-1063, PMID: 11807013.

Gordon, J.L., and Sibley, L.D. (2005). Comparative genome analysis reveals a conserved family of actin-like proteins in apicomplexan parasites. BMC Genomics *6*, 179, PMID: 16343347.

Green, J.L., Wall, R.J., Vahokoski, J., Yusuf, N.A., Ridzuan, M.A.M., Stanway, R.R., Stock, J., Knuepfer, E., Brady, D., Martin, S.R.*, et al.* (2017). Compositional and expression analyses of the glideosome during the Plasmodium life cycle reveal an additional myosin light chain required for maximum motility. J Biol Chem, PMID: 28893907.

Grier, D.G. (2003). A revolution in optical manipulation. Nature *424*, 810-816, PMID: 12917694.

Gruenberg, J., Allred, D.R., and Sherman, I.W. (1983). Scanning electron microscope-analysis of the protrusions (knobs) present on the surface of Plasmodium falciparum-infected erythrocytes. J Cell Biol *97*, 795-802, PMID: 6350320.

Guizetti, J., and Scherf, A. (2013). Silence, activate, poise and switch! Mechanisms of antigenic variation in Plasmodium falciparum. Cell Microbiol *15*, 718-726, PMID: 23351305.

Guttery, D.S., Roques, M., Holder, A.A., and Tewari, R. (2015). Commit and Transmit: Molecular Players in Plasmodium Sexual Development and Zygote Differentiation. Trends Parasitol *31*, 676-685, PMID: 26440790.

Haldar, K., Murphy, S.C., Milner, D.A., and Taylor, T.E. (2007). Malaria: Mechanisms of erythrocytic infection and pathological correlates of severe disease. Annu Rev Pathol-Mech *2*, 217-249, PMID: 18039099.

Hall, N., Karras, M., Raine, J.D., Carlton, J.M., Kooij, T.W., Berriman, M., Florens, L., Janssen, C.S., Pain, A., Christophides, G.K.*, et al.* (2005). A comprehensive survey of the Plasmodium life cycle by genomic, transcriptomic, and proteomic analyses. Science *307*, 82-86, PMID: 15637271.

Harlepp, S., Thalmann, F., Follain, G., and Goetz, J.G. (2017). Hemodynamic forces can be accurately measured in vivo with optical tweezers. Mol Biol Cell *28*, 3252-3260, PMID: 28904205.

Harris, A., and Dunn, G. (1972). Centripetal transport of attached particles on both surfaces of moving fibroblasts. Exp Cell Res *73*, 519-523, PMID: 4559927.

Hashemi Shabestari, M., Meijering, A.E.C., Roos, W.H., Wuite, G.J.L., and Peterman, E.J.G. (2017). Chapter Four - Recent Advances in Biological Single-Molecule Applications of Optical Tweezers and Fluorescence Microscopy. In Methods in Enzymology, M. Spies, and Y.R. Chemla, eds. (Academic Press), pp. 85-119, DOI: doi.org/10.1016/bs.mie.2016.09.047.

Heaslip, A.T., Leung, J.M., Carey, K.L., Catti, F., Warshaw, D.M., Westwood, N.J., Ballif, B.A., and Ward, G.E. (2010). A small-molecule inhibitor of T. gondii motility induces the posttranslational modification of myosin light chain-1 and inhibits myosin motor activity. PLoS Pathog *6*, e1000720, PMID: 20084115.

Hegge, S., Kudryashev, M., Smith, A., and Frischknecht, F. (2009). Automated classification of Plasmodium sporozoite movement patterns reveals a shift towards productive motility during salivary gland infection. Biotechnol J *4*, 903-913, PMID: 19455538.

References

Hegge, S., Munter, S., Steinbuchel, M., Heiss, K., Engel, U., Matuschewski, K., and Frischknecht, F. (2010). Multistep adhesion of Plasmodium sporozoites. FASEB J *24*, 2222-2234, PMID: 20159960.

Hegge, S., Uhrig, K., Streichfuss, M., Kynast-Wolf, G., Matuschewski, K., Spatz, J.P., and Frischknecht, F. (2012). Direct manipulation of malaria parasites with optical tweezers reveals distinct functions of Plasmodium surface proteins. ACS Nano *6*, 4648-4662, PMID: 22568891.

Heiss, K., Nie, H., Kumar, S., Daly, T.M., Bergman, L.W., and Matuschewski, K. (2008). Functional characterization of a redundant Plasmodium TRAP family invasin, TRAP-like protein, by aldolase binding and a genetic complementation test. Eukaryot Cell *7*, 1062-1070, PMID: 18441124.

Hellmann, J.K., Munter, S., Kudryashev, M., Schulz, S., Heiss, K., Muller, A.K., Matuschewski, K., Spatz, J.P., Schwarz, U.S., and Frischknecht, F. (2011). Environmental constraints guide migration of malaria parasites during transmission. PLoS Pathog *7*, e1002080, PMID: 21698220.

Hellmann, J.K., Perschmann, N., Spatz, J.P., and Frischknecht, F. (2013). Tunable substrates unveil chemical complementation of a genetic cell migration defect. Adv Healthc Mater *2*, 1162-1169, PMID: 23355513.

Helms, G., Dasanna, A.K., Schwarz, U.S., and Lanzer, M. (2016). Modeling cytoadhesion of Plasmodium falciparum-infected erythrocytes and leukocytes-common principles and distinctive features. FEBS Lett *590*, 1955-1971, PMID: 26992823.

Herm-Gotz, A., Weiss, S., Stratmann, R., Fujita-Becker, S., Ruff, C., Meyhofer, E., Soldati, T., Manstein, D.J., Geeves, M.A., and Soldati, D. (2002). Toxoplasma gondii myosin A and its light chain: a fast, single-headed, plus-end-directed motor. EMBO J *21*, 2149-2158, PMID: 11980712.

Hliscs, M., Sattler, J.M., Tempel, W., Artz, J.D., Dong, A.P., Hui, R., Matuschewski, K., and Schuler, H. (2010). Structure and Function of a G-actin Sequestering Protein with a Vital Role in Malaria Oocyst Development inside the Mosquito Vector. Journal of Biological Chemistry *285*, 11572-11583, PMID: 20083609.

Homsher, E., Nili, M., Chen, I.Y., and Tobacman, L.S. (2003). Regulatory proteins alter nucleotide binding to acto-myosin of sliding filaments in motility assays. Biophys J *85*, 1046-1052, PMID: 12885651.

Homsher, E., Wang, F., and Sellers, J.R. (1992). Factors affecting movement of F-actin filaments propelled by skeletal muscle heavy meromyosin. Am J Physiol *262*, C714-723, PMID: 1550212.

Hopp, C.S., Chiou, K., Ragheb, D.R., Salman, A., Khan, S.M., Liu, A.J., and Sinnis, P. (2015). Longitudinal analysis of Plasmodium sporozoite motility in the dermis reveals component of blood vessel recognition. Elife *4*, PMID: 26271010.

Horrocks, P., Pinches, R.A., Chakravorty, S.J., Papakrivos, J., Christodoulou, Z., Kyes, S.A., Urban, B.C., Ferguson, D.J.P., and Newbold, C.I. (2005). PfEMP1 expression is reduced on the surface of knobless Plasmodium falciparum infected erythrocytes. Journal of Cell Science *118*, 2507-2518, PMID: 15923663

Hu, K., Ji, L., Applegate, K.T., Danuser, G., and Waterman-Storer, C.M. (2007). Differential transmission of actin motion within focal adhesions. Science *315*, 111-115, PMID: 17204653.

Hynes, R.O. (2002). Integrins: bidirectional, allosteric signaling machines. Cell *110*, 673-687, PMID: 12297042.

References

Ishino, T., Chinzei, Y., and Yuda, M. (2005). Two proteins with 6-cys motifs are required for malarial parasites to commit to infection of the hepatocyte. Mol Microbiol *58*, 1264-1275, PMID: 16313615.

Ishino, T., Yano, K., Chinzei, Y., and Yuda, M. (2004). Cell-passage activity is required for the malarial parasite to cross the liver sinusoidal cell layer. Plos Biology *2*, 77-84, PMID: 14737184.

Jacot, D., Tosetti, N., Pires, I., Stock, J., Graindorge, A., Hung, Y.F., Han, H., Tewari, R., Kursula, I., and Soldati-Favre, D. (2016). An Apicomplexan Actin-Binding Protein Serves as a Connector and Lipid Sensor to Coordinate Motility and Invasion. Cell Host Microbe *20*, 731-743, PMID: 27978434.

Janse, C.J., Kroeze, H., van Wigcheren, A., Mededovic, S., Fonager, J., Franke-Fayard, B., Waters, A.P., and Khan, S.M. (2011). A genotype and phenotype database of genetically modified malaria-parasites. Trends Parasitol *27*, 31-39, PMID: 20663715.

Janse, C.J., Ramesar, J., and Waters, A.P. (2006). High-efficiency transfection and drug selection of genetically transformed blood stages of the rodent malaria parasite Plasmodium berghei. Nat Protoc *1*, 346-356, PMID: 17406255.

Jewett, T.J., and Sibley, L.D. (2003). Aldolase forms a bridge between cell surface adhesins and the actin cytoskeleton in apicomplexan parasites. Mol Cell *11*, 885-894, PMID: 12718875.

Johnson, T.M., Rajfur, Z., Jacobson, K., and Beckers, C.J. (2007). Immobilization of the type XIV myosin complex in Toxoplasma gondii. Mol Biol Cell *18*, 3039-3046, PMID: 17538016.

Jones, M.L., Collins, M.O., Goulding, D., Choudhary, J.S., and Rayner, J.C. (2012). Analysis of protein palmitoylation reveals a pervasive role in Plasmodium development and pathogenesis. Cell Host Microbe *12*, 246-258, PMID: 22901544.

Jurado, C., Haserick, J.R., and Lee, J. (2005). Slipping or gripping? Fluorescent speckle microscopy in fish keratocytes reveals two different mechanisms for generating a retrograde flow of actin. Mol Biol Cell *16*, 507-518, PMID: 15548591.

Kantele, A., and Jokiranta, T.S. (2011). Review of cases with the emerging fifth human malaria parasite, Plasmodium knowlesi. Clin Infect Dis *52*, 1356-1362, PMID: 21596677.

Kapishnikov, S., Grolimund, D., Schneider, G., Pereiro, E., McNally, J.G., Als-Nielsen, J., and Leiserowitz, L. (2017). Unraveling heme detoxification in the malaria parasite by in situ correlative X-ray fluorescence microscopy and soft X-ray tomography. Sci Rep *7*, 7610, PMID: 28790371.

Kappe, S., Bruderer, T., Gantt, S., Fujioka, H., Nussenzweig, V., and Menard, R. (1999). Conservation of a gliding motility and cell invasion machinery in Apicomplexan parasites. J Cell Biol *147*, 937-944, PMID: 10579715.

Kariu, T., Ishino, T., Yano, K., Chinzei, Y., and Yuda, M. (2006). CelTOS, a novel malarial protein that mediates transmission to mosquito and vertebrate hosts. Mol Microbiol *59*, 1369-1379, PMID: 16468982.

Kaushansky, A., Douglass, A.N., Arang, N., Vigdorovich, V., Dambrauskas, N., Kain, H.S., Austin, L.S., Sather, D.N., and Kappe, S.H. (2015). Malaria parasites target the hepatocyte receptor EphA2 for successful host infection. Science *350*, 1089-1092, PMID: 26612952.

Kehrer, J., Frischknecht, F., and Mair, G.R. (2016a). Proteomic Analysis of the Plasmodium berghei Gametocyte Egressome and Vesicular bioID of Osmiophilic Body Proteins Identifies Merozoite TRAP-

References

like Protein (MTRAP) as an Essential Factor for Parasite Transmission. Mol Cell Proteomics *15*, 2852-2862, PMID: 27371728.

Kehrer, J., Singer, M., Lemgruber, L., Silva, P.A., Frischknecht, F., and Mair, G.R. (2016b). A Putative Small Solute Transporter Is Responsible for the Secretion of G377 and TRAP-Containing Secretory Vesicles during Plasmodium Gamete Egress and Sporozoite Motility. PLoS Pathog *12*, e1005734, PMID: 27427910.

Khater, E.I., Sinden, R.E., and Dessens, J.T. (2004). A malaria membrane skeletal protein is essential for normal morphogenesis, motility and infectivity of sporozoites. Journal of Cell Biology *167*, 425-432, PMID: 15533999.

King, C.A. (1981). Cell surface interaction of the protozoan Gregarina with concanavalin A beads - implications for models of gregarine gliding. Cell Biol Int Rep *5*, 297-305, PMID: 6783325.

Klug, D., and Frischknecht, F. (2017). Motility precedes egress of malaria parasites from oocysts. Elife *6*, PMID: 28115054.

Kraemer, S.M., and Smith, J.D. (2006). A family affair: var genes, PfEMP1 binding, and malaria disease. Curr Opin Microbiol *9*, 374-380, PMID: 16814594.

Krugliak, M., Zhang, J., and Ginsburg, H. (2002). Intraerythrocytic Plasmodium falciparum utilizes only a fraction of the amino acids derived from the digestion of host cell cytosol for the biosynthesis of its proteins. Mol Biochem Parasitol *119*, 249-256, PMID: 11814576.

Kudryashev, M., Lepper, S., Baumeister, W., Cyrklaff, M., and Frischknecht, F. (2010a). Geometric constrains for detecting short actin filaments by cryogenic electron tomography. PMC Biophys *3*, 6, PMID: 20214767.

Kudryashev, M., Lepper, S., Stanway, R., Bohn, S., Baumeister, W., Cyrklaff, M., and Frischknecht, F. (2010b). Positioning of large organelles by a membrane- associated cytoskeleton in Plasmodium sporozoites. Cell Microbiol *12*, 362-371, PMID: 19863555.

Kudryashev, M., Munter, S., Lemgruber, L., Montagna, G., Stahlberg, H., Matuschewski, K., Meissner, M., Cyrklaff, M., and Frischknecht, F. (2012). Structural basis for chirality and directional motility of Plasmodium sporozoites. Cell Microbiol *14*, 1757-1768, PMID: 22776715.

Kyes, S., Horrocks, P., and Newbold, C. (2001). Antigenic variation at the infected red cell surface in malaria. Annu Rev Microbiol *55*, 673-707, PMID: 11544371.

Labaied, M., Harupa, A., Dumpit, R.F., Coppens, I., Mikolajczak, S.A., and Kappe, S.H. (2007). Plasmodium yoelii sporozoites with simultaneous deletion of P52 and P36 are completely attenuated and confer sterile immunity against infection. Infect Immun *75*, 3758-3768, PMID: 17517871.

Lammermann, T., Afonso, P.V., Angermann, B.R., Wang, J.M., Kastenmuller, W., Parent, C.A., and Germain, R.N. (2013). Neutrophil swarms require LTB4 and integrins at sites of cell death in vivo. Nature *498*, 371-375, PMID: 23708969.

Langreth, S.G., Jensen, J.B., Reese, R.T., and Trager, W. (1978). Fine structure of human malaria in vitro. J Protozool *25*, 443-452, PMID: 105129.

References

Li, A., Mansoor, A.H., Tan, K.S.W., and Lim, C.T. (2006). Observations on the internal and surface morphology of malaria infected blood cells using optical and atomic force microscope. J Microbiol Meth *66*, 434-439, PMID: 16519955

Lin, C.H., Espreafico, E.M., Mooseker, M.S., and Forscher, P. (1996). Myosin drives retrograde F-actin flow in neuronal growth cones. Neuron *16*, 769-782, PMID: 8607995.

Lin, C.H., and Forscher, P. (1995). Growth Cone Advance Is Inversely Proportional to Retrograde F-Actin Flow. Neuron *14*, 763-771, PMID: 7536426.

Lin, J.W., Annoura, T., Sajid, M., Chevalley-Maurel, S., Ramesar, J., Klop, O., Franke-Fayard, B.M., Janse, C.J., and Khan, S.M. (2011). A novel 'gene insertion/marker out' (GIMO) method for transgene expression and gene complementation in rodent malaria parasites. PLoS One *6*, e29289, PMID: 22216235.

Lindner, S.E., Swearingen, K.E., Harupa, A., Vaughan, A.M., Sinnis, P., Moritz, R.L., and Kappe, S.H. (2013). Total and putative surface proteomics of malaria parasite salivary gland sporozoites. Mol Cell Proteomics *12*, 1127-1143, PMID: 23325771.

Lodish, H.F. (2000). Molecular cell biology, 4th edn (New York: W.H. Freeman).

Mackenstedt, U., Brockelman, C.R., Mehlhorn, H., and Raether, W. (1989). Comparative morphology of human and animal malaria parasites. I. Host-parasite interface. Parasitol Res *75*, 528-535, PMID: 2671984.

Maier, A.G., Rug, M., O'Neill, M.T., Brown, M., Chakravorty, S., Szestak, T., Chesson, J., Wu, Y., Hughes, K., Coppel, R.L.*, et al.* (2008). Exported proteins required for virulence and rigidity of Plasmodium falciparum-infected human erythrocytes. Cell *134*, 48-61, PMID: 18614010.

Makkonen, M., Bertling, E., Chebotareva, N.A., Baum, J., and Lappalainen, P. (2013). Mammalian and Malaria Parasite Cyclase-associated Proteins Catalyze Nucleotide Exchange on G-actin through a Conserved Mechanism. Journal of Biological Chemistry *288*, 984-994, PMID: 23184938

Marti, M., Baum, J., Rug, M., Tilley, L., and Cowman, A.F. (2005). Signal-mediated export of proteins from the malaria parasite to the host erythrocyte. J Cell Biol *171*, 587-592, PMID: 16301328.

Mastan, B.S., Narwal, S.K., Dey, S., Kumar, K.A., and Mishra, S. (2017). Plasmodium berghei plasmepsin VIII is essential for sporozoite gliding motility. Int J Parasitol *47*, 239-245, PMID: 28192122.

Matuschewski, K., Nunes, A.C., Nussenzweig, V., and Menard, R. (2002). Plasmodium sporozoite invasion into insect and mammalian cells is directed by the same dual binding system. EMBO J *21*, 1597-1606, PMID: 11927544.

McCormick, C.J., Craig, A., Roberts, D., Newbold, C.I., and Berendt, A.R. (1997). Intercellular adhesion molecule-1 and CD36 synergize to mediate adherence of Plasmodium falciparum-infected erythrocytes to cultured human microvascular endothelial cells. J Clin Invest *100*, 2521-2529, PMID: 9366566.

McFadden, G.I. (2011). The apicoplast. Protoplasma *248*, 641-650, PMID: 21165662.

Mebius, R.E., and Kraal, G. (2005). Structure and function of the spleen. Nat Rev Immunol *5*, 606-616, PMID: 16056254.

References

Mehta, A.D., Rock, R.S., Rief, M., Spudich, J.A., Mooseker, M.S., and Cheney, R.E. (1999). Myosin-V is a processive actin-based motor. Nature *400*, 590-593, PMID: 10448864.

Meibalan, E., and Marti, M. (2016). Biology of Malaria Transmission. Cold Spring Harb Perspect Med, PMID: 27836912.

Meissner, M., Schluter, D., and Soldati, D. (2002). Role of Toxoplasma gondii myosin A in powering parasite gliding and host cell invasion. Science *298*, 837-840, PMID: 12399593.

Melak, M., Plessner, M., and Grosse, R. (2017). Actin visualization at a glance. J Cell Sci *130*, 525-530, PMID: 28082420.

Mikolajczak, S.A., Silva-Rivera, H., Peng, X., Tarun, A.S., Camargo, N., Jacobs-Lorena, V., Daly, T.M., Bergman, L.W., de la Vega, P., Williams, J.*, et al.* (2008). Distinct malaria parasite sporozoites reveal transcriptional changes that cause differential tissue infection competence in the mosquito vector and mammalian host. Mol Cell Biol *28*, 6196-6207, PMID: 18710954.

Miller, L.H., Baruch, D.I., Marsh, K., and Doumbo, O.K. (2002). The pathogenic basis of malaria. Nature *415*, 673-679, PMID: 11832955.

Millholland, M.G., Chandramohanadas, R., Pizzarro, A., Wehr, A., Shi, H., Darling, C., Lim, C.T., and Greenbaum, D.C. (2011). The malaria parasite progressively dismantles the host erythrocyte cytoskeleton for efficient egress. Mol Cell Proteomics *10*, M111 010678, PMID: 21903871.

Mishra, S., Nussenzweig, R.S., and Nussenzweig, V. (2012). Antibodies to Plasmodium circumsporozoite protein (CSP) inhibit sporozoite's cell traversal activity. J Immunol Methods *377*, 47-52, PMID: 22306356.

Mitchison, T., and Kirschner, M. (1988). Cytoskeletal dynamics and nerve growth. Neuron *1*, 761-772, PMID: 3078414.

Moller, C., Allen, M., Elings, V., Engel, A., and Muller, D.J. (1999). Tapping-mode atomic force microscopy produces faithful high-resolution images of protein surfaces. Biophys J *77*, 1150-1158, PMID: 10423460.

Molloy, J.E., Burns, J.E., Kendrick-Jones, J., Tregear, R.T., and White, D.C. (1995). Movement and force produced by a single myosin head. Nature *378*, 209-212, PMID: 7477328.

Montagna, G.N., Matuschewski, K., and Buscaglia, C.A. (2012). Plasmodium sporozoite motility: an update. Front Biosci (Landmark Ed) *17*, 726-744, PMID: 22201771.

Morahan, B.J., Wang, L., and Coppel, R.L. (2009). No TRAP, no invasion. Trends Parasitol *25*, 77-84, PMID: 19101208.

Moreau, C.A., Bhargav, S.P., Kumar, H., Quadt, K.A., Piirainen, H., Strauss, L., Kehrer, J., Streichfuss, M., Spatz, J.P., Wade, R.C.*, et al.* (2017). A unique profilin-actin interface is important for malaria parasite motility. PLoS Pathog *13*, e1006412, PMID: 28552953.

Moreira, C.K., Templeton, T.J., Lavazec, C., Hayward, R.E., Hobbs, C.V., Kroeze, H., Janse, C.J., Waters, A.P., Sinnis, P., and Coppi, A. (2008). The Plasmodium TRAP/MIC2 family member, TRAP-Like Protein (TLP), is involved in tissue traversal by sporozoites. Cell Microbiol *10*, 1505-1516, PMID: 18346224.

References

Mota, M.M., Pradel, G., Vanderberg, J.P., Hafalla, J.C.R., Frevert, U., Nussenzweig, R.S., Nussenzweig, V., and Rodriguez, A. (2001). Migration of Plasmodium sporozoites through cells before infection. Science *291*, 141-144, PMID: 12379848.

Mueller, A.K., Camargo, N., Kaiser, K., Andorfer, C., Frevert, U., Matuschewski, K., and Kappe, S.H. (2005a). Plasmodium liver stage developmental arrest by depletion of a protein at the parasite-host interface. Proc Natl Acad Sci U S A *102*, 3022-3027, PMID: 15699336.

Mueller, A.K., Labaied, M., Kappe, S.H.I., and Matuschewski, K. (2005b). Genetically modified Plasmodium parasites as a protective experimental malaria vaccine. Nature *433*, 164-167, PMID: 15580261.

Munter, S., Sabass, B., Selhuber-Unkel, C., Kudryashev, M., Hegge, S., Engel, U., Spatz, J.P., Matuschewski, K., Schwarz, U.S., and Frischknecht, F. (2009). Plasmodium sporozoite motility is modulated by the turnover of discrete adhesion sites. Cell Host Microbe *6*, 551-562, PMID: 20006843.

Muthinja, M.J., Ripp, J., Hellmann, J.K., Haraszti, T., Dahan, N., Lemgruber, L., Battista, A., Schutz, L., Fackler, O.T., Schwarz, U.S.*, et al.* (2017). Microstructured Blood Vessel Surrogates Reveal Structural Tropism of Motile Malaria Parasites. Adv Healthc Mater, PMID: 28117558.

Nagao, E., Kaneko, O., and Dvorak, J.A. (2000). Plasmodium falciparum-infected erythrocytes: qualitative and quantitative analyses of parasite-induced knobs by atomic force microscopy. J Struct Biol *130*, 34-44, PMID: 10806089.

Nambiar, R., McConnell, R.E., and Tyska, M.J. (2010). Myosin motor function: the ins and outs of actin-based membrane protrusions. Cell Mol Life Sci *67*, 1239-1254, PMID: 20107861.

Natarajan, R., Thathy, V., Mota, M.M., Hafalla, J.C., Menard, R., and Vernick, K.D. (2001). Fluorescent Plasmodium berghei sporozoites and pre-erythrocytic stages: a new tool to study mosquito and mammalian host interactions with malaria parasites. Cell Microbiol *3*, 371-379, PMID: 11422080.

Oberli, A., Slater, L.M., Cutts, E., Brand, F., Mundwiler-Pachlatko, E., Rusch, S., Masik, M.F.G., Erat, M.C., Beck, H.P., and Vakonakis, I. (2014). A Plasmodium falciparum PHIST protein binds the virulence factor PfEMP1 and comigrates to knobs on the host cell surface. Faseb Journal *28*, 4420-4433, PMID: 24983468.

Oh, S.S., Voigt, S., Fisher, D., Yi, S.J., LeRoy, P.J., Derick, L.H., Liu, S., and Chishti, A.H. (2000). Plasmodium falciparum erythrocyte membrane protein 1 is anchored to the actin-spectrin junction and knob-associated histidine-rich protein in the erythrocyte skeleton. Mol Biochem Parasitol *108*, 237-247, PMID: 10838226.

Olshina, M.A., Angrisano, F., Marapana, D.S., Riglar, D.T., Bane, K., Wong, W., Catimel, B., Yin, M.X., Holmes, A.B., Frischknecht, F.*, et al.* (2015). Plasmodium falciparum coronin organizes arrays of parallel actin filaments potentially guiding directional motility in invasive malaria parasites. Malar J *14*, 280, PMID: 26187846.

Olshina, M.A., Baumann, H., Willison, K.R., and Baum, J. (2016). Plasmodium actin is incompletely folded by heterologous protein-folding machinery and likely requires the native Plasmodium chaperonin complex to enter a mature functional state. FASEB J *30*, 405-416, PMID: 26443825.

Otto, T.D., Bohme, U., Jackson, A.P., Hunt, M., Franke-Fayard, B., Hoeijmakers, W.A., Religa, A.A., Robertson, L., Sanders, M., Ogun, S.A.*, et al.* (2014). A comprehensive evaluation of rodent malaria parasite genomes and gene expression. BMC Biol *12*, 86, PMID: 25359557.

References

Periz, J., Whitelaw, J., Harding, C., Gras, S., Del Rosario Minina, M.I., Latorre-Barragan, F., Lemgruber, L., Reimer, M.A., Insall, R., Heaslip, A.*, et al.* (2017). Toxoplasma gondii F-actin forms an extensive filamentous network required for material exchange and parasite maturation. Elife *6*, PMID: 28322189.

Pierini, F., Zembrzycki, K., Nakielski, P., Pawlowska, S., and Kowalewski, T.A. (2016). Atomic force microscopy combined with optical tweezers (AFM/OT). Meas Sci Technol *27*, DOI: doi.org/10.1088/0957-0233/27/2/025904.

Pimenta, P.F., Touray, M., and Miller, L. (1994). The journey of malaria sporozoites in the mosquito salivary gland. J Eukaryot Microbiol *41*, 608-624, PMID: 7866385.

Planche, T., and Krishna, S. (2006). Severe malaria: Metabolic complications. Curr Mol Med *6*, 141-153, PMID: 16515507.

Pollard, T.D., Blanchoin, L., and Mullins, R.D. (2000). Molecular mechanisms controlling actin filament dynamics in nonmuscle cells. Annu Rev Biophys Biomol Struct *29*, 545-576, PMID: 10940259.

Pologe, L.G., Pavlovec, A., Shio, H., and Ravetch, J.V. (1987). Primary structure and subcellular localization of the knob-associated histidine-rich protein of Plasmodium falciparum. Proc Natl Acad Sci U S A *84*, 7139-7143, PMID: 3313387.

Ponti, A., Machacek, M., Gupton, S.L., Waterman-Storer, C.M., and Danuser, G. (2004). Two distinct actin networks drive the protrusion of migrating cells. Science *305*, 1782-1786, PMID: 15375270.

Poupel, O., and Tardieux, I. (1999). Toxoplasma gondii motility and host cell invasiveness are drastically impaired by jasplakinolide, a cyclic peptide stabilizing F-actin. Microbes Infect *1*, 653-662, PMID: 10611742.

Pradel, G., and Frevert, U. (2001). Malaria sporozoites actively enter and pass through rat Kupffer cells prior to hepatocyte invasion. Hepatology *33*, 1154-1165, PMID: 11343244.

Prudencio, M., Rodriguez, A., and Mota, M.M. (2006). The silent path to thousands of merozoites: the Plasmodium liver stage. Nature Reviews Microbiology *4*, 849-856, PMID: 17041632.

Przyborski, J.M., Wickert, H., Krohne, G., and Lanzer, M. (2003). Maurer's clefts--a novel secretory organelle? Mol Biochem Parasitol *132*, 17-26, PMID: 14563533.

Quadt, K.A., Barfod, L., Andersen, D., Bruun, J., Gyan, B., Hassenkam, T., Ofori, M.F., and Hviid, L. (2012). The Density of Knobs on Plasmodium falciparum-Infected Erythrocytes Depends on Developmental Age and Varies among Isolates. Plos One *7*, PMID: 23029166

Rao, V.S., Marongelli, E.N., and Guilford, W.H. (2009). Phosphorylation of Tropomyosin Extends Cooperative Binding of Myosin Beyond a Single Regulatory Unit. Cell Motil Cytoskel *66*, 10-23, PMID: 18985725.

Renkawitz, J., and Sixt, M. (2010). Mechanisms of force generation and force transmission during interstitial leukocyte migration. EMBO Rep *11*, 744-750, PMID: 20865016.

Rief, M., Rock, R.S., Mehta, A.D., Mooseker, M.S., Cheney, R.E., and Spudich, J.A. (2000). Myosin-V stepping kinetics: a molecular model for processivity. Proc Natl Acad Sci U S A *97*, 9482-9486, PMID: 10944217.

References

Rieger, H., Yoshikawa, H.Y., Quadt, K., Nielsen, M.A., Sanchez, C.P., Salanti, A., Tanaka, M., and Lanzer, M. (2015). Cytoadhesion of Plasmodium falciparum-infected erythrocytes to chondroitin-4-sulfate is cooperative and shear enhanced. Blood *125*, 383-391, PMID: 25352129.

Rottger, S., Frischknecht, F., Reckmann, I., Smith, G.L., and Way, M. (1999). Interactions between vaccinia virus IEV membrane proteins and their roles in IEV assembly and actin tail formation. J Virol *73*, 2863-2875, PMID: 10074134.

Rowe, J.A., Claessens, A., Corrigan, R.A., and Arman, M. (2009). Adhesion of Plasmodium falciparum-infected erythrocytes to human cells: molecular mechanisms and therapeutic implications. Expert Rev Mol Med *11*, e16, PMID: 19467172.

Russell, D.G. (1983). Host-Cell Invasion by Apicomplexa - an Expression of the Parasites Contractile System. Parasitology *87*, 199-&, PMID: 6646806.

Russell, D.G., and Sinden, R.E. (1981). The role of the cytoskeleton in the motility of coccidian sporozoites. J Cell Sci *50*, 345-359, PMID: 7033252.

Sahoo, N., Beatty, W., Heuser, J., Sept, D., and Sibley, L.D. (2006). Unusual kinetic and structural properties control rapid assembly and turnover of actin in the parasite Toxoplasma gondii. Mol Biol Cell *17*, 895-906, PMID: 16319175.

Salanti, A., Dahlback, M., Turner, L., Nielsen, M.A., Barfod, L., Magistrado, P., Jensen, A.T., Lavstsen, T., Ofori, M.F., Marsh, K.*, et al.* (2004). Evidence for the involvement of VAR2CSA in pregnancy-associated malaria. J Exp Med *200*, 1197-1203, PMID: 15520249.

Sattler, J.M., Ganter, M., Hliscs, M., Matuschewski, K., and Schuler, H. (2011). Actin regulation in the malaria parasite. Eur J Cell Biol *90*, 966-971, PMID: 21256619.

Schewiakoff, W. (1894). Über die Ursache der fortschreitenden Bewegung der Gregarinen. Zeit Wiss Zool *58*, 340-354,

Schindelin, J., Arganda-Carreras, I., Frise, E., Kaynig, V., Longair, M., Pietzsch, T., Preibisch, S., Rueden, C., Saalfeld, S., Schmid, B.*, et al.* (2012). Fiji: an open-source platform for biological-image analysis. Nat Methods *9*, 676-682, PMID: 22743772.

Schmitz, S., Grainger, M., Howell, S., Calder, L.J., Gaeb, M., Pinder, J.C., Holder, A.A., and Veigel, C. (2005). Malaria parasite actin filaments are very short. J Mol Biol *349*, 113-125, PMID: 15876372.

Schmitz, S., Schaap, I.A., Kleinjung, J., Harder, S., Grainger, M., Calder, L., Rosenthal, P.B., Holder, A.A., and Veigel, C. (2010). Malaria parasite actin polymerization and filament structure. J Biol Chem *285*, 36577-36585, PMID: 20826799.

Schofield, L. (2007). Intravascular infiltrates and organ-specific inflammation in malaria pathogenesis. Immunol Cell Biol *85*, 130-137, PMID: 17344907.

Schrevel, J., Asfaux-Foucher, G., Hopkins, J.M., Robert, V., Bourgouin, C., Prensier, G., and Bannister, L.H. (2008). Vesicle trafficking during sporozoite development in Plasmodium berghei: ultrastructural evidence for a novel trafficking mechanism. Parasitology *135*, 1-12, PMID: 17908361.

Schuler, H., and Matuschewski, K. (2006). Regulation of apicomplexan microfilament dynamics by a minimal set of actin-binding proteins. Traffic *7*, 1433-1439, PMID: 17010119.

References

Schuler, H., Mueller, A.K., and Matuschewski, K. (2005a). A Plasmodium actin-depolymerizing factor that binds exclusively to actin monomers. Molecular Biology of the Cell *16*, 4013-4023, PMID: 15975905.

Schuler, H., Mueller, A.K., and Matuschewski, K. (2005b). Unusual properties of Plasmodium falciparum actin: new insights into microfilament dynamics of apicomplexan parasites. FEBS Lett *579*, 655-660, PMID: 15670824.

Schwingel, M., and Bastmeyer, M. (2013). Force mapping during the formation and maturation of cell adhesion sites with multiple optical tweezers. PLoS One *8*, e54850, PMID: 23372781.

Shaw, M.K., and Tilney, L.G. (1999). Induction of an acrosomal process in Toxoplasma gondii: visualization of actin filaments in a protozoan parasite. Proc Natl Acad Sci U S A *96*, 9095-9099, PMID: 10430901.

Shen, B., and Sibley, L.D. (2014). Toxoplasma aldolase is required for metabolism but dispensable for host-cell invasion. Proc Natl Acad Sci U S A *111*, 3567-3572, PMID: 24550496.

Shi, H., Liu, Z., Li, A., Yin, J., Chong, A.G.L., Tan, K.S.W., Zhang, Y., and Lim, C.T. (2013). Life Cycle-Dependent Cytoskeletal Modifications in Plasmodium falciparum Infected Erythrocytes. Plos One *8*, PMID: 23585879

Silvie, O., Briquet, S., Muller, K., Manzoni, G., and Matuschewski, K. (2014). Post-transcriptional silencing of UIS4 in Plasmodium berghei sporozoites is important for host switch. Molecular Microbiology *91*, 1200-1213, PMID: 24446886.

Silvie, O., Franetich, J.F., Charrin, S., Mueller, M.S., Siau, A., Bodescot, M., Rubinstein, E., Hannoun, L., Charoenvit, Y., Kocken, C.H.*, et al.* (2004). A role for apical membrane antigen 1 during invasion of hepatocytes by Plasmodium falciparum sporozoites. J Biol Chem *279*, 9490-9496, PMID: 14676185.

Sinden, R.E. (1983). The Cell Biology of Sexual Development in Plasmodium. Parasitology *86*, 7-+, PMID: 6191269.

Singer, M. (2017). Timed genome editing and sporozoite formation in Plasmodium berghei. In Parasitology - Center for Infectious Diseases (Heidelberg: University of Heidelberg).

Singh, B.K., Sattler, J.M., Chatterjee, M., Huttu, J., Schuler, H., and Kursula, I. (2011). Crystal Structures Explain Functional Differences in the Two Actin Depolymerization Factors of the Malaria Parasite. Journal of Biological Chemistry *286*, 28256-28264, PMID: 21832095.

Skillman, K.M., Daher, W., Ma, C.I., Soldati-Favre, D., and Sibley, L.D. (2012). Toxoplasma gondii profilin acts primarily to sequester G-actin while formins efficiently nucleate actin filament formation in vitro. Biochemistry-Us *51*, 2486-2495, PMID: 22397711.

Skillman, K.M., Diraviyam, K., Khan, A., Tang, K., Sept, D., and Sibley, L.D. (2011). Evolutionarily divergent, unstable filamentous actin is essential for gliding motility in apicomplexan parasites. PLoS Pathog *7*, e1002280, PMID: 21998582.

Smith, J.D., Rowe, J.A., Higgins, M.K., and Lavstsen, T. (2013). Malaria's deadly grip: cytoadhesion of Plasmodium falciparum-infected erythrocytes. Cell Microbiol *15*, 1976-1983, PMID: 23957661.

Song, G.J., Koksal, A.C., Lu, C.F., and Springer, T.A. (2012). Shape change in the receptor for gliding motility in Plasmodium sporozoites. P Natl Acad Sci USA *109*, 21420-21425, PMID: 23236185

References

Stadler, R.V., White, L.A., Hu, K., Helmke, B.P., and Guilford, W.H. (2017). Direct measurement of cortical force generation and polarization in a living parasite. Mol Biol Cell, PMID: 28209732.

Starnes, G.L., Coincon, M., Sygusch, J., and Sibley, L.D. (2009). Aldolase Is Essential for Energy Production and Bridging Adhesin-Actin Cytoskeletal Interactions during Parasite Invasion of Host Cells. Cell Host & Microbe *5*, 353-364, PMID: 19380114.

Steinbuechel, M., and Matuschewski, K. (2009). Role for the Plasmodium sporozoite-specific transmembrane protein S6 in parasite motility and efficient malaria transmission. Cell Microbiol *11*, 279-288, PMID: 19016774.

Stellamanns, E., Uppaluri, S., Hochstetter, A., Heddergott, N., Engstler, M., and Pfohl, T. (2014). Optical trapping reveals propulsion forces, power generation and motility efficiency of the unicellular parasites Trypanosoma brucei brucei. Sci Rep *4*, 6515, PMID: 25269514.

Stewart, M.J., and Vanderberg, J.P. (1991). Malaria sporozoites release circumsporozoite protein from their apical end and translocate it along their surface. J Protozool *38*, 411-421, PMID: 1787427.

Streichfuss, M., Erbs, F., Uhrig, K., Kurre, R., Clemen, A.E., Bohm, C.H., Haraszti, T., and Spatz, J.P. (2011). Measuring forces between two single actin filaments during bundle formation. Nano Lett *11*, 3676-3680, PMID: 21838252.

Sturm, A., Amino, R., van de Sand, C., Regen, T., Retzlaff, S., Rennenberg, A., Krueger, A., Pollok, J.M., Menard, R., and Heussler, V.T. (2006). Manipulation of host hepatocytes by the malaria parasite for delivery into liver sinusoids. Science *313*, 1287-1290, PMID: 16888102.

Suarez-Cortes, P., Sharma, V., Bertuccini, L., Costa, G., Bannerman, N.L., Sannella, A.R., Williamson, K., Klemba, M., Levashina, E.A., Lasonder, E.*, et al.* (2016). Comparative Proteomics and Functional Analysis Reveal a Role of Plasmodium falciparum Osmiophilic Bodies in Malaria Parasite Transmission. Mol Cell Proteomics *15*, 3243-3255, PMID: 27432909.

Subramani, R., Quadt, K., Jeppesen, A.E., Hempel, C., Petersen, J.E.V., Hassenkam, T., Hviid, L., and Barfod, L. (2015). Plasmodium falciparum-Infected Erythrocyte Knob Density Is Linked to the PfEMP1 Variant Expressed. Mbio *6*, PMID: 26443460.

Sultan, A.A., Thathy, V., Frevert, U., Robson, K.J., Crisanti, A., Nussenzweig, V., Nussenzweig, R.S., and Menard, R. (1997). TRAP is necessary for gliding motility and infectivity of plasmodium sporozoites. Cell *90*, 511-522, PMID: 9267031.

Svoboda, K., and Block, S.M. (1994). Force and velocity measured for single kinesin molecules. Cell *77*, 773-784, PMID: 8205624.

Swearingen, K.E., Lindner, S.E., Shi, L., Shears, M.J., Harupa, A., Hopp, C.S., Vaughan, A.M., Springer, T.A., Moritz, R.L., Kappe, S.H.*, et al.* (2016). Interrogating the Plasmodium Sporozoite Surface: Identification of Surface-Exposed Proteins and Demonstration of Glycosylation on CSP and TRAP by Mass Spectrometry-Based Proteomics. PLoS Pathog *12*, e1005606, PMID: 27128092.

Takagi, J., Petre, B.M., Walz, T., and Springer, T.A. (2002). Global conformational rearrangements in integrin extracellular domains in outside-in and inside-out signaling. Cell *110*, 599-511, PMID: 12230977.

References

Talman, A.M., Lacroix, C., Marques, S.R., Blagborough, A.M., Carzaniga, R., Menard, R., and Sinden, R.E. (2011). PbGEST mediates malaria transmission to both mosquito and vertebrate host. Mol Microbiol *82*, 462-474, PMID: 21958024.

Tavares, J., Formaglio, P., Thiberge, S., Mordelet, E., Van Rooijen, N., Medvinsky, A., Menard, R., and Amino, R. (2013). Role of host cell traversal by the malaria sporozoite during liver infection. J Exp Med *210*, 905-915, PMID: 23610126.

Taylor, S.M., Cerami, C., and Fairhurst, R.M. (2013). Hemoglobinopathies: slicing the Gordian knot of Plasmodium falciparum malaria pathogenesis. PLoS Pathog *9*, e1003327, PMID: 23696730.

Taylor, S.M., Parobek, C.M., and Fairhurst, R.M. (2012). Haemoglobinopathies and the clinical epidemiology of malaria: a systematic review and meta-analysis. Lancet Infect Dis *12*, 457-468, PMID: 22445352.

Tembo, D., and Montgomery, J. (2010). Var gene expression and human Plasmodium pathogenesis. Future Microbiol *5*, 801-815, PMID: 20441551.

Theriot, J.A., and Mitchison, T.J. (1991). Actin microfilament dynamics in locomoting cells. Nature *352*, 126-131, PMID: 2067574.

Tilly, A.K., Thiede, J., Metwally, N., Lubiana, P., Bachmann, A., Roeder, T., Rockliffe, N., Lorenzen, S., Tannich, E., Gutsmann, T*., et al.* (2015). Type of in vitro cultivation influences cytoadhesion, knob structure, protein localization and transcriptome profile of Plasmodium falciparum. Sci Rep *5*, 16766, PMID: 26568166.

Tomley, F.M., and Soldati, D.S. (2001). Mix and match modules: structure and function of microneme proteins in apicomplexan parasites. Trends Parasitol *17*, 81-88, PMID: 11228014.

Tucker, R.P. (2004). The thrombospondin type 1 repeat superfamily. Int J Biochem Cell B *36*, 969-974, PMID: 15094110.

Turner, L., Lavstsen, T., Berger, S.S., Wang, C.W., Petersen, J.E., Avril, M., Brazier, A.J., Freeth, J., Jespersen, J.S., Nielsen, M.A*., et al.* (2013). Severe malaria is associated with parasite binding to endothelial protein C receptor. Nature *498*, 502-505, PMID: 23739325.

Tyska, M.J., Dupuis, D.E., Guilford, W.H., Patlak, J.B., Waller, G.S., Trybus, K.M., Warshaw, D.M., and Lowey, S. (1999). Two heads of myosin are better than one for generating force and motion. Proc Natl Acad Sci U S A *96*, 4402-4407, PMID: 10200274.

Uhrig, K., Kurre, R., Schmitz, C., Curtis, J.E., Haraszti, T., Clemen, A.E.M., and Spatz, J.P. (2009). Optical force sensor array in a microfluidic device based on holographic optical tweezers. Lab Chip *9*, 661-668, PMID: 19224015.

Vahokoski, J., Bhargav, S.P., Desfosses, A., Andreadaki, M., Kumpula, E.P., Martinez, S.M., Ignatev, A., Lepper, S., Frischknecht, F., Siden-Kiamos, I*., et al.* (2014). Structural differences explain diverse functions of Plasmodium actins. PLoS Pathog *10*, e1004091, PMID: 24743229.

van der Heyde, H.C., Nolan, J., Combes, V., Gramaglia, I., and Grau, G.E. (2006). A unified hypothesis for the genesis of cerebral malaria: sequestration, inflammation and hemostasis leading to microcirculatory dysfunction. Trends Parasitol *22*, 503-508, PMID: 16979941.

References

van Dijk, M.R., Douradinha, B., Franke-Fayard, B., Heussler, V., van Dooren, M.W., van Schaijk, B., van Gemert, G.J., Sauerwein, R.W., Mota, M.M., Waters, A.P.*, et al.* (2005). Genetically attenuated, P36p-deficient malarial sporozoites induce protective immunity and apoptosis of infected liver cells. Proc Natl Acad Sci U S A *102*, 12194-12199, PMID: 16103357.

Vanburen, P., Guilford, W.H., Kennedy, G., Wu, J.R., and Warshaw, D.M. (1995). Smooth-Muscle Myosin - a High Force-Generating Molecular Motor. Biophysical Journal *68*, S256-S259, PMID: 7787086.

Vanderberg, J.P. (1974). Studies on the motility of Plasmodium sporozoites. J Protozool *21*, 527-537, PMID: 4138523.

Vaughan, A.M., and Kappe, S.H.I. (2017). Malaria Parasite Liver Infection and Exoerythrocytic Biology. Cold Spring Harb Perspect Med *7*, PMID: 28242785.

Veigel, C., Bartoo, M.L., White, D.C., Sparrow, J.C., and Molloy, J.E. (1998). The stiffness of rabbit skeletal actomyosin cross-bridges determined with an optical tweezers transducer. Biophys J *75*, 1424-1438, PMID: 9726944.

Vincke, I.H., and Bafort, J. (1968). [Standardization of the inoculum of Plasmodium berghei sporozoites]. Ann Soc Belges Med Trop Parasitol Mycol *48*, 181-194, PMID: 5744433.

Vlachou, D., Schlegelmilch, T., Runn, E., Mendes, A., and Kafatos, F.C. (2006). The developmental migration of Plasmodium in mosquitoes. Curr Opin Genet Dev *16*, 384-391, PMID: 16793259.

Wang, M.D., Yin, H., Landick, R., Gelles, J., and Block, S.M. (1997). Stretching DNA with optical tweezers. Biophys J *72*, 1335-1346, PMID: 9138579.

Wang, Y.L. (1985). Exchange of actin subunits at the leading edge of living fibroblasts: possible role of treadmilling. J Cell Biol *101*, 597-602, PMID: 4040521.

Weng, H., Guo, X., Papoin, J., Wang, J., Coppel, R., Mohandas, N., and An, X. (2014). Interaction of Plasmodium falciparum knob-associated histidine-rich protein (KAHRP) with erythrocyte ankyrin R is required for its attachment to the erythrocyte membrane. Biochim Biophys Acta *1838*, 185-192, PMID: 24090929.

Wesseling, J.G., Smits, M.A., and Schoenmakers, J.G. (1988). Extremely diverged actin proteins in Plasmodium falciparum. Mol Biochem Parasitol *30*, 143-153, PMID: 2459617.

Wetzel, D.M., Hakansson, S., Hu, K., Roos, D., and Sibley, L.D. (2003). Actin filament polymerization regulates gliding motility by apicomplexan parasites. Mol Biol Cell *14*, 396-406, PMID: 12589042.

Wetzel, D.M., Schmidt, J., Kuhlenschmidt, M.S., Dubey, J.P., and Sibley, L.D. (2005). Gliding motility leads to active cellular invasion by Cryptosporidium parvum sporozoites. Infect Immun *73*, 5379-5387, PMID: 16113253.

Whitelaw, J.A., Latorre-Barragan, F., Gras, S., Pall, G.S., Leung, J.M., Heaslip, A., Egarter, S., Andenmatten, N., Nelson, S.R., Warshaw, D.M.*, et al.* (2017). Surface attachment, promoted by the actomyosin system of Toxoplasma gondii is important for efficient gliding motility and invasion. Bmc Biology *15*, PMID: 28100223.

References

Whittaker, C.A., and Hynes, R.O. (2002). Distribution and evolution of von Willebrand/integrin a domains: Widely dispersed adhesion and elsewhere. Molecular Biology of the Cell *13*, 3369-3387, PMID: 12388743.

WHO (2017). World Malaria Report 2017, pp. 196.

Yamauchi, L.M., Coppi, A., Snounou, G., and Sinnis, P. (2007). Plasmodium sporozoites trickle out of the injection site (vol 9, pg 1215, 2007). Cellular Microbiology *9*, 2093-2093, PMID: 17223931.

7 Appendix

7.1 Primer: Cloning TLP tail mutants

N°	Primer name	T °C	Sequence
P110	PbTLPfor_1 BamHI	47	CGggatccTAGGTGGTTCTACTAAGG
P111	PbTLPrev_1	41	ATTTTGATCTTTATAATTTTC
P112	PbTLPtestfor	55	TTTTGAGAAGGTATAACCCATATTCC
P113	PbTLPtestrev SacII	48	TCCccgcggAACATCCATATTAAATAACATCG
P159	TLPrepl_for SacII	54	TCCccgcggACAAATTAAAGAACAAATCGAGGG
P960	yFCU_seq_R	49	TAATTCAAAGGGACGAGG
P961	yFCU_seq_F	48	ATCCTCTGGTAATTTTTCG
P1129	TLPR1 fw SalI	52	ACGCgtcgacAAAAGAACCCGTAAATAGCG
P1130	TLPR1 rv EcoRV	53	ACACGCgatatcTGTTTTTTTTGATCATCCCCAT
P1192	fw TLP homology SalI	54	ACGCgtcgacGATAATATCGATACAGACCCTTATTGG
P1193	rv TLP homology EcoRV	55	gatatcATTATTATTATTATGATCTATATATGATTCAATACCTTTATTATTTC
P1194	fw 3'UTR TLP PstI	55	AActgcagAAATAAATTTAACGATATGGAAAGAAAAACAC
P1195	rv 3'UTR TLP HindIII	55	CCCaagcttCCTCCCAATAGACCCATTCC
P1234	1a rv tail deletion	61	CTTTCCATATCGTTAAATTTATTTTCATTTATAATTTTCAGTTTTTTGGG
P1235	1b fw tail deletion	61	CCCAAAAAACTGAAAATTATAAATGAAAATAAATTTAACGATATGGAAAG
P1236	1a rv W to A	58	CTTTCCATATCGTTAAATTTATTTTCATTTCGCTGGAGAATTGTC
P1237	1b fw W to A	61	GACAATTCTCCAGCGAAATGAAAATAAATTTAACGATATGGAAAG
P1238	GFP Fusion front rv 1a	62	GCCCTTGCTCACCATACCTCCACCTCCATTATTATTATTATGATCTATATATGATTCAATACC
P1239	GFP Fusion front fw 1b	62	GGTATTGAATCATATATAGATCATAATAATAATAATGGAGGTGGAGGTATGGTGAGCAAGGGC
P1240	GFP Fusion back rv 1b	65	TAATGTTTTTTTTGATCATCCCCACCTCCACCTCCCTTGTACAGCTCGTCCATG
P1241	GFP Fusion back fw 1c	65	CATGGACGAGCTGTACAAGGGAGGTGGAGGTGGGGATGATCAAAAAAAACATTA

Lowercase: restriction sites with overhangs to optimize enzyme activity

Uppercase: DNA-sequence; linker

Uppercase: bases flanking the recognition site to optimize cleavage